CHARLES UNIVERSITY IN PRAGUE

FACULTY OF MATHEMATICS AND PHYSICS

DEPARTMENT OF SURFACE AND PLASMA SCIENCE

DOCTORAL THESIS

DIAGNOSTICS OF LOW-TEMPERATURE PLASMA FOR TECHNOLOGICAL APPLICATIONS

BY

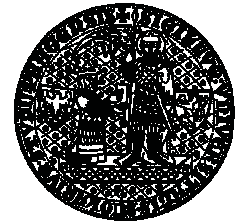VÍTĚZSLAV STRAŇÁK

SUPERVISOR
PROF. RNDR. MILAN TICHÝ, DRSC.

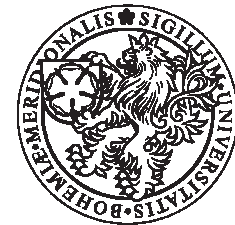STUDY BRANCH
PHYSICS OF PLASMAS AND IONIZED MEDIA

PRAGUE, JANUARY 2007

The work described in this thesis has been performed at:

Charles University in Prague
Faculty of Mathematics and Physiscs
V Holešovičkách 2
180 00, Praha 8
Czech Republic

University of South Bohemia
Department of Physics
Jeronýmova 10
371 15, Česke Budějovice
Czech Republic

E. M. A. University of Greifswald
Institute of Physics
Domstrasse 10a
174 89, Greifswald
Germany

Academy of Science of the Czech Republic
Institute of Physics
Na Slovance 2
180 00, Praha 8
Czech Republic

Dedicated to the memory of my grandparents,
Cecílie and Josef Bradáč († 2006).

Věnováno památce mých prarodičů,
Cecílii a Josefu Bradáčovým († 2006).

ACKNOWLEDGEMENTS

PREFACE

Recent developments of advanced technologies in bio-medicine, microelectronic, micro-mechanic and other branches have led to a renewed interest in plasma physics and plasma technology. Plasma produces energetic active species which initiate physical changes or chemical reactions, that can occur only with difficulty or not at all in ordinary chemical reactions.

Nowadays plasma is one of the essential tools in the large field of thin film deposition. Plasma deposition is one of the ways how to effectively replace ecologically unsuitable electrolytic coatings. Another advantage of plasma assisted deposition is possibility to create layers of unique properties. The surface treatment of different bio-materials and plasma-assisted layer coating on artificial implants are under high interest, too. These processes increase bio-compatibility, i.e. reduce the risk of implants not to be accepted by living tissue. Plasma sterilisation is another secondary effect of plasma technologies in biology and bio-medicine. Hence, the plasma sterilisation is investigated with the aim to replace sterilisation by toxic chemicals and agents.

Diagnostic of generated plasmas plays an important role in all laboratory experiments as well as in application research or industrial processes. The knowledge of elementary processes and major plasma parameters allows better control of processes and increases their reproducibility. So called *in situ* diagnostic, done under real application conditions, enables to find the optimum relation between input experimental quantities and output results.

The thesis topic is focused on diagnostic and partially on applications of two low-temperature plasma sources. The first one concerns diagnostic and applications of surfatron produced discharge. The surfatron plasma source working at 2.45 GHz was developed and built in the frame of the doctoral study.

The results of comprehensive diagnostic together with preliminary results of bio-medical and biology application (plasma sterilisation, seed treatment and surface treatment of plastic samples) are also included.

The second part is aimed at probe diagnostic of planar magnetron discharge, mainly used for deposition of thin TiO_x layers. This part of the work was done in tight cooperation with Institute of Physics, E.M.A. University in Greifswald (Germany), where the experimental device is situated.

The thesis consists of four main chapters. The chapter *Technological plasmas* summarises basic definitions about plasmas and their existing utilization in technological processes. This chapter gives raise to *Aims of the thesis*. The chapter *Sources of technological plasmas* introduces general features of devices which were employed in the experimental part of the thesis. The chapter *Diagnostic methods* theoretically describes the main way of data evaluation by means of probe techniques and optical emission spectroscopy. The fundamental chapters *Experimental results and discussion of surfatron plasma diagnostics* and *Experimental results and discussion of dc planar magnetron plasma diagnostics* include not only summary and discussion of the diagnostic and applications results but also description of particular experimental systems, which were used. **All data presented in graphs are interlaid by B-spline curves for greater clarity; the curves do not represent functional dependences.** Overview of the most important results is resumed in *Conclusion*.

LIST OF SYMBOLS

A_p	probe surface
c	velocity of light
$D_\lambda = r_\mathrm{p}/\lambda_\mathrm{D}$	Debye number
$e = 1.602{\cdot}10^{-19}\,\mathrm{C}$	elementary electron charge
E_m	mean electron energy
$\overline{E_\mathrm{m}}$	radially averaged mean electron energy
$h = 6.626{\cdot}10^{-34}\,\mathrm{J{\cdot}s}$	Planck constant
$i_\mathrm{e},\ i_\mathrm{i}$	electron and ion current
I_d	total probe current (double probe technique)
I_p	instant discharge current in active part of period
I_av	average discharge current over the period
$J_\mathrm{e0},\ J_\mathrm{i0}$	electron and ion thermal chaotic current
$k = 1.38{\cdot}10^{23}\,\mathrm{J \cdot K^{-1}}$	Boltzman constant
$K_\mathrm{i,e} = \lambda_\mathrm{i,e}/r_\mathrm{p}$	Knudsen number for ions and electrons
$m_\mathrm{e},\ m_\mathrm{i}\ (m_\mathrm{p}),\ m_\mathrm{n}$	masses of electron, positive ion and negative ion
$n_\mathrm{e},\ n_\mathrm{i}\ (n_\mathrm{p}),\ n_\mathrm{n}$	densities of electrons, positive ions and negative ions
$\overline{n_\mathrm{e}}$	radially averaged electron density
P	power
p	pressure
r_p	probe radius
r_s	space sheath thickness
$T_\mathrm{e},\ T_\mathrm{i}\ (T_\mathrm{p}),\ T_\mathrm{n}$	temperature of electrons, positive ions, negative ions
$\overline{T_\mathrm{e}}$	radially averaged electron temperature
$\langle T_\mathrm{e}\rangle$	*mean* value of electron temperature in plasma volume
T_eff	effective temperature
$T_\mathrm{r},\ T_\mathrm{v}$	rotational and vibrational temperature
U_d	voltage between probes (double probe technique)
$V_\mathrm{fl},V_\mathrm{p},\ V_\mathrm{pl}$	floating, probe and plasma potential
α	attenuation coefficient

$\eta = eV_{\mathrm{p}}/kT_{\mathrm{e}}$	normalized probe potential
λ_{e}, λ_{i}	electron and ion mean free path
ν_{e}, ν_{i}	electron and ion plasma frequency
ω	wave angular frequency

CONTENTS

1. TECHNOLOGICAL PLASMAS

1.1   Characterisation of plasma

First scientific studies of electrical discharges were done by H. Davy (arc discharge) and M. Faraday at the beginning of 19$^{\text{th}}$ century. However, the term *plasma* was introduced at first by *L. Tonks* and *I. Langmuir* in 1929 [1].

F. F. Chen defined plasma as quasi-neutral gas of charged and neutral particles which exhibits collective behaviour [2]. Plasma quasi-neutrality is sensed that one can assume for single charged particles $n_{\text{e}} \approx n_{\text{i}}$, where n_{e} and n_{i} denote electron and positive ions density, respectively. The particles can be in different quantum states - can be excited or de-excited to and from various energy levels. During these processes photons and subsequently light are produced. Collective behaviour means that not only local properties but also plasma conditions in remote regions influence plasma particles.

If there are only atoms as the heavy particles and only single charged positive ions in plasma, the degree of ionisation X in plasma is given by

$$X = \frac{n_{\text{e}}}{n_{\text{e}} + n_0}, \qquad (1.1)$$

where n_{e} is electron density and n_0 is density of neutral particles. There are plasmas with different degree of ionisation ($X \approx 10^{-8} - 1$) in the nature and in laboratory;

- $X \ll 1$ - plasma is weakly ionised;

- $X \lesssim 1$ – plasma is fully ionised;

Energy and temperature

Energy is the main factor which influences the plasma properties. In the state of **T**hermal **E**quilibrium (TE) the energetic proportion in plasma, i.e. the total content of energy and distribution function per degree of freedom (translation movement and excitation etc.) is characterised by thermodynamic state quantity – temperature T. Although this plasma state is realized only rarely, it represents important theoretical concept. Provided that the plasma is in this state the mutually inverse processes (for example ionisation-recombination, excitation-deexcitation) are in equilibrium (principle of detailed balance), i.e. they occur similarly often. The most significant properties of plasma in thermodynamic equilibrium are summarised in [3]:

- spectral distribution of radiation in plasma corresponds to radiation of the black body at temperature T, described by Planck law;

- all particles have Maxwell distribution of velocity (energy) with the same temperature T;

- occupation of excited states is in accord with Boltzmann distribution with temperature T;

- chemical equilibrium in plasma is given by Guldberg-Waag mass-action law with equilibrium constant corresponding to temperature T;

- for equilibrium of ionisation-recombination processes applies the Saha equation with ionisation temperature T.

Real plasma always shows deviations from full thermodynamic equilibrium because detailed balance of particular elementary processes with their inverse ones is disturbed. If these deviations are limited only to certain processes and stay small, we can describe the state of plasma as close to equilibrium. In this case some of mentioned thermodynamic equilibrium characteristics stay valid.

The most important model of plasma close to equilibrium is so-called **L**ocal **T**hermodynamic **E**quilibrium (LTE). In this state all properties except of

Planck radiation law stay valid. In particle balance, however, deviations from Planck law do not apply, provided that collision processes dominate over radiation processes (e.g. if the electron density is high or photoexcitation, optionally photoionisation is unimportant, i.e. system is optically thin).

At bigger deviations from equilibrium state the thermodynamic description of plasma fails and the detailed kinetic approach must be applied. The simplest among these cases of non-equilibrium conditions in plasma is when it is possible to describe every kind of particles in plasma (neutrals, electrons and ions) by their kinetic temperature (i.e. they have Maxwellian distribution function of velocity). The kinetic temperature can be derived from relation

$$kT_\mathrm{k} = \frac{1}{2}mv_\mathrm{p}^2, \tag{1.2}$$

where T_k is kinetic temperature, m and v_p denote mass and the most probable velocity of the particle, respectively. Taking the (1.2), one finds that 1 eV is equivalent to 11 604 K. The degree Kelvin (K) is inconveniently small unit with which to measure kinetic temperatures in plasmas, and so one usually expresses the kinetic temperature in electronvolt unit (eV).

division	*temperature*
non-isothermal LTP	$T_\mathrm{i} \approx T_0 \approx 300\,\mathrm{K}, \quad T_\mathrm{i} \ll T_\mathrm{e} \lesssim 10^5\,\mathrm{K}$
isothermal LTP	$T_\mathrm{e} \approx T_\mathrm{i} \approx T_0 \approx 2.10^4\,\mathrm{K}$
HTP	$T_\mathrm{i} \approx T_\mathrm{e} \gtrsim 10^7\,\mathrm{K}$

Tab. 1.1: Subdivision of plasmas.

If kinetic temperatures of electrons and ions (neutrals) are different $T_\mathrm{e} \neq T_\mathrm{i}$, it is so-called **non-isothermal** plasma, which is described by degree of anisothermicity τ,

$$\tau = \frac{T_\mathrm{e}}{T_\mathrm{i}}. \tag{1.3}$$

Depending on particle temperature, plasmas are frequently subdivided into **L**ow-**T**emperature (LTP) and **H**igh-**T**emperature (HTP) plasma. The ex-

planation is given in Tab. 1.1. The symbols T_{i}, T_{e}, T_0 denote temperatures of ions, electrons and neutral particles, respectively [4].

Debye screening length

The electrical potential distribution of a charge carrier inside a plasma is different from the corresponding distribution in a vacuum. In a plasma each charge carrier polarizes its surrounding and thereby reduces the interaction length of Coulomb potential. Ability to screen electric potentials, which are put in plasma, is one of the most important fundamental property of plasma behaviour. The characteristic scale of screening or the width of the space charge sheath is determined by so-called Debye length λ_{D} [4]

$$\lambda_{\mathrm{D}} \equiv \left(\frac{\varepsilon_0 k T_{\mathrm{e}}}{n e^2} \right)^{1/2}, \tag{1.4}$$

where ε_0 is dielectric permittivity in vacuum, e is the electron charge.

Outside the Debye length λ_{D} the potential may be neglected. Equation (1.4) is valid only if there is enough particles in the space charge sheath: $N_{\mathrm{D}} \gg 1$, where $N_{\mathrm{D}} = 4/3\,\pi\,n_{\mathrm{e}}\lambda_{\mathrm{D}}^3$ is the number of particles in the so-called Debye sphere. Hence, the collective behaviour requires two valid conditions: **(i)** charge density must be high enough to fulfil criterion $\lambda_{\mathrm{D}} \ll L$ (L is plasma size) and **(ii)** Debye screening must be valid, i.e $N_{\mathrm{D}} \gg 1$.

1.2 Plasma for technological applications

The non-thermal low temperature plasma is mostly used for technological surface applications. Low (often room) temperature of neutral species protects material against thermal degradation while plasma characteristics are preserved. The most common way of plasma generation in laboratory or industry is by external electric field.

The electric discharges can be classified by the nature of applied electric field to dc (direct current) and ac (alternating current) discharges. The ac discharges are further divided according the frequency of applied power into

three groups:

- low frequency discharges, range of kHz, $\nu_{\mathrm{disch}} \ll \nu_{\mathrm{e}}, \nu_{\mathrm{i}}$,

- radio-frequency discharges (RF), range of MHz, $\nu_{\mathrm{i}} < \nu_{\mathrm{disch}} < \nu_{\mathrm{e}}$,

- microwave discharges (MW), range of GHz, $\nu_{\mathrm{disch}} \gg \nu_{\mathrm{e}}, \nu_{\mathrm{i}}$,

where ν_{i} and ν_{e} denote ion and electron plasma frequency respectively, as they are defined in detail e.g in [5].

Plasma offers several points of industrial interest. The energy contained in a plasma, which is higher compared with energy in ideal gas at the same conditions, is one of the most important factor for technological applications. Beside the energy in plasma is distributed into several components which mutually interact together during series of processes. These energy components and their interactions determine dynamic plasma properties. The main plasma energy components are [3]:

- energy of electric field,

- energy of magnetic field,

- ionisation energy,

- translation energy of particles (neutral as well as charged particles),

- excitation energy (electron, vibrational and rotational excitation),

- radiation energy,

- energy of collective phenomena (oscillation etc.).

Active species in reactive discharges include not only free electrons and ions but also radicals, highly reactive neutral particles and results of primary chemical reactions as clusters, monomers and reactive molecular fragments. Compared with classical ways the plasma-assisted technologies do not create by-products or waste.

1.3 Selected plasma assisted technological processes

1.3.1 Low-temperature plasma sterilisation

Low temperature plasma is able to produce energetic active species and UV radiation which can initiate specific physical and chemical reactions with sterilisation effects. Plasma-based sterilisation is a promising alternative method for standard surgical instruments as well as for biomedical devices based on heat sensitive materials. Gas plasma was reported to be suitable for sterilisation of metals, natural rubber, silicone and various polymers as polyvinyl chloride, polyethylene, polyuretane etc. [6].

Sterilisation of such materials can not be realized by conventional way in hot water vapour (so called steam sterilisation) in autoclaves, with $t \approx 121\,°\text{C}$, $p \approx 121\,\text{kPa}$. Hence ethylene oxide (EtO) sterilisation is routinely used to sterilise materials that can not withstand the high temperature of autoclaving. This sterilisation technique requires long time (up to 24 hours) aeration process for treated articles and, above all essentially, makes a serious danger for both service persons and environment. Another way of cold sterilisation technique is radiation. Gamma rays from a cobalt-60 isotope source or machine-generated accelerated electrons are usually used.

Sterilization means total destruction of microorganisms and their spores. In spite of the fact that several plasma-based sterilisation technologies have been developed, their mechanism is not clearly and completely understood yet. *Moisan et al.* assumed three following elementary processes of sterilisation [7, 8]:

- Destruction of the generic material of the organism by UV irradiation.

- Erosion of the micro-organism, atom by atom, through intrinsic photodesorption. Photon-induced desorption results from UV photons breaking chemical bonds in the micro-organism material and leading to the formation of volatile compounds from atoms intrinsic to the micro-organism.

- Erosion of the micro-organism, atom by atom, through etching. Etching results from the adsorption of reactive species from the plasma (active glow or afterglow) on the micro-organism with which they subsequently undergo chemical reactions to form volatile compounds (spontaneous etching). The reactive species can be atomic and molecular radicals, e.g. O and OH, respectively, and excited molecules, e.g. the $^1O_2$. This chemistry, under thermodynamic equilibrium conditions, yields small molecules (e.g. CO_2, H_2O) which are the final products of the oxidation process [9].

Plasma sterilisation efficiency is strongly influenced by numerous experimental parameters as described by *Lerouge et al.* [10]. The gas composition is a determining factor in the effectiveness of sterilisation. It dictates the types of active species (radicals, excited molecules) and, at the same time, the intensity and wavelengths of emitted UV and VUV radiation. Former experiments demonstrated that oxygen-based plasmas are more efficient in sterilisation than pure Ar (or other pure rare gas) plasmas. The most important oxygen-based plasmas as pure O_2, CO_2 or mixtures O_2/H_2, Ar/O_2, CF_4/O_2 have been studied [11]. The theoretical aspects of plasma sterilisation with oxygen, including fundamental mechanisms and kinetics, have been previously presented and discussed [9]. Without going to microbiological details *Moreau et al.* [12] said that the genetic material carried by DNA helices is in the case of bacterial spores protected by a series of "defence walls" and coats. Total inactivation of the spores is obtained when the DNA material is so heavily damaged that it can not repair itself.

The efficiency of the sterilisation processes is usually displayed by so-called survival curve: a logarithm plot of the number of surviving micro-organisms as a function of exposure time. The survival curve usually consists of several phases; the most often bi-phasic or three-phase inactivation mechanism was observed [13]. To characterize the slope of each phase segment, called inactivation phase, the time D required to decrease a given population of spores by a factor 10 is used. In the same work *Moisan et al.* suggest explanation of three-phase sterilisation mechanism. As a rule, first and third phase

have approximately the same D value which is much shorter than D time of second phase. Destruction by UV photons of isolated spores dominates during phase 1. Phase 2 would be partly dependent on the erosion rate of the various materials (coatings, debris, dead spores) covering still living spores. Phase 3 starts when the spores that were not inactivated during phases 1 and 2 have been sufficiently eroded or cleared from debris for UV photons to finally kill them. This explain why D_1 and D_3 are close and why the third phase is observed immediately before sterilisation is achieved.

Plasma sterilisation efficiency has been investigated for several sorts of spores. First, plasma sterilisation was tested on *Bacillus subtilis. Nelson et al.* [14] showed on *B. subtilis* that O_2 is very efficient agent for sterilisation in high frequency (RF 13.56 MHz) discharge. *Kelly-Wintenberg et al.* [15] used an atmospheric uniform glow discharge (OAUGDP) to inactivate various micro-organisms, including bacterias and endospores, applied on different porous and non-porous surfaces (glass, agar, polypropylen, paper). *Hury et al.* [16] reported the inactivation of spores exposed in Ar/O_2, (CO_2, H_2O_2) based microwave sustained plasmas at low pressures. They used *B. cecerus, B. subtilis, B. pumilis, B. stearothermophilus* as test spores. It was found that survival-curves are rather similar but *B. subtilis* was a bit more resistant than *B. stearothermophilus.* This is in contrary with results of *Kelly-Wintenberg et al.* [17] using OAUGDP system. Microwave flowing post-discharge was also used by *Ricard et al.* [18] with the aim of *E. coli* inactivation. They studied sterilisation mechanism of Ar/O_2 by means of optical emission spectroscopy. Later the discharge N_2/O_2 under similar condition was also studied [19].

New bio-compatible plasma source, so called plasma needle, originally developed for high precision tissue treatment, was introduced by *Stoffels et al.* [20]. The source generates RF (13.56 MHz) plasma of small size (in order of milimeters) at low power (from 10 mW up to 5 W). Excitation and vibrational temperatures are close to each other, in the range 0.2 - 0.3 eV, rotational gas temperature is at most of few hundred Kelvins. The generated plasma is of non-aggressive nature i.e. it can be applied on organic materials without causing electric or thermal damage of the surface. The plasma needle was used also for deactivation of *E. coli* bacteria under atmospheric pressure [21].

1.3.2 Plasma treatment of seed

In recent years the plant stimulation using physical factors like ionizing radiation, laser, high-power light radiation, high electro-magnetic field etc. has been examined. The main aim of these investigations is to search for methods to improve the sowing quality of seed. One of the most important criteria of the sowing material quality is germination. Experiments have to distinguish laboratory germination (ability to germinate in laboratory conditions) from field germination (ability to germinate in agricultural conditions). Seed germination is unsatisfactory, in agriculture branch, if is less than 95 %. *Dubinov at al.* [22] treated oat (*Avena Savita*) and barley (*Hordeum Rulgare*) seeds by air glow discharge with the view to increase their germination under laboratory conditions. The seeds were treated in continuous as well as in pulsed discharge regime for several minutes (up to 4 min). The seed was successfully stimulated and germination increased.

Zivkovic et al. [23] used for *Paulownia tomentosa* seed stimulation air and argon RF (13.56 MHz) discharge with incoming power of about 100 W. The experiments were done under reduced pressure about 10 Pa. Simple tests proved unaffection of germination by vacuum. Plasma exposure on the seed caused increasing of their germination almost three times - from 25 % up to 75 %. The maximum germination was achieved after 10 minutes of treatment. The authors considered that the stimulation effect of air-derived cold plasma pre-treatment could be explained on the basis of three different mechanisms: etching, surface functionalism and deposition of bio-active small molecules.

The last mentioned mechanism, deposition of bio-active molecules, was investigated by *Volin et al.* [24]. They carried experiments with CF_4 and ODFD (octadecafluorodecalin) plasmas generated by RF driven (13.56 MHz) electrodes in vacuum chamber. Pre-treatment by these plasmas of peas (*Pisum sativum*), radish (*Raphanus sativum*), bean (*Phaseolus vulgaris*), corn (*Zea mays*) and soybean (*Glycine max*) caused delay of germination. Pre-treatment process may result in the covalent or non-covalent attachment of plasma-produced molecular fragments on the seed envelope. In a context this process can be considered as some kind of seed coating. It has been

demonstrated that fluorine-carbon (F-C) ratio controls forming of macro-molecular-structure: high values of the ratio shift the mechanism towards etching process, low values lead to fluorocarbon layer deposition [25]. On the other hand, nitrogen-based plasmas (aniline, hydrazine) caused small acceleration of seed germination of soybean (*Glycine max*) and corn (*Zea mays*).

1.3.3 Surface treatment and activation of plastic materials

Plasma surface treatment uses active species, produced by plasma, to modify surface characteristics of solid materials. It may involve chemical reactions with surface, add or remove surface charge, remove adsorbed monolayers or change physical or chemical state of the superficial monolayer of a material [26]. Plasma surface treatment can be used for a wide spectra of applications - changes of surface energy, surface cleaning, improving cohesive and adhesive properties etc. - because of its technical and economical advantages [27].

Plasma surface treatment is very often intended to change, increase or decrease, surface energy. The surface free energy is the work done against surface tension forces in creating a unit area of liquid on the surface. It is associated with the ability of water to wet surfaces. The free surface energy unit is $J.m^{-2}$. Probably the most important surface energy-related characteristic is wettability. Wettability is the ability to absorb a liquid on a solid surface, or to adsorb a liquid in the bulk of fibrous materials. When the free surface energy of the material is lower, it is relatively unwettable and water will bead up on its surface and vice versa.

Many industrial plastics such as polyethylen (PE), polypropylen (PP), poly-tetrafluorethylen (PTFE) have low surface energy and lacquers, inks and adhesives do not sufficiently wet them. With the view to increase wettability *Ooji et al.* [28] modified PE and PP surfaces by plasma polymerisation. In another work by *Barni et al.* the wettability and dyeability of polyethylen terephthalate (PET) was modified using radio-frequency SF_6 plasma at reduced pressure [29]. Recently there were found several methods of surface activation under atmospheric pressure. *Choi et al.* [30] used atmospheric pressure dielectric barrier discharge (He, CF_4 in air) for treatment of PP.

Janca et al. [31] used the dielectric barrier discharge (DBD) for the activation of oiled polyester (PES) multicord sewing threads for tires. Namely the barrier discharge created at higher frequencies in nitrogen remarkably improves the adhesion of the cord to rubber. Another type of discharges used for plasma activation are so-called surface discharges. Such a type of discharge, surface discharge induced plasma chemical processing (SPCP), was at first introduced by *Masuda et al.* [32] in 1988. In the original configuration the discharge was not suitable for industrial applications because of limited life-time of electrodes. To reduce this limitation a novel surface discharge type, coplanar diffuse surface discharge (CDSD), was developed by *Cernak et al.* [33]. This surface discharge was used for several applications, e.g. for increasing of wettability the non-woven polypropylen [34].

1.3.4 Plasma sputtering deposition of thin films

Deposition technologies are often used to deposit electrically conducting or insulating layers for microelectronic circuits, optical coatings, protective coatings, recording media and other. The thickness of deposited layers is in the range from approximately tens of nanometers to several tens of microns.

Devices called magnetrons are primarily used for physical vapour deposition (PVD) processes. Magnetron principles are known for a long time since 1978 from works by *Waits* [35] and *Thornton* [36] in planar or cylindrical configuration, respectively. Magnetron sputtering deposition sources are now widely used in industry because of their simple technology, economic acceptability and easy alterable physical conditions. Magnetron technology as well as magnetron plasma diagnostic is, however, continuously developing because new advanced films with prescribed physical and functional properties are needed. Perspectives of magnetron sputtering in surface engineering were described by *Musil* and *Vlcek* [37].

The ions generated by electron impact ionisation are accelerated due to strong electric field towards the target which is made from the material to be deposited. If the background pressure is sufficiently low then the mean free paths of the sputtered atoms, after ion target bombarding, are comparable or greater than the distance between target and substrate and sputtered atoms coat the substrate. The process of substrate coating is characterized by deposition rate (thickness per time unit). If a substrate sample does not move with respect to the plasma source the deposition rate is easily determined by dividing thickness of deposited layer by deposition time. For such static deposition by means of planar magnetrons the thickness of layer is usually non-uniform. Substrate motion raises the layer quality but enumeration of deposition rate is more complicated.

Plasma density is the most important factor directly connected with deposition rate and deposition efficiency. For technological applications it would be advantageous to achieve high deposition rate. The major factor limiting deposition rate is the maximum power flux which can be applied to the cathode without causing its cracking, sublimation or melting. The deposition rate can influence properties of deposited films; in detail studied, e.g., by *Musil et al.* [38].

With the view to increase deposition efficiency magnetrons are often modified, e.g. by additional RF and MW (microwave) component [39], by plasma confinement [40, 41] or simply by using two magnetrons working in dual sputtering system [42]. Other way how to deliver higher power density into discharge is operating of magnetrons in pulsed regime.

2. THE AIMS OF THE THESIS

The thesis was focused on development of new plasma sources and subsequent diagnostics of generated plasmas. The plasma sources were envisaged for technological applications. Hence, preliminary tests and experiments of the plasma-assisted technological applications were also included. The main aims of the thesis were as follows:

1) Plasma source working at 2.45 GHz frequency for technological applications

a) First aim of the thesis was the development and construction of a new plasma source working at microwave range of frequencies that could be used for technological applications. The plasma generation was based on surfatron principle (2.45 GHz) of jet type. The plasma source was operated at wide range of pressures, up to atmospheric, with different working gas mixtures. The source was being developed with the view of future application on heat sensitive materials. Thermal sensitive samples had to be protected from overheating. Homogeneous treatments of samples during application experiments should have been achieved.

b) Second task was to carry out a comprehensive diagnostics of the above described plasma source, i.e. determination of basic plasma parameters using probe technique and optical emission spectroscopy. Plasma potential, electron energy and electron density were determined from single probe measurement at low pressures. In wide range of pressures double probe technique was used for determination of electron temperature. Results of probe measurements were evaluated under different experimental conditions in continuous as well as in pulsed regime. Vibrational and rotational temperatures of molecular species were estimated from optical emission spectroscopy.

c) Surfatron plasma was applied in preliminary tests for sterilisation, seed treatment and surface modification of plastic samples. Sterilisation efficiency was assessed from the rate of deactivation of test micro-organisms. Seed was treated by surfatron plasma with the intention of increase germination. Surface of plastic samples (PE) was modified in order to change the free surface energy.

2) Planar magnetron plasma source for deposition of thin films

a) Planar magnetron system, used for deposition of thin oxide and nitride films, was studied in detail by means of Langmuir probe measurements in continuous regime. At the beginning the probe measuring system was developed and commissioned the probe was implemented into the vacuum chamber. Plasma potential, electron density and electron temperature were determined as dependences of radial and axial probe position.

b) Growth rate of deposited layer can be significantly increased using pulsed regime. Hence, conventional planar magnetron system was modified for operation in pulsed regime. For determination of plasma parameters in dependence on time the method of time-resolved probe measurement was suggested and developed.

c) Comprehensive time- and spatial-resolved measurements by Langmuir probe in pulsed regime were carried out. The basic plasma parameters were determined from probe data and compared with parameters reached in continuous regime.

3. SOURCES OF TECHNOLOGICAL PLASMAS

The various types of plasma are produced in principle by: **(i)** dc glow discharges, either operated continuous in pulse regime, **(ii)** capacitively and inductively coupled rf discharges, **(iii)** microwave discharges etc. As quoted above this thesis is aimed at description, development, commissioning, testing, diagnosing and application of microwave surfatron plasma source and dc planar magnetron; both of them were used for experiments done in the frame of doctoral study. Their basic physical principles are introduced below; more detail information can be found in quoted references.

3.1 *Surface-wave discharges*

Surface-wave discharges (SWD), also called "long microwave discharges" are known since 1970s as a part of larger class of high frequency (HF) discharges [43]. The characteristic feature of SWD is that the energy delivered to the active plasma zone comes from the power flux carried by an electromagnetic wave propagating along the plasma column. This is an essential difference between the situation where the surface wave propagates along plasma column created by some other means, e.g. along a positive column of a dc discharge. In SWD case the discharge and the wave field interact self-consistently and can not be controlled independently.

When considering SWD discharges the attenuation characteristic $\alpha(\overline{n_e})$ is the main interest; $\overline{n_e}$ is the cross-section averaged electron density and α is the attenuation coefficient. Analytical approximation of $\alpha(\overline{n_e})$, at low gas

pressure is expressed as [44]

$$\alpha\left(\overline{n}_{\mathrm{e}}\right) = \frac{B\left(\omega, a\right) \nu_{\mathrm{ef}}}{\overline{n}_{\mathrm{e}} - n_{\mathrm{D}}}, \tag{3.1}$$

where n_{D} is the electron density corresponding to the wave resonance, $B\left(\omega, a\right)$ has to be determined by fitting equation (3.1) to the attenuation characteristic computed for ω (wave angular frequency) and a (plasma radius). The effective electron collision frequency ν_{ef} depends on the nature of the gas and, to some extent, is proportional to its pressure. The equation (3.1) implies that $\overline{n}_{\mathrm{e}} > n_{\mathrm{D}}$ and so n_{D} defines the end of the plasma column. It shows that $\alpha(\overline{n}_{\mathrm{e}})$ increases with decreasing electron density $\overline{n}_{\mathrm{e}}$. The attenuation characteristic was studied theoretically [45, 46] as well as experimentally [47].

The condition for a stable power balance in SWD, where the length of the active zone is large compared with its diameter, was at first formulated by *Zakrzewski* [48]

$$\frac{\mathrm{d}\,\alpha(\overline{n}_{\mathrm{e}})}{\alpha(\overline{n}_{\mathrm{e}})} < \frac{\mathrm{d}\overline{n}_{\mathrm{e}}}{\overline{n}_{\mathrm{e}}}. \tag{3.2}$$

The initial stage of SWD was described by *Shivarova* [49]. The initial breakdown takes place in the discharge tube close to a launcher gap. It occurs spontaneously, when the intensity of the electric field extending from the launcher is large enough. Due to the field gradients within the gap region of the exciter, the electrons are driven along the tube axis by the ponderomotive force. Once the electron density $\overline{n}_{\mathrm{e}}$ in the launching area exceeds n_{D}, the surface wave propagates until it is reflected back at the axial position where $\overline{n}_{\mathrm{e}} \approx n_{\mathrm{D}}$. Nevertheless, at that point the electrons are ejected forward because of the large electric field gradient there, which enhances the plasma. This process allows the electromagnetic field to gradually extend away from the launcher, the ionisation front moving along with the wave field.

3.1.1   Surface-wave launcher - Surfatron

The wave launcher consists of an impedance matching network and field applicator. The impedance matching network optimises the power transfer

to the plasma. The overall efficiency of the surface-wave plasma source can be quantitatively expressed as $\eta = P_A/P_I$, where P_A and P_I are power absorbed in the plasma and incident power flux in the feed line, respectively.

The aperture, the most commonly used for sustaining a plasma column with an azimuthally symmetric ($m = 0$ mode) surface wave, consists of a cylindrical metallic tube and a thin metallic plate. The metallic tube generally surrounding the discharge tube and the thin plate is located perpendicularly to the tube axis and positioned at a few milimeters from it. The high-frequency power is supplied to the launcher such that, in the gap region, a strong electric field excites the wave. When the launcher is properly designed, most of the power leaving the gap is carried away by two oppositely directed surface waves, and this power is gradually used to sustain the discharge [50]. This coaxial device, called surfatron, was introduced by *Moisan et al.* [51] at first.
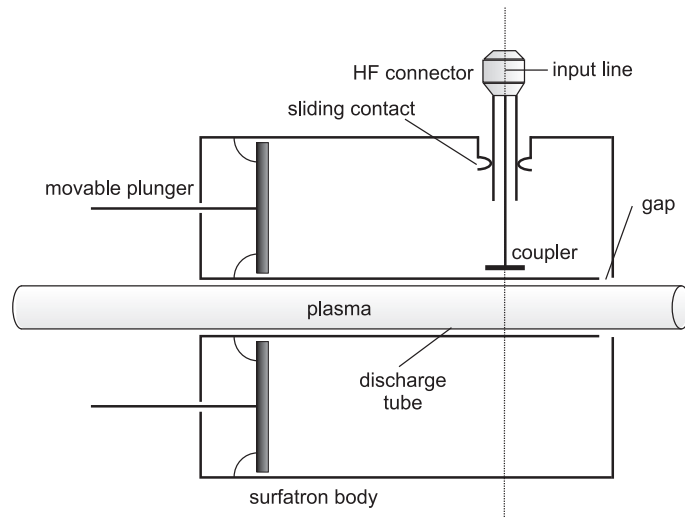
Fig. 3.1: Axial cross-section of a surfatron body showing the field shaping structure (gap) and the tunable means (movable plunger and coupler) [50].

The surfatron cross-section is shown in Fig. 3.1. The surfatron structure consists of two metal cylinders forming a section of coaxial line terminated by a short circuit at one end and by a circuit gap at the other. This structure has a required shape and symmetry, so the electric field extending through the gap can excite the azimuthal surface wave sustaining plasma column in the axially placed dielectric tube. Quartz is the best material for the tube be-

cause of its low tangent loss. The coupler, constructed from semi-rigid coaxial cable, is placed radially in the structure and extending outside where it is connected to the input transmission line. The coupler, electrically connected to the surfatron body, is movable in radial direction. Depth of coupler insertion affects the input impedance, its imaginary part, of the surfatron and thus power coupling. The real part of the input impedance is affected by changing the structure length l_1 (see Fig. 3.2) through movable plunger. It is possible to tune the surfatron so that the input power is totally absorbed by the plasma.
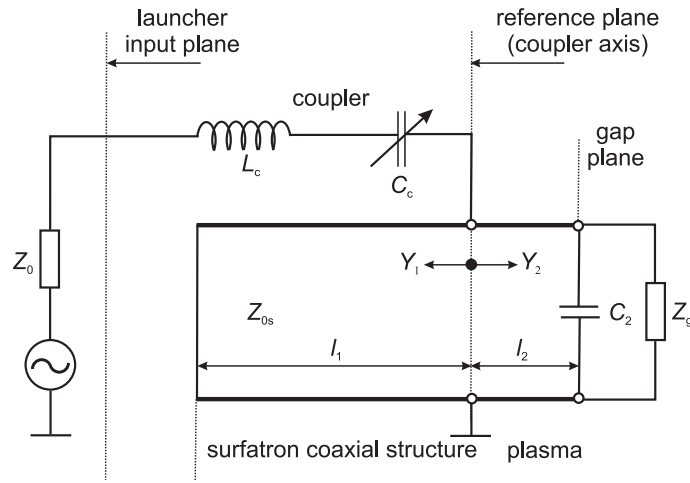
Fig. 3.2: The equivalent circuit of surfatron plasma source. The two heavy lines figure an equivalent transmission line of characteristic impedance Z_{os}, of lengths l_1 and l_2 with respect to the refence plane [52].

The theory and characteristics of surfatron producing long plasma columns was brought by *Moisan et al.* [52]. The HF power is supplied to the surfatron via the coaxial line (characteristic impedance Z_0) that feeds the coupler. In the equivalent principal circuit the coupler is represented by the capacitance C_{c} connected in series with the inductance L_{c}, see Fig. 3.2. The characteristic impedance of the coaxial structure of the surfatron main body is denoted $Z_{0\mathrm{s}}$. Then the admittance from side 1, left part with respect to the reference plane in Fig. 3.2, is that of a line of length l_1 and characteristic impedance $Z_{0\mathrm{s}}$, terminated by short circuit:

$$Y_1 = (\mathrm{j}Z_{0\mathrm{s}} \tan 2\pi l_1/\lambda)^{-1}\,, \qquad (3.3)$$

where λ is the free-space wavelength. The admittance Y_2, from side 2 (right part with respect to the reference plane in Fig. 3.2), is the input admittance of length l'_2 and characteristic impedance terminated by a capacitance C_2 in parallel with Z_g - the equivalent impedance of the plasma seen from the gap. The length l'_2 is possibly shorter than the actual distance l_2 in the Fig. 3.2, between coupler and the front plate, because of existence of capacitance C_2. Then the Y_2 is described by the formula

$$Y_2 = \frac{1}{R_g} \cdot \frac{(\omega R_g C_g)^2}{1 + (\omega R_g C_g)^2} + \mathrm{j}\omega C_2 \left(1 + \frac{C_g}{C_2} \cdot \frac{1}{1 + (\omega R_g C_g)^2}\right). \tag{3.4}$$

The R_g and C_g are used for description of total impedance seen from gap; their exact meaning and definition can be found in [52]. There can be also found the input impedance Z_{in} of a surfatron normalized with respect to the feed-line characteristic impedance Z_0. Thus

$$\frac{Z_{in}}{Z_0} = \frac{R_{in}}{Z_0} + \mathrm{j}\frac{X_{in}}{Z_0} = \frac{g_2}{g_2^2 + (b_2 - z/t_1)^2} + \mathrm{j}\left(\frac{\omega L_c}{Z_0} - \frac{1}{\omega C_c Z_0} - \frac{b_2 - z/t_1}{g_2^2 + (b_2 - z/t_1)^2}\right), \tag{3.5}$$

where

$$g_2 = Z_0 G_g, \quad b_2 = Z_0 \left(\omega C_2 + B_g\right), \quad z = Z_0/Z_{0s}, \quad t_1 = \tan 2\pi l_1/\lambda. \tag{3.6}$$

Here G_g and B_g denote the gap conductance and susceptance, respectively. Hence, the gap admittance can be expressed by formula $G_g + \mathrm{j}B_g \equiv Z_g^{-1}$ [50]. $Y_1 Z_0 = -\mathrm{j}(z/t_1)$ and $Y_2 Z_0 = g_2 + \mathrm{j}b_2$ are normalized admittances seen in each direction from the reference plane, which coincides with the coupler axis, as shown in Fig. 3.2. The admittance Y_1 is imaginary for a lossless structure. The plasma impedance Z_g depends on two effects. The first is capacitive effect caused by the presence of a plasma-filled tube in the electric field extending from the gap. The other is the launching of surface wave in both directions along the plasma column. Plasma impedance as a function of the gas, flow rate, microwave power and other parameters was experimentally determined [53].

The ratio of the reflected P_r and the incident power P_{in} at the input of a surfatron is described by formula

$$\frac{P_r}{P_{in}} = \left| \frac{Z_{in} - Z_0}{Z_{in} + Z_0} \right|^2 .\tag{3.7}$$

For a given R_{in}/Z_0, the reflected power is minimum when imaginary part $X_{in} = 0$. This condition can always be met by adjusting the coupler insertion length, and thus C_c, providing L_c is large enough. Only one setting of the capacitive coupler yields $X_{in} = 0$ for given conditions; so-called tuning characteristics were studied and published in [50, 52]. Generally, the frequency upper limit of operation depends on the design of gap-coupler part of the surfatron and decreases with increasing plasma tube radius. Above the frequency limit the reflected power rises with frequency. The maximum input power is determined mainly by the quality of the cable and connector. Through experiments the upper power limit for surfatron working with frequency 2.45 GHz has been found to be around 500 W in cw regime [54].

3.1.2 Main features of surface-wave discharges

In the last years the SWDs have been subjected to thorough theoretical and experimental studies. A self-consistent theory was applied by *Ferreira* [55] on the first experimentally investigated results [52]. The self-consistent theory predicts absolute values and radial profiles of electron density $n_e(r)$, electron temperature $T_e(r)$, electric field intensity E_r and other parameters. These values are in qualitative agreement with later theoretical work by *Nowakowska et al.* [56]. The parameters are dependent on the power delivered to the discharge and pressure. The absolute values of electron density and collision frequency as a function of delivered power were determined on base of the reflection coefficient measurements by *Musil* and *Vyskocil* [57, 58]. The axial electron density gradient dn_e/dz and axial distribution of electron density $n_e(z)$ along the column length decrease almost linearly towards the column end [59, 60]. The behaviour of $n_e(z)$ was described by *Ferreira* [61].

The electron energy distribution function (EEDF) in Ar discharge at low pressure was investigated using Langmuir probe measurements by *Kortshagen et al.* [62, 63] and *Grosse et al.* [64]. The body of EEDF was less populated compared with Maxwellian distribution that was obtained theoretically as well as experimentally. It should be taken into account that at higher degree of ionization, the influence of electron-electron collisions increases and deviation from the Maxwellian distribution decreases. The self-consistent kinetic model for nitrogen discharge was developed and used for determination of EEDF in [65].

Surface wave produced plasmas have low density of fluctuations and they are perfectly reproducible. Because of this reason they are a promising tool for technological applications. Mainly Ar discharge was subjected to basic investigations. For technological application the mixtures of gases with a reactive components are often used. The He [66, 67, 68], O_2/N_2 [69], N_2/H_2 [70], N_2 [71, 72] and other discharges were studied theoretically as well as experimentally. A review of surface-wave sustained discharges for technological applications was made by *Moisan et al.* [73]. In works by *Musil* microwave plasmas were subjected to investigation with the view of thin film deposition [74, 75].

3.2 Principle of dc-planar magnetron discharge

A typical planar magnetron sputtering system consists of a planar cathode (sputtering source or target) parallel to an anode surface (usually grounded), which serves as a substrate holder. The cathode assembly consists of the source material, dependent on the deposited layer, directly connected with the backing power electrode. Magnets are placed below backing electrode. The structure of the magnetron is shown in Fig. 3.3; the important parts of magnetron are numbered as 1 magnets, 2 magnetic circuit and target clamp (iron), 3 coolant chamber, 4 shielding (ground), 5 insulator, 6 target (Ti), 7 cooper meant, 8 water tube cooling, 9 substrate [76].

If the negative voltage is applied on the cathode and the pressure is low
enough, a glow discharge is formed. Negative particles (mainly electrons) of
a dc glow discharge are trapped by external magnetic field, which in a certain
region above the cathode runs parallel to the cathode surface. Such configu-
ration increases electron density in a localized zone. The increased electron
concentration leads to higher ion production through ionisation collisions.
Radial current distribution is peaked at the radius at which the magnetic
field is tangent to the cathode plate [77]. Relatively strong electric field
between the positive glow plasma and the cathode accelerates ions towards
the cathode, where they sputter the cathode material. The most intensive
sputtering of the target is visible as an erosion rill called race-track [78]; see
Fig. 3.4.
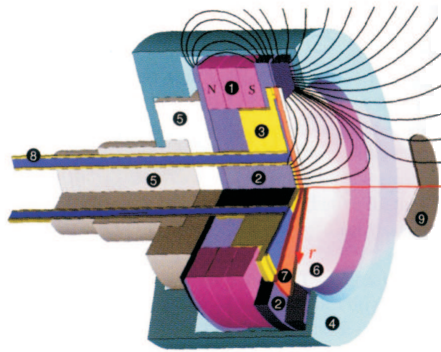
Fig. 3.3: The cross-section of mag-
netron [76].
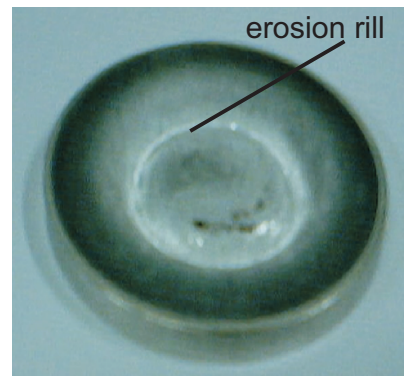
Fig. 3.4: Erosion rill on the Ti tar-
get, ϕ 77 mm.

The external magnetic field is essential feature of magnetrons. Planar mag-
netrons can be operated with two types of magnetic fields corresponding to
balanced (BLM) [77] and unbalanced (UNB) mode [79], see Fig. 3.5. Gener-
ally, it is difficult to precisely distinguish between modes. The characteristic
feature of balanced mode are magnetic field lines well confined around the
cathode. The electron loss is reduced to minimum. The basic principle of
the unbalanced magnetron is to allow release of electrons from the magnetic
trap in order to create ionization away from the magnetron cathode near by
substrate. *Sheridan et al.* showed that electrons escape from plasma up the
"chimney" along the axis of cathode in UNB magnetron [80, 81]. On the con-
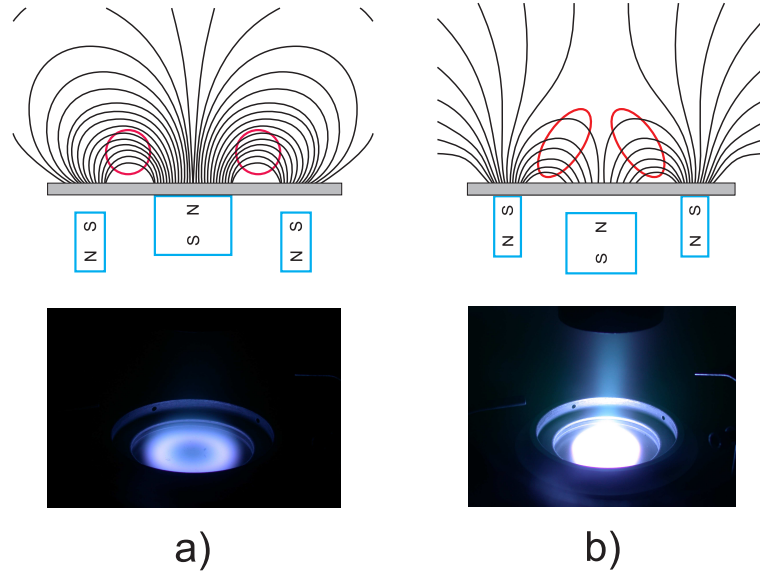
Fig. 3.5: The magnetic field lines and photos of magnetron discharges operated in: **a)** balanced, **b)** unbalanced mode.

trary, their earlier simulations [82] show that electrons in BLM magnetrons escape radially outward.

Understanding the transport processes in crossed electric (E) and magnetic (B) field is essential for understanding the operation of magnetron devices. Therefore the elementary processes as electron, ion and energetic electron transports and sputter processes induced by electric and magnetic field were experimentally studied as well as Monte-Carlo modelled by *Sheridan et al.* [83, 84, 85]. Using the calculated E-field and modelled B-field as well as measured electron temperature, the electron $E \times B$ and ∇B drift speeds were determined [86]. In the plasma bulk the $E \times B$ drift speeds are distributed in a diagonal region sloping from above the racetrack and terminating close to the discharge axis. The drift speed is slightly reduced with increasing pressure. Typically $E \times B$ speeds were observed about two or three times higher than ∇B drift. The electron drift current ($j_{\mathrm{H}} = n_{\mathrm{e}} \cdot \nabla V_{\mathrm{pl}} \times \mathbf{B}/B^2$) was imaged in 2D maps [76]. The drift current was the highest near by target, localized above race-track, which corresponds to magnetic field line geometry.

The influence of magnetic field on the plasma boundary region adjacent to the cathode target (cathode fall region, sheath) was investigated using a 1D two-fluid model description [87]. For constant and weak magnetic

field (about 0.01 T) in all space, the sheath behaves according to the Child-Langmuir law, with the thickness decreasing as the magnetic field strength is raised. Mirror force in electron fluid description due to the magnetic field gradient was necessary introduced in case of more realistic magnetic field variation close to the cathode.

3.2.1 DC planar magnetrons for thin film deposition

Generally it is difficult to characterize physical and technical parameters of magnetrons because of wide range of their experimental modifications. However, in this chapter there are summarized typical overall parameters of dc planar magnetrons. Negative voltage bias in order of several hundreds volts (usually up to -1.000 V) is applied on the cathode - the target. The diameter of the circularly shaped target is usually from 60 up to 200 mm with the thickness about 7 - 10 mm. Target is made of material to be deposited - mainly Ti, In, Ta, Al, Cu, Zr and other species. As buffer gases are frequently used inert gases (e.g. Ar) with reactive component(s) (e.g. O_2, [88], N_2, [89, 90]) for creation of -oxide or -nitride layers.

Plasma potential near the substrate position is mostly positive, in cw regime, with values near to zero and decreases up to negative values with approaching to the target [76, 86]. Electron temperature or electron energy usually reaches several electronvolts. In Ar discharges at low pressure the EEDF is usually Maxwellian, but very often the so-called double Maxwellian or two-temperatures distributions are met; in the logarithmic plot of second derivative of I-V characteristic two slopes can be distinguished [91]. This two temperature distribution was observed, e.g., in [92]. The hot component was observed mainly near by the target whereas cold component was dominant far from the cathode.

Furthermore, the ionisation fraction of sputtered particles, which tightly corresponds to deposition rate, is relatively small under conventional conditions. Generally, in conventional magnetrons operated in continuous mode, the electron density is about $n_e \approx 10^{15}$ - 10^{16} m^{-3} at a distance of 10 cm from the cathode [93]. For this reason magnetrons are often modified to operate in pulsed regime.

This means that the instant discharge current in the active pulse can be very high but the average discharge current is low and has similar magnitude as in the systems working in continuous mode. The next important reason of using pulse magnetrons is discharging of dielectric layer or clusters formed on the cathode target during reactive sputtering process of dielectric films [94, 95]. Recently, this method has been widely used in many research laboratories and in industrial processes for deposition of many kinds of thin films. This includes deposition of oxides or nitrides by reactive sputtering of metallic target [96, 97]. The modulation frequency is typically selected in a wide range from 100 Hz up to 350 kHz.

Low and mid-frequency pulsed magnetron discharges were carefully theoretically as well as experimentally studied in several works. The repetition frequency 2 kHz (duty cycle 50 %), so-called mid-frequency discharge, was used in magnetron with Ti target by *Bradley* and *Backer* [98, 99]. The discharge with higher modulation frequency 20 kHz with Ti target was studied in [100] and with Ti and Al targets in [101]. Pulsed magnetrons working at high pulsing frequency (100 - 350 kHz) with graphite [102], magnesium [103, 104] and titanium [105] targets were studied as well. Similar modulation frequencies were used for depositions of TiO_x films [106, 107, 108], ZnO, poly-silicon films etc. The measured electron density is $n_e \approx 10^{16} \, \text{m}^{-3}$ in almost all the mentioned works. It is only several times higher than with the magnetron working in continual mode.

High power magnetron sputtering in pulsed regime with duty cycles of 1 % at low repetition frequency 50 Hz, was studied for example in [109, 110]. These so-called low-frequency pulsed discharges use peak power densities of the order of $\text{kW} \, \text{cm}^{-2}$ and can achieve high density plasma. The electron density about $n_e \approx 8 \times 10^{18} \, \text{m}^{-3}$ was reached with Ta target and Ar gas [111, 112]. As it was shown in [113, 114] despite high electron density the deposition rate is low under these conditions and similar to deposition rate in continuous regime. It is caused by small duty cycle ratio - the ratio of active to the idle time of the period - $t_a/T \sim 0.01$. Hence, the compromise between high plasma density and duty cycle has to be found in order to reach high deposition rates at pulsed magnetron conditions.

The pulsed discharges can be operated in a unipolar [109, 112, 115] and in asymmetric bi-polar mode [116, 117]. Comprehensive diagnostic of both modes was carefully done by *Vlcek* [94] by means of time resolved OES, Langmuir probe measurements and time and energy resolved mass spectroscopy.

4. DIAGNOSTIC METHODS

Diagnostic of plasmas plays an important role in all experiments and becomes inseparable part of plasma-assisted technological processes. Knowledge of internal plasma parameters serves either for study of elementary processes or helps to find optimal technological conditions. The comprehensive picture of plasma properties is usually reached due to combination of different diagnostic methods [118]. This chapter treats the diagnostic techniques that were employed in the frame of the thesis - Langmuir probe measurements (single and double probe technique) and optical emission spectroscopy.

4.1 *Langmuir probe diagnostics*

The probe diagnostic of low temperature plasma, developed by Langmuir and Mott-Smith in twenties [119], belongs to the oldest as well as most often used diagnostic methods. The method of the Langmuir probe measurement is based on the estimation of the current-voltage (I-V) characteristic, so-called probe characteristic, of a circuit consisting of two electrodes immersed into the plasma under study. Hence the *single* (the surface areas of both electrodes being in contact with plasma differ by several orders of magnitude) and *double* (the surface areas of both electrodes being in contact with plasma are approximately equal to each other and very small in comparison with the plasma vessel dimensions) probe techniques are distinguished. The both methods, including probe theories, were described, e.g., by *Pfau* and *Tichy* [120].

4.1.1 The working regimes of the single Langmuir probe

The typical I-V characteristic of small cylindrical probe immersed into low-temperature plasma, consisted mainly from neutrals, electrons and positive ions is shown in Fig. 4.1. In the electron acceleration region, where the high positive voltage is applied on the probe, the electron current dominates the total probe current. The positive ions are repulsed and the negative sheath is built around the probe. If the probe bias towards the plasma potential is decreased, the electrons pass through the retarding field. Low energetic electrons do not reach the probe. On the contrary, positive ions are accelerated towards the probe. The probe potential V_p, where the electron and positive ion current compensates each other and the total probe current equals to zero, is called floating potential V_{fl}. An almost pure positive ion current flows to the probe at high negative voltage; the probe is operated in ion acceleration region.
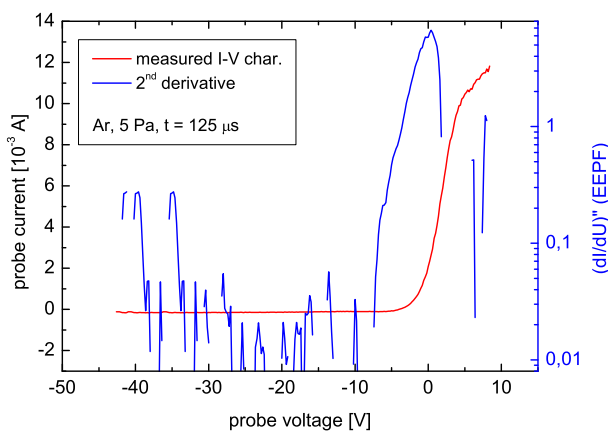
Fig. 4.1: The real single probe I-V characteristic and its 2nd derivative in semi-logarithmic scale measured in pulsed magnetron discharge (Ar, $p = 5$ Pa, $U_{cat} = -580$ V, $f = 250$ Hz, $T_{active} = 150 \mu$s) by time-resolved technique 125μs after ignition.

The working regime of the probe of radius r_p is determined by several parameters; Knudsen number for ions and electron $K_{i,e} = \lambda_{i,e}/r_p$ (where $\lambda_{i,e}$ is the mean free path of ions or electrons respectively) and Debye number $D_\lambda = r_p/\lambda_D$, where $\lambda_D = (\varepsilon_0 k T_e/(e^2 n_e))^{1/2}$ is Debye length, k is Boltzman constant, T_e electron temperature, e elementary charge and n_e electron density.

Another important parameter, which influences charged particles flow on the probe surface, is anisothermicity $\tau = T_e/T_i$; see (1.2). The elementary theory of single cylindrical probe is restricted to the Maxwellian, isotropic plasma with presumption $\tau \gg 1$, i.e. $T_e \gg T_i$.

The thickness of the probe sheath is of the order of several Debye lengths under our experimental conditions (pressure reduced up to several tens of pascal). The average number of collisions of charged particles in the sheath is proportional to the mean free path and can be described as a product $X_{i,e} = (D_\lambda K_{i,e})^{-1}$. Since the sheath thickness depends on the probe potential V_p, the product $(D_\lambda K_{i,e})^{-1}$ is also a function of the probe potential. The number of electron-ions collisions for a given probe potential can be illustrated by the dependence of D_λ on K_i. A graph for $D_\lambda \leq 3$ and $\eta = 15$ (where $\eta = eV_p/kT_e$ is so-called normalized probe potential) is shown in Fig. 4.2. The area where $D_\lambda \leq 3$ is described by the orbit motion limited (OML) theory by *Laframboise* [121].
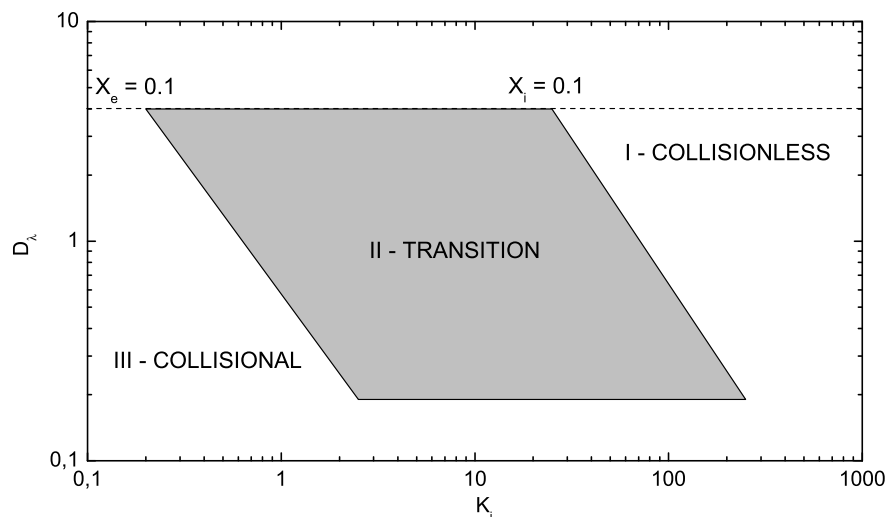
Fig. 4.2: The diagram of working regimes of the probe divided according to collisions in the sheath, $D_\lambda \leq 3$, $\eta = 15$, computed for Ar, [122].

One can see that working regime of the probe is divided into three zones by two curves, $X_{i,e} = 0.1$, of constant number of collisions in the sheath. The criterion $X_{i,e} = 0.1$ means that only 10% of particles collide in the sheath region.

The first zone (I‑collisionless) is determined by $X_{i,e} \leq 0.1$ and electron-ion collisions can be neglected in the probe sheath. The ion as well as electron currents are described using collisionless model ‑ first works by *Langmuir* and *Mott-Smith* [1, 119], later the Bohm criterion was included in so-called ABR theory (*Allen, Boyd, Reynolds*) [123]. The OML theory was further extended by *Bernstein* and *Rabinowitz* who assumed monoenergetic distribution of ions [124] and by *Laframboise* [125], who assumed Maxwell distribution for both electrons and ions.

The second zone (II‑transition) is determined by $X_i \geq 0.1$ and $X_e \leq 0.1$. The electron current can be described using collisionless model. The positive ion collection by a Langmuir probe under the influence of collisions of ions with neutrals in probe sheath is described by collision model. The collision model presents the effect of collisions in form of correction to a collisionless ion model. The most frequently used so-called ABR-Chen model [126] includes the classical Langmuir OML model and the radial motion cold ion approximation.

In the last zone (III‑collision), where $X_{i,e} \geq 0.1$, the collisions of electron as well as ions has to be taken into account. The collision theories were done by *Chou, Talbot, Willis* [127], *Jakubowski* [128] and later by *Zakrzewski* and *Kopiczynski* [129]. *Klagge* and *Tichy* in [130] published collision theory based on collisionless ABR-Chen theory together with Talbot correction. Theory by Zakrzewski and Kopiczynski combined together with theory Talbot and Chou is published in [122].

4.1.2 Determination of basic plasma parameters

From I-V characteristic it is possible to determine basic parameters of the plasma surrounding the probe e.g. plasma potential, mean electron energy, electron density, electron energy distribution function (EEDF). This chapter is focused on determination of basic plasma parameters by means of single cylindrical Langmuir probe. The determination of electron energy distribution function, electron density, electron temperature and plasma potential will be described for plasma containing electrons, only positive ions and no negative ions under the assumption of collisionless regime.

Electron energy distribution function

The transition area of I-V single probe characteristic, measured in collision-less and non-perturbed plasma discharge volume, is influenced by distribution of electron energy $f(\varepsilon)$ commonly called Electron Energy Distribution Function (EEDF). The electron current in the transition region of the probe voltages can be described using EEDF in the form

$$i_{\mathrm{e}}^{(V)} = \frac{1}{4} e n_{\mathrm{e}} A_{\mathrm{p}} \sqrt{\frac{2}{m_{\mathrm{e}}}} \int\limits_{eV}^{\infty} f(\varepsilon) \sqrt{\varepsilon} (\varepsilon - eV) \, \mathrm{d}\varepsilon. \tag{4.1}$$

Here $\varepsilon = m_{\mathrm{e}} v^2/2$ is electron energy, v denotes electron velocity, A_{p} is probe surface and $V = V_{\mathrm{p}} \text{-} V_{\mathrm{pl}}$, where V_{p} and V_{pl} denote probe and plasma potentials, respectively. The second derivative of (4.1) with respect to V yields the so called Druyvesteyn formula [131]

$$f(\varepsilon) = \frac{4}{e^3 A_{\mathrm{p}}} \sqrt{\frac{m_{\mathrm{e}}}{2}} \sqrt{\varepsilon} \frac{\mathrm{d}^2 i_{\mathrm{e}}}{\mathrm{d}V^2}, \qquad (\varepsilon = -eV), \tag{4.2}$$

which gives electron distribution function $f(\varepsilon)$ directly in terms of the measured value of $\mathrm{d}^2 i_{\mathrm{e}}/\mathrm{d}V^2$. Because of further processing it is necessary to know whether EEDF is Maxwellian or not. The Maxwellian distribution function is described

$$f_{\mathrm{maxwell}}(\varepsilon) = \frac{2}{\sqrt{\pi}} n_{\mathrm{e}} (kT_{\mathrm{e}})^{-3/2} \sqrt{\varepsilon} \exp\left(\frac{-\varepsilon}{kT_{\mathrm{e}}}\right). \tag{4.3}$$

A low-pressure discharge has often the electron energy distribution that departs from a Maxwellian one. It can be easily distinguished on the second derivative of I-V characteristic in transition area; the $(\mathrm{d}^2 i_{\mathrm{e}}/\mathrm{d}V^2)$ of Maxwellian distribution is linear to ε (voltage) in semi-logarithmic scale, see Fig. 4.1.

The Electron Energy Probability Function (EEPF) $F(\varepsilon) = \varepsilon^{-1/2} f(\varepsilon)$ is sometimes introduced instead of EEDF [91]:

$$F(\varepsilon) = \varepsilon^{-1/2} f(\varepsilon) = \frac{4}{e^3 A_{\mathrm{p}}} \sqrt{\frac{m_{\mathrm{e}}}{2}} \frac{\mathrm{d}^2 i_{\mathrm{e}}}{\mathrm{d}V^2}. \tag{4.4}$$

Electron density

The probe does not influence the charged particles through the electric field if the voltage bias applied on the probe is equal to the plasma potential V_{pl}. At plasma potential the probe sheath disappears and particles fall on the probe is caused only by chaotic thermal motion. The thermal chaotic currents of electrons $J_{\mathrm{e}0}$ and ions $J_{\mathrm{i}0}$ can be described

$$J_{\mathrm{e}0} = \frac{1}{4} e A_{\mathrm{p}} n_{\mathrm{e}} \sqrt{\frac{8kT_{\mathrm{e}}}{\pi m_{\mathrm{e}}}} \tag{4.5}$$

and

$$J_{\mathrm{i}0} = \frac{1}{4} e A_{\mathrm{p}} n_{\mathrm{i}} \sqrt{\frac{8kT_{\mathrm{i}}}{\pi m_{\mathrm{i}}}} \tag{4.6}$$

where m_{e}, n_{e} or m_{i}, n_{i} denote masses and densities of electrons or ions, respectively, A_{p} is probe surface. It is easy to show, using the quasineutrality condition $n_{\mathrm{e}} \approx n_{\mathrm{i}}$ and large difference of masses $m_{\mathrm{e}} \ll m_{\mathrm{i}}$, that the ion current at plasma potential is much smaller than the electron one and can be neglected. Hence, the n_{e} is determined from the probe current in plasma potential $i(V_{\mathrm{pl}})$:

$$i\left(V_{\mathrm{pl}}\right) = J_{\mathrm{e}0} - J_{\mathrm{i}0} \approx J_{\mathrm{e}0} = \frac{1}{4} e A_{\mathrm{p}} n_{\mathrm{e}} \sqrt{\frac{8kT_{\mathrm{e}}}{\pi m_{\mathrm{e}}}} \tag{4.7}$$

However the necessity of knowing T_{e} may complicate the precise analysis. The T_{e} has to be determined from I-V characteristic at first, described in the next part of the chapter, and its absolute value is burdened by computational error which increases total error of n_{e}.

Under OML conditions ($r_{\mathrm{s}} \gg r_{\mathrm{p}}$, where r_{s} denotes the space sheath thickness at $D_{\lambda} \to 0$, and r_{p} is probe radius) the electron current in the transition region of probe voltages is described [1, 119]

$$\frac{i_{\mathrm{e}}}{J_{\mathrm{e}0}} \sim \exp\left(\eta\right), \quad \eta < 0, \tag{4.8}$$

where i_{e} is the real electron probe current, $J_{\mathrm{e}0}$ was defined by (4.5) and η is

dimensionless probe potential

$$\eta = \frac{e\left(V_{\mathrm{p}} - V_{\mathrm{pl}}\right)}{kT_{\mathrm{e}}}. \qquad (4.9)$$

According to the OML regime the electron current in the electron acceleration region $\eta \gg 1$ should be square root dependent on the V_{p}, referenced to the V_{pl}. Hence, the slope of i_e^2 vs. V plot is proportional to n_e^2 and the electron density can be determined from

$$\frac{\Delta i_e^2}{\Delta V} = \frac{2}{\pi^2} A_{\mathrm{p}}^2 \frac{e}{m_{\mathrm{e}}} n_{\mathrm{e}}^2. \qquad (4.10)$$

Using (4.10) the n_{e} is computed directly from the probe data, no other quantities as T_e are required. Thus the computational error is reduced at minima. However, care should be taken when measuring by probe in electron accelerating regime in an active discharge.

The estimation of n_{e} directly from EEDF (4.2) is possible, too. The method is based on integral evaluation

$$n_{\mathrm{e}} = \int\limits_0^\infty f\left(\varepsilon\right) \mathrm{d}\varepsilon. \qquad (4.11)$$

However, the results are burdened by larger computational error caused by inaccurate estimation of $f(\varepsilon) \sim \mathrm{d}^2 i / \mathrm{d}V^2$ especially at low energies and proper limits of integral.

Electron temperature

The easiest method of electron temperature evaluation in Maxwellian plasma is based on the formula

$$T_{\mathrm{e}} = \left[\frac{\mathrm{d}\log i_{\mathrm{e}}\left(V\right)}{\mathrm{d}V}\right]^{-1}. \qquad (4.12)$$

Using (4.12) together with (4.8), we see that the inverse slope of the logarithmic electron probe current with respect to probe voltage (in volts) gives

directly T_e in volts,

$$i_e \sim \exp\left(\frac{eV}{kT_e}\right), \quad [T_e] = \mathrm{K}. \tag{4.13}$$

In order to get $i_e(V)$, the positive ion current is often approximated by linear relation.

The mean electron energy E_m can be determined using EEDF again as

$$E_m = \langle\varepsilon\rangle = \frac{1}{n_e}\int_0^\infty \varepsilon f(\varepsilon)\,\mathrm{d}\varepsilon. \tag{4.14}$$

The effective temperature defined as $T_{eff} = 2/3\langle\varepsilon\rangle$ is a suitable characteristic for non-Maxwellian plasma. For Maxwellian plasma $T_{eff} = T_e$.

Plasma potential

Plasma potential can be determined as probe potential at which occurs cross of the second derivative of I-V characteristic. The electron current is a convex function in electron retarding region while concave in electron acceleration region. Hence, plasma potential V_{pl} is a point where the second derivative changes sign from positive to negative values. The method was experimentally verified in [132].

Another method is based on determination of difference between floating V_{fl} and plasma V_{pl} potentials. For the probe data evaluation from transition part of I-V characteristic it is useful to separate i_e and i_i (we are able to measure only the total probe current). The i_i can be approximated by so-called double logarithmic approximation [133]. Hence, in the region $\eta < 0$

$$i_e = J_{e0}e^{-|\eta|}, \tag{4.15}$$

$$i_i = J_{i0}(1 + |\eta|)^\kappa. \tag{4.16}$$

where $J_{e,i0}$ is thermal electron (4.5) or ion (4.6) current respectively and κ is a real positive exponent (for OML regime and cylindrical probe usually $\kappa \approx 0.5$).

The electron (4.15) and ion (4.16) approximations should be equal to each other in floating potential. Then the V_{pl} is a root of the equation

$$J_{i0} \left(1 + |\eta_{fl}|\right)^{\kappa} = J_{e0} e^{-|\eta_{fl}|}, \tag{4.17}$$

where $J_{e,i0}$ are defined in (4.5) and (4.6) and $\eta_{fl} = e \left(V_{fl} - V_{pl}\right) / kT_e$. The disadvantage of the described method lies in necessity to know T_e. Assuming Maxwellian plasma we can determine the T_e from the slope of 2nd derivative of the **total** probe current in the transition region of probe voltages. That requires assumption of negligible 2nd derivative of the ion current characteristics, which is not so restrictive.

4.1.3 Double probe technique

Double probe technique is another probe configuration. Its main advantage is that it can be used for diagnostics of discharges where ground electrode is not well-defined; e.g. in diagnostic of electrodeless discharges. The double probe method, originally proposed by *Johnson* and *Malter* [134], is based on I-V characteristic measurement when voltage is applied between two small identical electrodes ($A_{p1} \approx A_{p2}$) immersed in plasma. The probes are usually placed close to each other so that is possible to assume that the plasma parameters are the same at both probe positions.

The double I-V characteristic, measured in surfatron discharge, is depicted in Fig. 4.3. A voltage $U_d = U_1 - U_2$ is applied between probes 1 and 2, but the entire system is not connected to any electrode. Since the electron velocities are much higher than the ion ones, the both probes in general must be negative with respect to space potential, the system is fully floating. This condition can be violated only if one probe is larger that the other. The I-V characteristic course is symmetric if $A_{p1} = A_{p2}$. The second derivative of measured I-V characteristic serves for estimation of inflection point of the characteristic. That enables assessment of measured data quality (data offset, probes uniformity etc.).
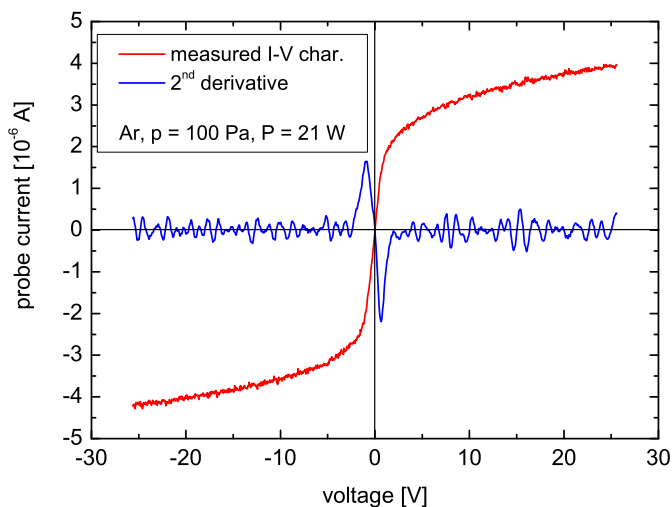
Fig. 4.3: The real double probe I-V characteristic and its 2$^{\text{nd}}$ derivative of surfatron produced discharge (Ar, $p = 100\,\text{Pa}$, $P = 21\,\text{W}$ - "plume" shape discharge) measured at the distance 5 mm from the nozzle outlet.

At $U_{\text{d}} = 0$, both probes are at floating potential and total current $I_{\text{d}} = 0$. If U_{d} is made slightly positive, then U_1 is less negative and U_2 more negative. Thus more electrons flow to probe 1 and fewer to 2, i.e. $i_{\text{e1}} > i_{\text{e2}}$. This results in a current I_{d}. For a large U_{d} the probe 2 will be very negative, $i_{\text{e2}} \ll i_{\text{e1}}$, drawing ion saturation current. Probe 1 will still be negative, but close enough to V_{pl} to collect a sufficient electron current to cancel the ion current to probe 2, $i_{\text{e1}} \approx i_{\text{i2}} \approx I_{\text{d}}$. Thus the probe characteristic assumes the shape of the saturation ion characteristic of probe 2. With negative voltage U_{d} the current is reversed. This qualitative description reveals that the total current to the system can not be higher then the saturation ion current. Hence, the current measured by double probe is lover about several orders of magnitude compared to single probe method.

The following equation holds

$$i_{\text{e1}} + i_{\text{i1}} = -\left(i_{\text{e2}} + i_{\text{i2}}\right) = I_{\text{d}}, \tag{4.18}$$

where $i_{\text{e1}} = i_{\text{e1}}(U_1)$, $i_{\text{i1}} = i_{\text{i1}}(U_1)$ and $i_{\text{e2}} = i_{\text{e2}}(U_2)$, $i_{\text{i2}} = i_{\text{i2}}(U_2)$. In case of a Maxwellian EEDF it is possible to use the following expression for the both

electron probe currents i_{e1}, i_{e2}

$$i_{e1,2} = i_e \left(U_{1,2} = 0 \right) \exp \left(\frac{eU_{1,2}}{kT_e} \right). \tag{4.19}$$

The current in the double probe circuit is given by

$$I_d \left(U_d \right) = i_{i1} \left(U_1 \right) + i_{e1} \left(0 \right) \exp \left(\frac{eU_1}{kT_e} \right), \tag{4.20}$$

$$-I_d \left(U_d \right) = i_{i2} \left(U_2 \right) + i_{e2} \left(0 \right) \exp \left(\frac{eU_2}{kT_e} \right). \tag{4.21}$$

If the double probe characteristic is differentiated with respect to U_d, we obtain the expression for the electron temperature T_e [120]

$$\frac{kT_e}{e} = \left[2 \left(\frac{dI_d}{dU_d} \right)_{fl} - \frac{1}{2} \left(\frac{di_{i1}}{dU_d} + \frac{di_{i2}}{dU_d} \right)_{fl} \right]^{-1} \cdot \frac{2 \left(i_{i1} \right)_{fl} \left(i_{i2} \right)_{fl}}{\left(i_{i1} \right)_{fl} + \left(i_{i2} \right)_{fl}}, \tag{4.22}$$

where $(i_{i1,2})_{fl}$ denotes the extrapolated dependence of the ion current at $U_d = 0$.

A modification of this procedure is based on the estimation of the so-called Γ-function, $\Gamma = i_{e1}/i_{e2}$. The electron temperature T_e is determined from the slope of the dependence $\ln(\Gamma)$ vs. U_d

$$\ln \left(\Gamma \right) = -\frac{eU_d}{kT_e} + \ln \left(\frac{A_1}{A_2} \right). \tag{4.23}$$

The method is described in detail [120, 118].

4.2 Optical emission spectroscopy

Optical emission spectroscopy (OES) is often used for diagnostics of different types of plasmas. This, in principle contactless, method is based on measurements of light emission radiated outwards from plasma volume. The light emission, in wavelength range of 200-900 nm, produced by spontaneous emission of excited atoms, ions and molecules, will be discussed below.

Atoms and molecules have determined energetic levels. A quantum of energy is emitted when a particle transits from higher to lower energetic state in according with the equation

$$h\nu = E_2 - E_1 \tag{4.24}$$

where E_2 is energy of higher and E_1 is energy of lower energetic state, h is Planck constant and ν is the frequency of the emitted quantum. The line spectrum (observed at so called bound-bound transition, i.e. transition between two discrete energetic levels) and continuum spectrum (observed at so called free-bound and free-free transitions - one or both energy levels lay in energy continuum, e.g. braking radiation) has to be distinguished [135].

The intensity of spontaneously emitted radiation for the particular transition $E_{i2} \rightarrow E_{i1}$ between discrete states of particle i is described by the equation

$$I_{21} \approx A_{i21} N_{i2} h\nu_{21}, \qquad [I_{21}] = \text{W} \cdot \text{m}^{-2} \tag{4.25}$$

where I_{21} is spectral line intensity for the transition, A_{21} is spontaneous emission probability of the quantum with the frequency ν_{21}, and N_{i2} denotes the density of particle i on the excited energy level E_{i2}. The intensities enable to determine population of excited states and subsequently to identify the transition in the system of levels.

4.2.1 Determination of vibrational temperature of N_2 molecules

The vibrational temperature of N_2 molecule in the state $C^3\Pi_u$ can be determined from the 2nd positive system of molecule N_2. The 2nd positive system $(C^3\Pi_u \longrightarrow B^3\Pi_g)$ consists of vibrational-rotational lines grouped into the vibrational bands according to the change of vibrational numbers.

The integral intensity of vibrational bands $I_{v',v''}$ of the system are described by the equation

$$I_{v',v''} = \text{const.}\nu^4 p\left(v', v''\right) \exp\left[-\frac{E_{v'}}{kT}\right], \tag{4.26}$$
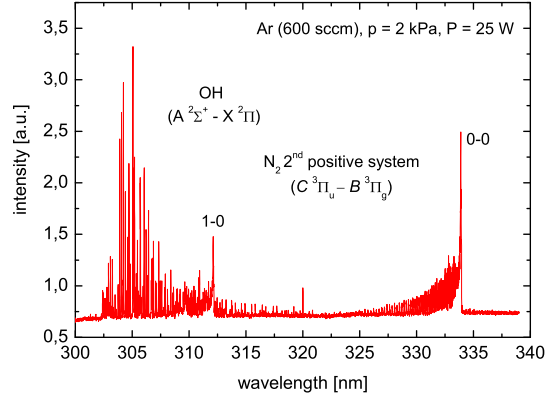
Fig. 4.4: Sample of the 2nd positive system of molecule N$_2$ and OH system measured in Ar surfatron produced discharge $p = 2$ kPa, $P = 25$ W, $z = -3$ mm below the tube outlet.

where ν is the frequency of vibrational band, $p(v', v'')$ is the Franck-Condon factor of the electronic-vibrational transition, v' and v'' are vibrational quantum numbers and $\exp\left[-E_{v'}/kT\right]$ denotes Boltzmann factor.

The fine structure of rotational lines, forming the head band, has to be included into the calculation. Hence, the rotational quantum number J_h, limiting the band edge, and the number of lines ΔJ has to be determined. The triplet of rotational line of P branch can be described by the expression for singlets [136]. Then the total intensity of head vibrational band is given by the equation [137]

$$I_{J, J+1}^{v'} = \text{const } \nu_h^4 \, p(v', v'') \, J_h \Delta J \exp\left[-\frac{E_{v'} + hcB_{v'}J_h(J_h + 1)}{kT}\right], \quad (4.27)$$

where J_h is described by the equation

$$J_h = \frac{B_{v'} + B_{v''}}{2(B_{v'} - B_{v''})}, \quad (4.28)$$

and ΔJ is equal

$$\Delta J = \left(\frac{\Delta\nu}{B_{v'} - B_{v''}}\right)^{1/2}. \quad (4.29)$$

The quantities $B_{v'}$ and $B_{v''}$ denotes rotational constants. These constants are known and have been already published, e.g. in [138].

In our case the vibrational temperature was determined from the intensity of vibrational bands in the 2nd positive system of N$_2$ with unresolved rotational band structure using equation (4.26). The vibrational temperature in ground state and the vibrational temperature in excited state, should be equal at the condition of full thermodynamic equilibrium (FTE). However, it is impossible to reach the equilibrium in our investigated low-temperature plasma systems. The vibrational temperature is used to approximate the electron temperature.

4.2.2 Determination of rotational temperature of OH radicals

The rotational temperature can be determined from the fine structure of rotational lines e.g. lines of OH radicals. Molecules of H$_2$O are often identified as impurities in spite of high-vacuum conditions. These impurities, which are generally unwanted, with weak spectrum intensity, can be used for determination of rotational temperature.

The rotational temperature was calculated from transitions $^2\sum^+$ (mainly $A^2\sum^+ \rightarrow X^2\prod$) of 0-0 band of OH system [139]. The intensity of such rotational line is described by

$$I_{\mathrm{r}} = \mathrm{const.}\nu^4 \left(2J+1\right) i \exp\left[\frac{-B'J\left(J+1\right)hc}{kT_{\mathrm{r}}}\right], \qquad (4.30)$$

where ν is frequency of spectral line, J is rotational quantum number of upper state, B' denotes rotational constant of upper vibrational state, i is intensive factor for the transition, c is light velocity and T_{r} denotes rotational temperature. It was shown in [140] that the rotational temperature approximates the temperature of neutral particles with good agreement. The method of rotational temperature evaluation was described in detail e.g. in [141].

5. EXPERIMENTAL RESULTS AND DISCUSSION OF SURFATRON PLASMA DIAGNOSTICS

The author, in the frame of doctoral study, developed a microwave plasma source of jet type based on surfatron principle and working at frequency 2.45 GHz. The plasma generated by the source in wide range of experimental conditions was subject of detailed diagnostics. The chapter includes three main parts: **(i)** description of surfatron plasma source together with Langmuir probe and optical emission spectroscopy diagnostics devices, **(ii)** results and discussion of surfatron discharge diagnostics with respect to possible future technological applications - probe investigation (single and double probe technique) in continuous and pulsed regimes and optical emission spectroscopy measurements of plasma column in the quartz nozzle as well as of plasma exiting the nozzle, **(iii)** first results of bio-technological applications. As mentioned in *Preface* all data presented in graphs in following chapters are interlaid by B-spline curves.

5.1 Experimental setup based on surfatron

The configuration is shown in Fig. 5.1. The commercial (Sairem) surfatron (1) and microwave generator (Sairem GMP 03KE/D) working in the power range 0 - 300 W were used for plasma generation. The generator operates in continuous as well as in pulsed regimes. An external source of pulses was necessary; function generator Agilent 33120A was used in pulse mode. The amplitude of pulses controlled incoming microwave power, $1 \, \text{V} \approx 30 \, \text{W}$.

Experimental arrangement comprise of a vacuum vessel (2) made from stainless steel. The upper flange (3) of the vessel was made of plastic in order to
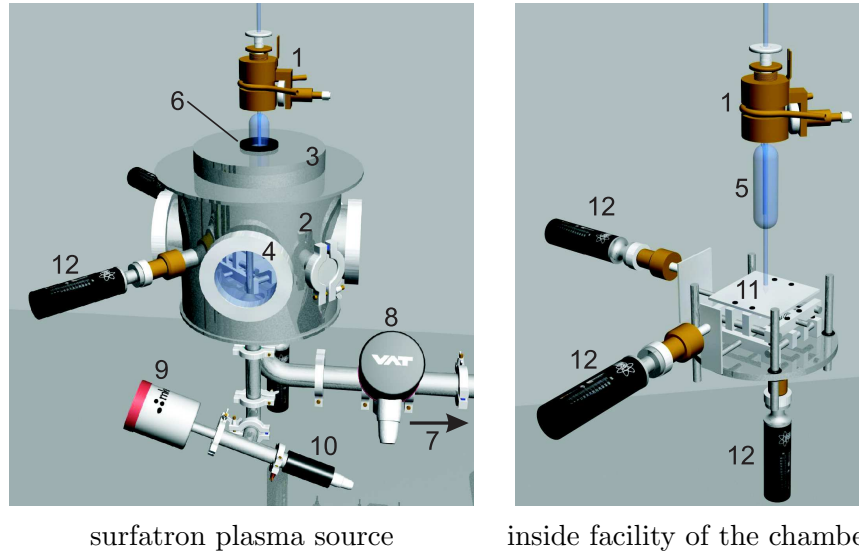
surfatron plasma source   inside facility of the chamber

Fig. 5.1: Experimental setup based on surfatron working with frequency 2.45 GHz.

enable the propagation of the surface wave into the vessel. Four windows (4) in the vessel served for observation of the discharge, optical emission spectroscopy diagnostic and as ports for handling of samples into and out of the chamber. The whole system was screened by a perforated copper tin to protect an operator from power radiation.

The quartz tube of 8 mm outer and 6 mm inner diameter was inserted into the surfatron cavity. The end of the tube (5) protruded into vessel, using silicon O-ring sealed PTFE feed-through (6). The PTFE material was used because of its good thermostability. The quartz tube was designed as two coaxial cylinders at the bottom part protruding through the plastic flange. The space between both tubes was cooled by compressed air to protect plastic from overheating. The working gas flew through the tube. The microwave power was coupled to the surfatron resonator cavity and caused ionisation of flowing gas. Plasma created in this manner was sustained further downstream by a surface wave and exited out of the open tube end. The length of the plasma column in the tube (distance surfatron gap - the end of the nozzle) was about 180 mm. Plasma exiting the tube had a specific shape given by experimental conditions (mainly power, pressure and gas mixture ratio), see Fig. 5.2. So called plasma "plume" was usually created in pure Ar under lower

pressures. Fog-like form of discharges, observed mainly in reactive mixtures Ar/O_2 and Ar/N_2 at higher pressures, was probably caused by long-lived metastable particles of oxygen or nitrogen.
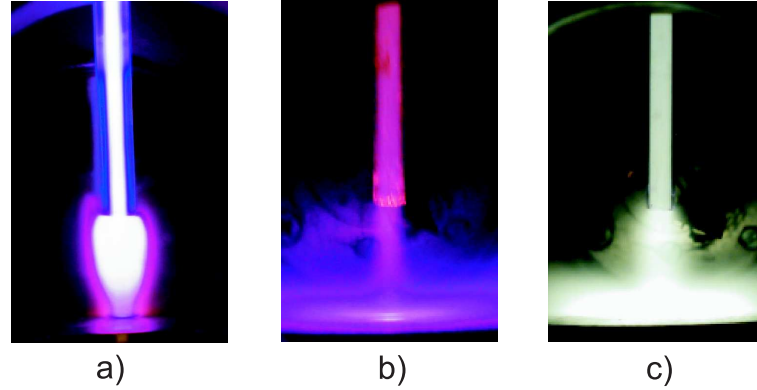

Fig. 5.2: Typical shapes of surfatron produced plasmas at different experimental conditions. "Plume" shape at lower and fog-like form at higher pressures. **a)** Ar, $p = 1\,\mathrm{kPa}$, $P = 20\,\mathrm{W}$, **b)** Ar/N_2, $p = 4\,\mathrm{kPa}$, $P = 100\,\mathrm{W}$, **c)** Ar/O_2, $p = 4\,\mathrm{kPa}$, $P = 150\,\mathrm{W}$. Outer tube diameter is $8\,\mathrm{mm}$.

The flow rates of the working gases were controlled by MKS mass flow-controllers (operated by control unit MKS PR 4000), with ranges to 10, 1.000 and 10.000 sccm. Required gas consistences were mixed. As working gases technical Ar, N_2 and O_2 with purity grade 4.6 were used. The gases were stored in standard pressurized cylinders equipped by reducers. The total flow rate of working gas mixture was usually kept constant, typically at 600 sccm.

The volume of the vessel was continuously pumped out by a large rotary vacuum pump Lavat RV 100/1 (7) down to ultimate pressure of the order of one pascal. The stepping-motor-controlled butterfly VAT valve (8) was situated between the vessel and the vacuum pump. The valve controlled the pumping speed thus allowing setting of the desired pressure in the chamber independently of the working gas flow rate. The valve was controlled by VAT control unit PM-3. Pressure in the vessel was sensed by MKS Baratron 626A (9) controlled via MKS unit. The baratron was calibrated from 0 Pa up to 1 atm. More accurate measurement at lower pressures (0.1 - 100 Pa) was achieved by Pirani vacuum gauge (10) controlled by Lavat VPR1 unit. There was a possibility to connect the MKS and the VAT control units feedback-wise, which kept the desired pressure in the vessel automatically.

The table (11) movable in three dimensions was inserted in the vessel. The upper part of the table laid on two slides movable in perpendicular directions x and y. The movement was realised via linear vacuum feed-through Huntington L21 equipped by stepping-motors (12). The motors, powered by external source, were controlled via computer equipped by LabView software application. Planar samples could be treated homogeneously by this way. In vertical direction z the table was moved via feed-through Huntington L20 (hand-operated). In such way the distance between the nozzle outlet and the table could be set. The table was also used as a movable probe holder during probe measurements. This equipment allowed to move the probe (probes) independently in three dimensions. The table was electrically isolated by the PTFE separators; isolation was important for single probe measurement.

Single as well as double probe method were used for diagnostic; theory of both can be found in previous chapter 4.1. Tungsten wire, of diameter $75\,\mu$m with length $5\,$mm was used for a probe(s) construction. Surfatron discharge is electrodeless in principle. Hence, in order to make single probe measurements, we had to employ the reference electrode. An auxiliary reference electrode was made of stainless steel plate bent into the cylindrical shape with a narrow slit. For the measurements of radial profile the probe bent in right angle was used. This arrangement allowed to measure in a more homogeneous volume of plasma column with respect to assumed radial distribution.

5.1.1 Probe data acquisition system

The probe data were sampled by PC-controlled measuring system [142] in continuous as well as in time resolved regime. The probe circuit was fully floating, i.e. isolated from the control part of the system. The probe current was converted to voltage via an operational amplifier with low input bias current. Its output voltage was fed to isolation amplifier, amplified and measured by the 12-bit A/D converter. Two floating D/A converters connected in series formed the probe bias. The first D/A converter - waveform generator - generated a variable probe bias in 1024 levels. The second D/A converter

served for setting of the dc probe bias. The achieved span of the probe bias was 50 V. This configuration allowed using both, single and double, probe techniques. The difference lied only on distinct connection of probe circuit and using more sensitive input amplifier during double probe measurement.

Trigger circuit was provided by adjustable time delay; after that started the measurement of one probe characteristic point (i.e. A/D conversion of the probe current). The digital data were written into the static RAM buffer. After the whole probe characteristic had been recorder into the buffer, it was read out into the computer by a control program. Signal generator, Agilent 33120A as well as trigger circuit were connected with the dual-channel digital oscilloscope Tektronix TDS-1012. That allowed observation and comparing signals from generator and trigger circuit, i.e. delay adjustment, during the course of the measurement. The acquired data were pre-processed by averaging methods and saved to a standard text file. Program Start [143] or programme procedure written in Matlab [144] were used to process the probe data.
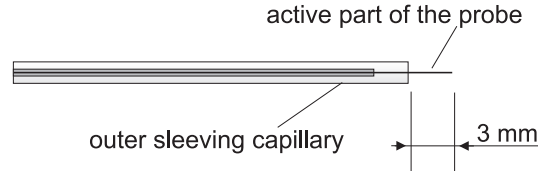
Fig. 5.3: Detail of probe arrangement preventing the probe from short-circuiting by deposited material.

During the measurements in a reactive plasmas with admixtures of O_2 and N_2 a thin electrically non-conducting film was deposited on the probe surface. The film could affect the measured probe data and could lead to incorrect plasma parameters determination. To minimize this effect, the probe surface was cleaned prior to each measurement by positive ion bombardment, during which the deposited material was sputtered off. The cleaning current about 10^{-5} A through the probe was usually used. The probe wire was sleeved by a double-capillary glass tube with the outer capillary longer than the inner. This arrangement prevented the probe from short-circuiting by a metal-coated sleeve, see Fig. 5.3.

5.1.2   Experimental arrangement for optical emission spectroscopy

The plasma exiting from the tube as well as the plasma column burning in the quartz nozzle was investigated by means of optical emission spectroscopy. The measurements were realised by Jobin Yvon Horiba Triax 550 spectrometer equipped with CCD detector Spectrum One with 2000×800 pixels cooled by liquid nitrogen. The spectrometer was equipped with three gratings 300, 1.200 and 3.600 lines per milimeter. The emitted light was collected by an optical fibre connected with the spectrometer. The entrance slit was typically kept at width $0.3\,\mathrm{mm}$. The spectrometer operation was controlled via PC equipped by proper program.

The end of the optical fibre was situated outside of the vessel close to the quartz window shown in Fig. 5.4. The quartz window also allowed to measure in UV spectra region. Hence, the scanned spectra were in the range $\lambda = (200\,\text{-}\,900)\,\mathrm{nm}$. The CCD detector was able to record only part of the spectra (roughly about $50\,\mathrm{nm}$) during one exposition. Because of this the grating was turned by a stepper motor after each exposition until the overview spectra range was measured. In such configuration the spectrum was scanned during several minutes (up to $3\,\mathrm{min.}$). For measurements of vibrational and rotational temperatures intensities in relative (arbitrary) units are sufficient. In order to calibrate the wavelength range the light source with well-known line spectrum - Hg lamp - was used.

The bare optical fibre has a big entrance aperture angle. Since we intended to make position-resolved measurements the end of the fibre was equipped by an end-piece with the view to reduce the aperture angle. In spite of this radiation was collected from a small solid angle, see Fig. 5.4. The distance between emission light source (plasma column burning in the tube) and the fibre was about $18\,\mathrm{cm}$. This fact caused that emission spectrum was averaged almost over the total radial cross section ($6\,\mathrm{mm}$ was inner diameter of the tube). Hence, this experimental arrangement was used only for spatially resolved investigation of emission spectra in axial direction. For this purpose the position of optical fibre was adjusted by micrometer screw. In graphs presented below the tube outlet is situated at position $z = 0\,\mathrm{mm}$. The neg-
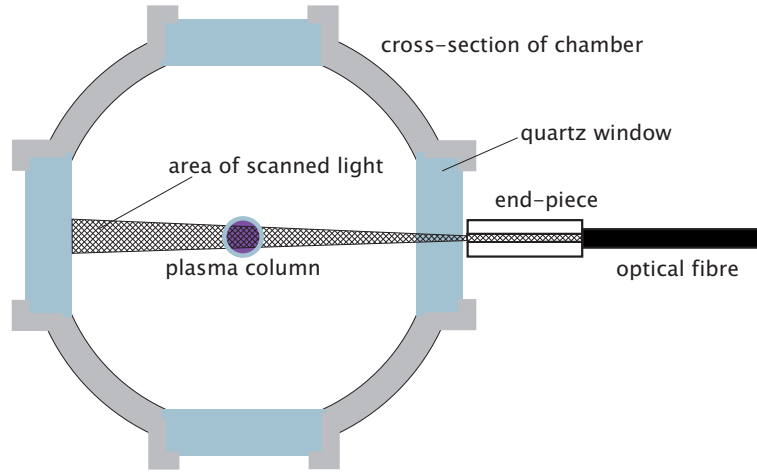
Fig. 5.4: Detail of optical emission diagnostics arrangement with illustrated area of scanned light. The picture represents cross-section of vacuum chamber, end-piece of optical fibre was movable by micrometer screw.

ative values represent position in plasma burning outside the tube, positive values positions upstream of the nozzle end towards the surfatron.

5.2   Diagnostics of surfatron plasma discharge

The surfatron-produced plasma was diagnosed by means of probe measurements and optical emission spectroscopy (OES) with the view of future application in the area of bio-technology. For these practical utilisations rare-gas discharges with small amount of reactive admixtures are frequently used. For this reason Ar/O_2 and Ar/N_2 discharges with volume mixture ratio $590/10$ (sccm) were mostly investigated. These results were compared to those obtained with pure Ar discharge. Primarily, plasma exiting the tube was investigated.

At the beginning the range of conditions, at which the plasma generated by surfatron is sufficiently stable for its precise diagnostics, was studied by simple optical method. As a rule, at lower pressures only low microwave power was needed to sustain the plasma downstream of the end of the nozzle and vice versa. At low pressure and higher power, the plasma generated inside the nozzle did not absorb the whole incoming power from microwave

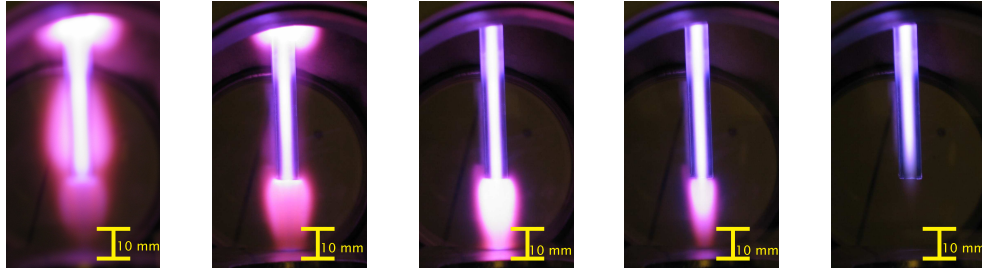*Fig. 5.5:*   Sequence of photographs of surfatron-produced plasma; a)-e) from left. Ar discharge generated at the same power, $P = 21\,\mathrm{W}$, but under different pressures: a) $p_\mathrm{a} = 110\,\mathrm{Pa}$, b) $p_\mathrm{b} = 500\,\mathrm{Pa}$, c) $p_\mathrm{c} = 800\,\mathrm{Pa}$, d) $p_\mathrm{d} = 1.100\,\mathrm{Pa}$, e) $p_\mathrm{e} = 1.500\,\mathrm{Pa}$.

generator, what originated in standing wave pattern in the vacuum vessel. Then the plasma was generated at the places outside of the nozzle where standing wave maxima were located, see Fig. 5.5 a. With increasing pressure in the chamber the power was more substantially absorbed and the standing wave pattern vanished. If the pressure was higher, the incoming power was not sufficient enough to create plasma "plume" and the discharge burnt only inside the tube where the surface wave propagated, Fig. 5.5 e.

The stable working conditions were therefore determined mainly by pressure in the vessel and supplied microwave power. The range of stable surfatron working conditions is displayed as an area between two limit lines in so called "p-P map" in Fig. 5.6. The area above the upper line corresponds to discharge burning outside the tube (Fig. 5.5 a), the area below a lower-bound line is characterised by discharge burning only inside the tube (Fig. 5.5 e). These dependences on power-pressure ratio are essential and make precise diagnostic rather difficult. Change of some input parameters causes change of discharge shape and vice versa.

The presence of admixtures O_2 and N_2 increases power demands at the same pressure. As the incoming power is limited by power source working up to $300\,\mathrm{W}$, the extrapolation of bound–lines in "p-P map" to this maximum power gives pressure limitation, up to which the plasma "plume" can be created. However, at higher pressures, roughly about $4\,\mathrm{kPa}$, in mixtures Ar/O_2 and Ar/N_2 discharges in fog-like form are created, see Fig. 5.2.
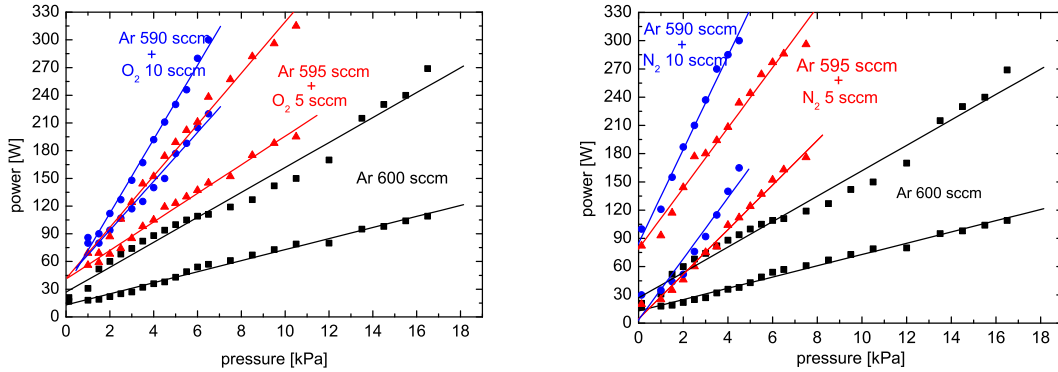
p-P maps of Ar/O_2 discharges.   p-P maps of Ar/N_2 discharges.

Fig. 5.6: p-P maps for discharges Ar/O_2 and Ar/N_2 with mixture ratios 600/0, 595/5 and 590/10 (values in sccm).

5.2.1   Double probe investigation of surfatron discharge

At first surfatron discharge was diagnosed by double probe technique. The double probe technique can be used in wide range of pressures and does not need reference electrode, so that the electrodeless discharges can be easily diagnosed.

Typical shape of double probe characteristic measured in Ar surfatron produced plasma plume is depicted in Fig. 4.3. The second derivative of I-V characteristic serves for estimation and verification of inflection point and its appropriate correction. A code written in Matlab was developed for processing the double probe data. This code interactively fits the measured data by polynomials of low degree, e.g. linear or quadratic, with the aim to extrapolate the values of ion currents of each probe to the floating potential $(U_d = 0)$: $(i_{i1})_{fl}$, $(i_{i2})_{fl}$. In similar manner the first derivative $(dI_d/dU_d)_{fl}$ and the first derivatives $(di_{i1}/dU_d)_{fl}$ and $(di_{i2}/dU_d)_{fl}$ are determined. The electron temperature T_e was then calculated using equation (4.22). No noise-reducing digital filters were applied.

The radial dependences of electron temperature $T_e(r)$ at three distances z from the nozzle exit in Ar discharge are depicted in Fig. 5.7. The tube axis is situated at $r = 0\,\mathrm{mm}$, the nozzle outlet at $z = 0\,\mathrm{mm}$. Only halves of the curves
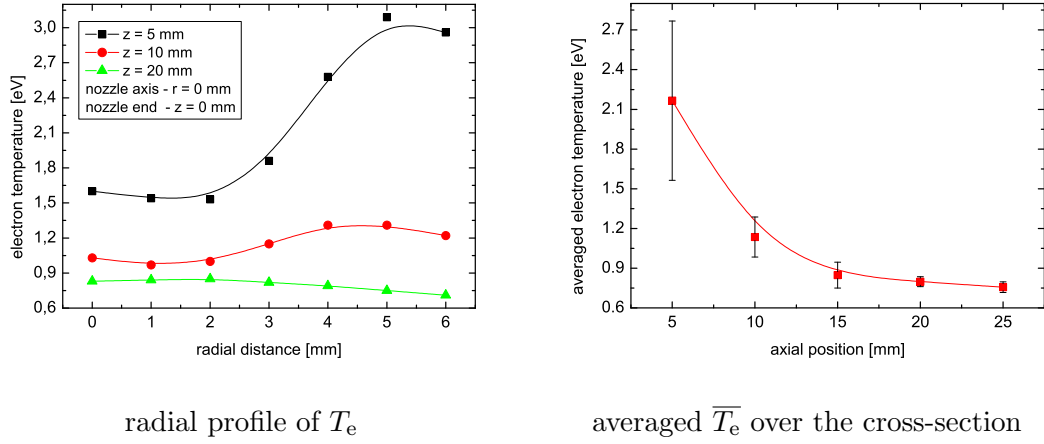
radial profile of T_e averaged $\overline{T_e}$ over the cross-section

Fig. 5.7: The radial T_e profile of Ar discharge ($p = 800\,\mathrm{Pa}$, $P = 21\,\mathrm{W}$) and dependence of $\overline{T_e}$ averaged over the cross-section vs. axial distance z from the nozzle outlet.

are shown supposing radial symmetry of plasma column. Probes bent in right angle were used for measurement of radial dependences, giving better space resolution. The radial course of electron temperature near the outlet of the quartz tube proved strong maxima at the plasma "plume" edges. This profile probably corresponds to azimuthally symmetric $m = 0$ mode of TM surface wave generated in the surfatron. The form of radial profile $T_e(r)$ qualitatively corresponds to spectroscopic measurements of Ar I emission at $\lambda = 549.6\,\mathrm{nm}$ presented in [145]. At larger distances from the outlet ($z = 10, 20\,\mathrm{mm}$) the radial T_e profile becomes flatter. These radial courses correspond to photography of investigated discharge in Fig. 5.5 c.

The $\overline{T_e}$ averaged over cross-section of tube versus axial distance z is depicted in Fig. 5.7, too. $\overline{T_e}$ is the highest near by outlet and decreases with increasing distance from the outlet. The error bar in the graph represents the standard deviation from the mean value.

As it was mentioned above, the stable surfatron discharge can be operated only in the area between bound-lines in "p-P" maps. By another words, stable conditions of discharge generated at one particular input power (e.g. $P = 45\,\mathrm{W}$ in pure Ar) are limited by corresponding range of pressure (for $P = 45\,\mathrm{W}$ the range of pressure is $p \approx 1.5$ - $5.5\,\mathrm{kPa}$), see p-P map in Fig. 5.6.

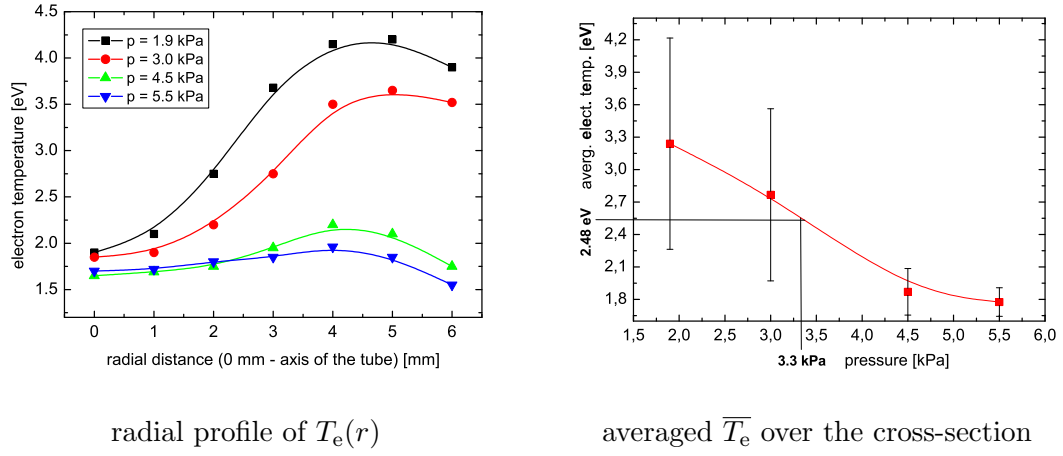radial profile of $T_e(r)$ averaged $\overline{T_e}$ over the cross-section

Fig. 5.8: The radial $T_e(r)$ profile of Ar discharge ($P = 45\,\text{W}$) and dependence of averaged $\overline{T_e}$ over the cross-section vs. pressure; $z = 7\,\text{mm}$ from the nozzle outlet.

The influence of pressure on electron temperature is illustrated in Fig. 5.8. The microwave input power was kept constant, $P = 45\,\text{W}$. Radial courses $T_e(r)$ were measured in the plane $z = 7\,\text{mm}$ below the nozzle outlet. At higher pressures the maximum around the plasma "plume" edges becomes less pronounced. Radially averaged $\overline{T_e}$ decreases towards the higher pressure almost linearly, see right panel in Fig. 5.8. That can be qualitatively explained by energy losses in collisions with neutrals which increase towards higher pressures. Since the input power is kept constant the electron temperature is bound to decrease with increasing pressure.

Large number of double probe measurements was done and gave results about T_e in wide range of pressures and powers in continuous regime. The radially averaged electron temperature measured along a linear segment of power vs. pressure in "p-P" map was more or less constant, but depended on the gas mixture (see Fig. 5.9): in pure Ar - $\overline{T_e} \approx 2.45\,\text{eV}$, in Ar/N$_2$ mixture - $\overline{T_e} \approx 2.25\,\text{eV}$ and in Ar/O$_2$ mixture - $\overline{T_e} \approx 3.05\,\text{eV}$. In Ar discharge generated at power $P = 45\,\text{W}$ at pressure about $p \approx 3\,\text{kPa}$ was measured $\overline{T_e} \approx 2.5\,\text{eV}$, see Fig. 5.9. The similar pressure $p = 3.3\,\text{kPa}$ corresponds to $\overline{T_e} \approx 2.48\,\text{eV}$, averaged from radial profiles of Ar discharge in Fig. 5.8. The rough agreement of radially averaged $\overline{T_e}$ in Figs. 5.8 and 5.9 supports argument that the plasma "plume" generated under stable conditions given by "p-P" map can be char-

acterized by a single "*mean*" value of electron temperature $\langle T_e \rangle$, see Fig. 5.9. An error of this *mean* $\langle T_e \rangle$ at least about 30 % has to be taken into account in the whole range of pressures.
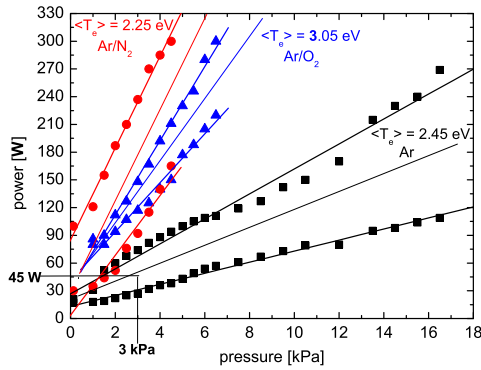
Fig. 5.9: p-P maps of Ar, Ar/O$_2$, Ar/N$_2$ (590/10 in sccm) discharges and their *mean* T_e, axial distance $z = 7$ mm.
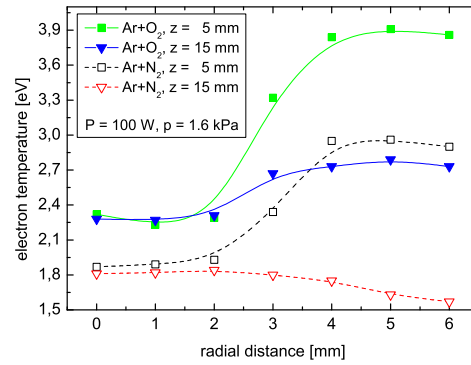
Fig. 5.10: Dependences of radial profiles of T_e in Ar/O$_2$, Ar/N$_2$ (590/10 in sccm); axial distance z is parameter.

The radial profiles of electron temperature $T_e(r)$ in mixtures Ar/O$_2$ and Ar/N$_2$ (590/10 values in sccm, $P = 100$ W, $p = 1.6$ kPa) were also investigated, see Fig. 5.10. Electron temperature is higher and its rise is faster with more pronounced maxima at the edge of plasma column in slightly electronegative Ar/O$_2$ discharge. Higher T_e in Ar/O$_2$ mixture compared to that in Ar/N$_2$ mixture is probably caused by energy release during negative oxygen creation in dissociative attachment reaction, in more detail discussed in next chapter 6.3. Dependence of $\overline{T_e}$ averaged over cross-section diameter on axial distance z in Ar/N$_2$ discharges (not shown) has a similar profile as in pure Ar, depicted in Fig. 5.7. In Ar/O$_2$ this dependence was close to the linear one, especially at lower pressures. That might also be qualitatively explained by energy gain due to dissociative attachment reactions.

5.2.2 Single probe investigation of surfatron discharge

Assuming collisionless criterion and validity of OML theory, the plasma exiting surfatron tube was investigated by single probe technique under low pressure up to 800 Pa. With regard to the relation between power and pres-

sure ("p-P" map, Fig. 5.9), only low input powers could be supplied. In pure Ar discharge the delivered power was $P = 20\,\mathrm{W}$, in mixtures Ar/O_2, Ar/N_2 (590/10) the applied power was $P = 70\,\mathrm{W}$ with pressure $p = 800\,\mathrm{Pa}$ in all cases. Probe immersed in the exiting plasma was distanced $z = 5, 15\,\mathrm{mm}$ from the nozzle outlet. The auxiliary electrode mentioned in previous chapter was used as the reference electrode. The major plasma parameters were determined by standard ways: the electron density n_e was estimated from i_e^2 vs. V_p plot in the electron accelerating regime (4.10), the mean electron energy E_m was computed from the integral of second derivative of I-V characteristic using equation (4.14).

a) n_e radial profile   **b)** E_m radial profile
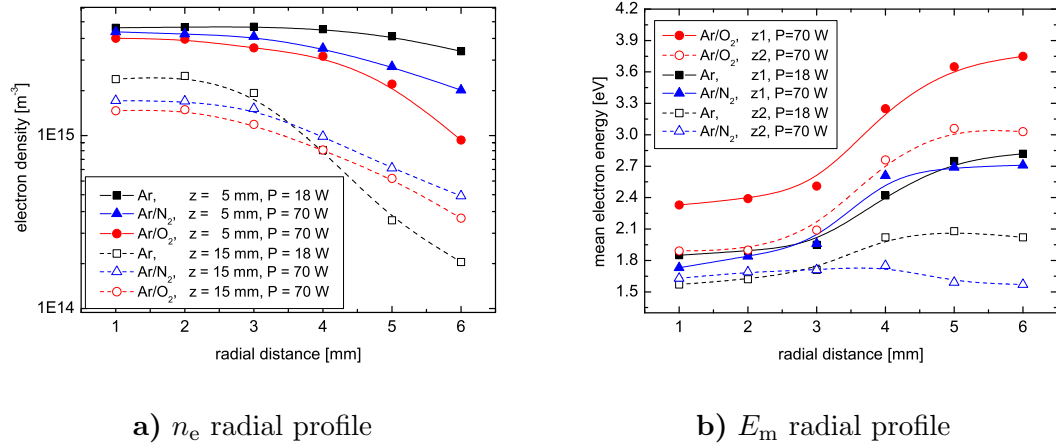
Fig. 5.11: Radial profiles of: **a)** electron density n_e and **b)** mean electron energy E_m. Measured in Ar ($P = 18\,\mathrm{W}$) and Ar/O_2, Ar/N_2 ($P = 70\,\mathrm{W}$) discharges; $p = 800\,\mathrm{Pa}$, z1 = 5\,mm, z2 = 15\,mm.

Electron density n_e reaches $n_e \approx 5 \times 10^{15}\,\mathrm{m^{-3}}$ in the axis of the tube near by the outlet. Radial profile of electron density $n_e(r)$ decreases with the distance from the tube axis. This behavior is more evident in Ar/O_2, Ar/N_2 gas measured mixtures and for distances further away from the outlet, where n_e is almost about one order of magnitude lower, see Fig. 5.11 a. The radial profile of $n_e(r)$ inside the tube, published in [55, 56], exhibits the similar feature: $n_e(r)$ drops significantly from maximum at the tube axis towards the tube wall in agreement with diffusion to the wall as the main loss mechanism [55, 56]. The axial distribution of n_e in SWD discharges inside the tube is essentially different from that, e.g. in a positive column plasma of the glow

discharge, where the n_e almost does not change with axial distance. This is because SWD can only exists provided that the radially averaged electron density $\overline{n_e}$ always decreases with the axial position from the launcher. This slow density decrease is usually linear [50, 60]. Plasma exiting the tube is not further supported by surface wave and $\overline{n_e}$ decreases much faster than in linear manner as it can be deduced from Fig. 5.11 a.

The radial courses of mean electron energy E_m in Fig. 5.11 b exhibit similar behaviour as the electron temperature T_e measured by double probe in Fig. 5.10. Absolute values of E_m have to be considered carefully because of different delivered microwave power: in pure Ar, $P = 18\,\mathrm{W}$ (value close to the case in Fig. 5.7) in gas mixtures Ar/O$_2$, Ar/N$_2$, $P = 70\,\mathrm{W}$ (value close to the results in Fig. 5.10). The differences between E_m and T_e can be qualitatively explained by considering errors arising when integrating measured EEDF and the fact that EEDF is not Maxwellian and hence T_e measured by double probe is just rough approximation. However, the absolute values of radially averaged $\overline{E_m}$ agree with estimated *mean* $\langle T_e \rangle$ of discharges in "p-P" map, Fig. 5.9, within the acceptable error about of a few percent. E_m reaches its maximum at the edge of plasma column and averaged value decreases with the axial distance z, which probably corresponds to azimuthally symmetric $m = 0$ mode of surface wave; the data in Fig. 5.11 b correspond to probe positions $z_1 = 5\,\mathrm{mm}$, $z_2 = 15\,\mathrm{mm}$ from the tube outlet. At larger distances from the tube outlet the radial profile $E_m(r)$ become flatter.

Plasma potential V_{pl} was determined as the probe voltage corresponding to zero-cross of the second derivative of an I-V probe characteristic. Radial as well as axial distribution of V_{pl} was almost uniform with steep decrease at the plasma column edge. Absolute values of V_{pl} reached roughly 5 V.

5.2.3   Time-resolved probe measurements in pulsed surfatron

For the reasons mentioned in chapter *Technological plasmas*, the pulsed regime of plasma source operation is frequently used in plasma supported technologies at present. Further argument may be that in afterglow plasma (after the driving power has been switched off) specific ion-molecule reac-

tions needed for a particular technological process are realized more simply. Other important aim is to increase instantaneous incoming input power and at the same time to decrease exposure time, i.e. to prevent materials from thermal destruction. However, the diagnostic of pulsed discharge is more complicated than diagnostic in cw regime and time-resolved measurements have to be used.

In our case a typical repetition frequency $f = 1\,\mathrm{kHz}$ was kept constant with different duty-cycles about 30, 50 and 80 %, i.e. with active pulse-lengths 300, 500 and 800 μs; the pure Ar and the mixtures $\mathrm{Ar/O_2}$, $\mathrm{Ar/N_2}$ (590/10 ratio in sccm) were used in all cases discussed below. The incoming effective input power averaged over the whole period was $P = 90\,\mathrm{W}$, working pressure $p = 5.6\,\mathrm{kPa}$. Reason of this seemingly inconsistent power resides in pulse regime of plasma source operation; "p-P maps" depicted in Fig. 5.6 are valid only for continuous (cw) regime. When the pulsed regime is used, higher incoming power is necessary.
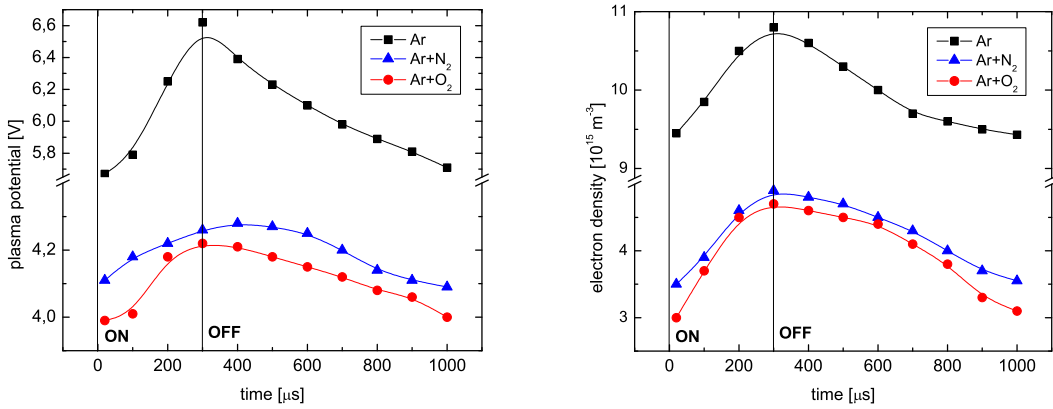
a) time evolution of V_{pl} **b)** time evolution of n_{e}

Fig. 5.12: Time evolution along a single period of: **a)** plasma potential V_{pl} and **b)** electron density n_{e}; $f = 1\,\mathrm{kHz}$, duty-cycle 30 %, $P = 90\,\mathrm{W}$, $p = 5.6\,\mathrm{kPa}$.

Time evolution of plasma potential V_{pl} and electron density n_{e} during one period in pulsed regime of frequency $f = 1\,\mathrm{kHz}$ with duty cycle 30 % are depicted in Fig. 5.12 a and 5.12 b, respectively. One can see that growth of both plasma parameters after ignition ($t = 0\,\mu$s - when the time ON edge of

control pulse comes) is almost linear. When the power is OFF ($t = 300\,\mu$s), the plasma is quenched and V_{pl} and n_{e} decreases. This comparatively slow decrease is probably caused by residual afterglow plasma flowing out of the nozzle. Plasma potential and electron density have similar qualitative behaviour: the highest values belong to the pure Ar discharge. With reactive admixtures O_2 or N_2 V_{pl} and n_{e} become smaller. The lower plasma potential and electron density in Ar/O_2 discharge could be partly due to creation of negative ions by dissociative electron attachment.

In the active phase, the gas flowing through the quartz tube inserted into the surfatron cavity, is ionised and plasma is sustained downstream by surface wave. The energy of surface wave invokes additional ionisation along the tube. If the power is switched OFF, the surface wave vanishes almost immediately but decaying plasma still flows out of the tube. Simple calculation of neutral gas velocity in the tube based on Poiseuill-Hagen law and state equation yielded neutral gas velocity within 100-250 m/s. Detailed calculation of gas velocity is more complicated as the effects connected with viscosity, pressure fall towards the tube end etc. have to be taken into account. The distance between ionisation source and nozzle exit was approximately 200 mm. Hence the time of neutral gas flight between the surfatron and the nozzle end was in the order of 10^{-3} - 10^{-4} s, i.e. comparable with the used discharge repetition period.

The effect of the non-Maxwellian EEDF is manifested by comparing dependences of mean energy E_{m}, calculated from the integral of the second derivative of I-V single probe characteristics, and temperature T_{e}, determined from double probe data at the same experimental conditions, see Fig. 5.13. Absolute values obtained from different techniques are similar with only slight differences of about 20 %. In spite of this relatively small error, the dependences on the working gas-mixture differs: the highest E_{m} was determined in pure Ar discharge and the lowest in Ar/O_2 discharge, contrary to the results for T_{e}. Other difference is connected with the shape of time dependences. Time dependences of E_{m} fall down more steeply than those for T_{e}. Both phenomenons can be qualitatively explained by the form of EEDF. While the
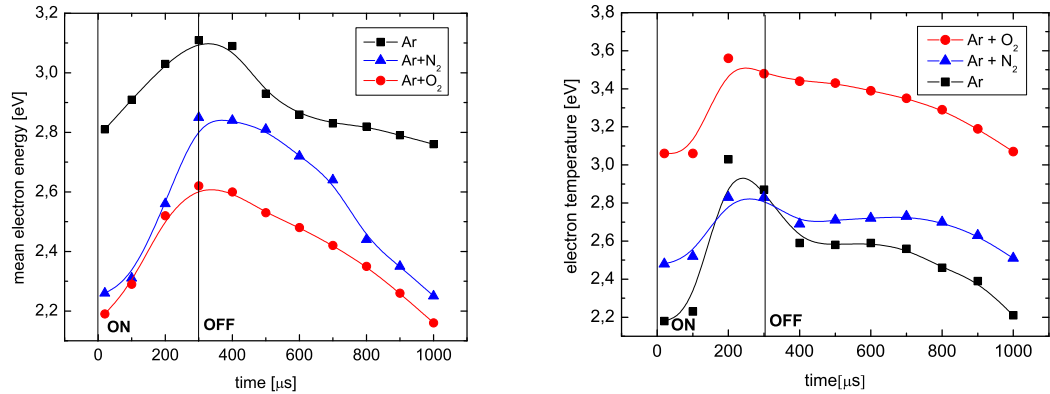
time evolution of T_e (double probe).   time evolution of E_m (single probe).

Fig. 5.13: Time evolution of T_e (computed from double probe measurements) and E_m (determined from single probe measurements) under the same experimental conditions ($p = 5.6\,\text{kPa}$, $P = 90\,\text{W}$, $f = 1\,\text{kHz}$, duty-cycle 30 %).

double probe methods accentuates the body of the EEDF, the determination of E_m via integration takes into account also high-energetic tail of the EEDF. The time evolutions of E_m have their maxima in the active part of the pulse, i.e. roughly 70 μs before the OFF edge, see the right panel of Fig. 5.13.

The energy contained in the system and the number of active species play main role during technological processes. Taking account of this fact we studied time evolution of E_m and n_e mainly in afterglow discharge along one excitation pulse at different duty-cycles, see Fig. 5.14 a and Fig. 5.14 b, respectively, for Ar/O_2 gas mixture. For these figures time $t = 0\,\mu$s corresponds to the OFF edge; then follows the afterglow phase. Time evolution of E_m is depicted in Fig. 5.14 a. If discharge operates in pulsed regime with duty cycle 80 %, the relaxation time is too short and the mean energy is almost constant. Small fall of E_m can be observed at $t = 200\,\mu$s but the difference is not bigger than 10 %. Decrease of E_m in afterglow phase is more obvious for duty cycles 50 % and 80 %, when the fall of mean electron energy is roughly 25 %. Qualitatively similar behavior is seen in Fig. 5.14 b, where time evolution of n_e is depicted. From these results follows that it is possible to reduce the duty cycle and to increase the input power. This option might increase efficiency of technological applications as higher energy is delivered in the system during the pulse and longer idle time prevents overheating.
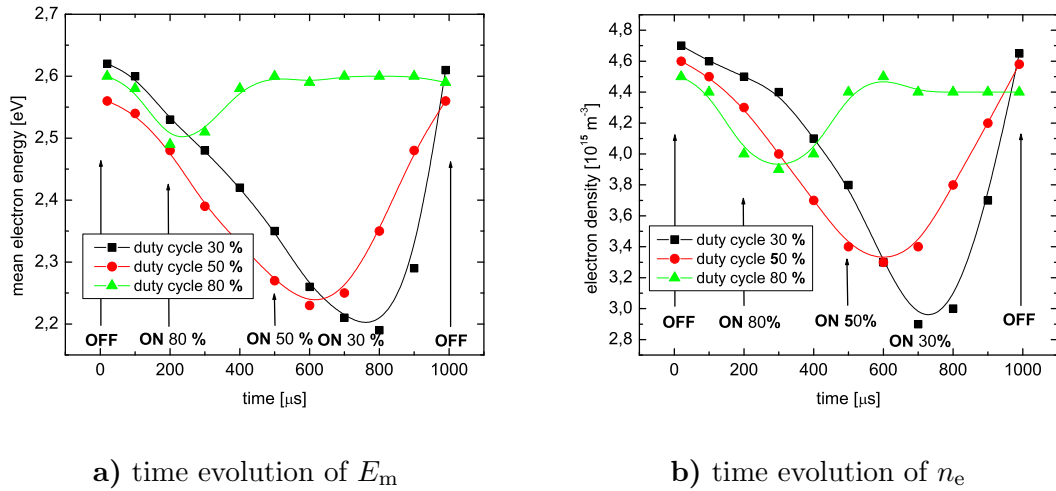
a) time evolution of E_m **b)** time evolution of n_e

Fig. 5.14: Time evolutions of: **a)** mean energy E_m and **b)** electron density n_e under the same experimental conditions - Ar/O$_2$ (590/10), $p = 5.6$ kPa, $P = 90$ W, $f = 1$ kHz, duty-cycle 30, 50, 80 %.

5.2.4   Optical emission spectroscopy of Ar discharge

The emission spectra were measured at various experimental conditions (pressure, power, working gas mixture and fibre position) in the UV-VIS range 200-900 nm. Results are discussed for different gas-mixtures Ar, Ar/N$_2$, Ar/O$_2$. Basic composition of discharges is revealed from so-called overview spectra, i.e. the spectra where all applicable wavelength range is exploited. Axial development of spectral lines or systems and rotational T_r or vibrational T_v temperatures give rough idea about possible reactions and energy contained in the system. In the graphs presented below the outlet of the tube is situated as a role at position $z = 0$ mm - the negative values of axial distance z represent downstream and the positive values upstream position with respect to the nozzle end.

Overview spectrum in pure Ar consisted above all of atomic lines; it is shown in Fig. 5.15. Presence of other impurities as atomic lines of oxygen, molecular bands of nitrogen and OH were registered due to gas impurities or vacuum chamber leakage. The vibrational temperature T_v was calculated from the molecular bands of the second positive system of nitrogen, $C^3\Pi_u \rightarrow B^3\Pi_g$, with a corresponding change of vibrational quantum number $\Delta v = -2$, see Fig. 4.4.
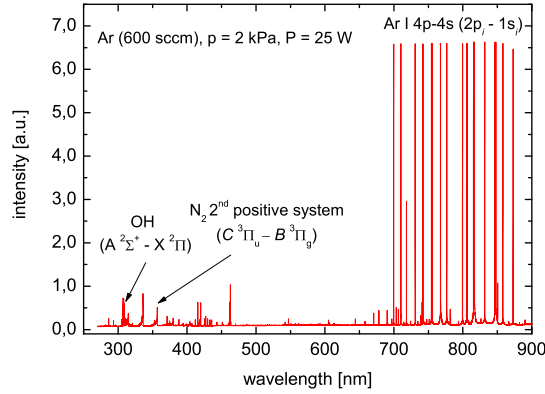
Fig. 5.15: Overview discharge spectra in Ar, $p = 2\,\text{kPa}$, $P = 25\,\text{W}$, $z = \text{-}3\,\text{mm}$.

The axial dependence of vibrational temperature $T_\text{v}(z)$ was almost constant, i.e. T_v was almost independent on axial position, see Fig. 5.16 a. The T_v usually approximately corresponds to electron temperature while in our case the two temperatures differ by factor $(3 \div 4)$; from the spectra calculated $T_\text{v} \sim 3\text{-}7 \times 10^3\,\text{K} \approx 0.5\,\text{eV}$ compared with probe results $T_\text{e} \sim 2\,\text{eV}$ (see e.g. Figs. 5.7, 5.11). Apart from the fact that our plasma is not in thermal equilibrium, while the corresponding equations were derived assuming the thermodynamic equilibrium, the difference might be due to used spectroscopic method, which determines the T_v from broad region of plasma stream including peripheral and axial regions where the electron temperature is lower.
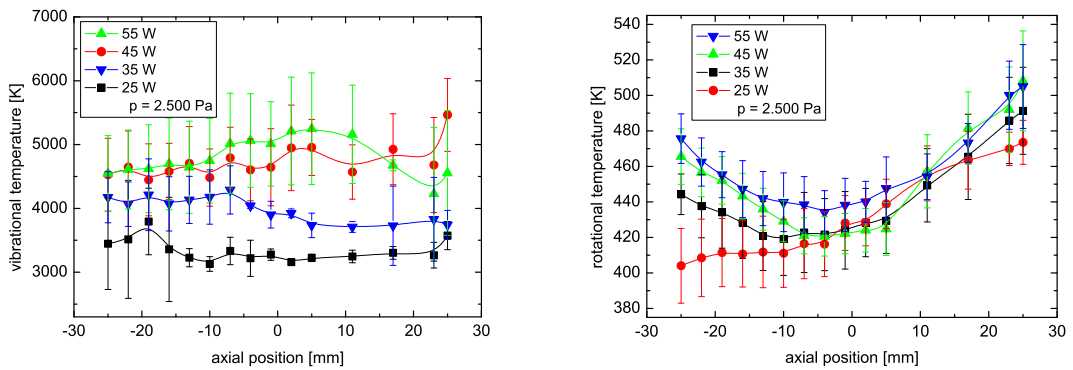
a) axial dependence of $T_\text{v}(z)$.   **b)** axial dependence of $T_\text{r}(z)$.

Fig. 5.16: Axial dependences of: **a)** vibrational $T_\text{v}(z)$ and **b)** rotational $T_\text{r}(z)$ temperatures in Ar discharge; $p = 2.5\,\text{kPa}$, $P = 25, 35, 45, 55\,\text{W}$.

The rotational temperature T_r was calculated from the rotational lines of OH of a transition with $\Delta v = 0$. The resulting T_r dependences for various powers and constant pressure $p = 2.5\,\text{kPa}$ are shown in Fig. 5.16 b. The graphs show that rotational temperature increases with axial distance from the nozzle end when the applied power is higher than $\approx 30\,\text{W}$. The rotational temperature approximates the temperature of neutral particles with good agreement [140]. This fact is important specification for treatment of thermal sensitive materials.

5.2.5   Optical emission spectroscopy of Ar/N_2 discharge

The overview spectra of Ar/N_2 discharge consisted of the atomic lines of argon and the molecular bands of nitrogen (the 1st positive system $B^3\Pi_g \rightarrow A^3\Sigma_u^+$ and the 2nd positive system $C^3\Pi_u \rightarrow B^3\Pi_g$) is shown in Fig. 5.17. Apart from the lines of impurities the atomic lines of oxygen, molecular bands of NO_β ($B^2\Pi \rightarrow X^2\Pi$) and OH ($A^2\sum^+ \rightarrow X^2\Pi$) systems were registered, too.
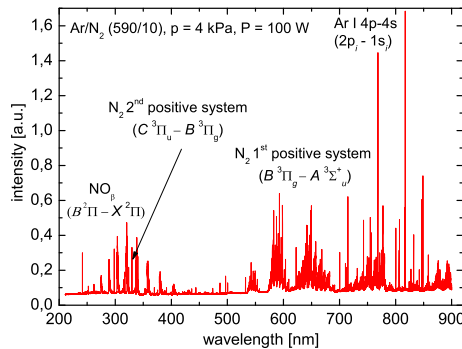
Fig. 5.17: Overview of Ar/N_2 (590/10) discharge spectra, $p = 4\,\text{kPa}$, $P = 100\,\text{W}$, $z = $ -3mm.
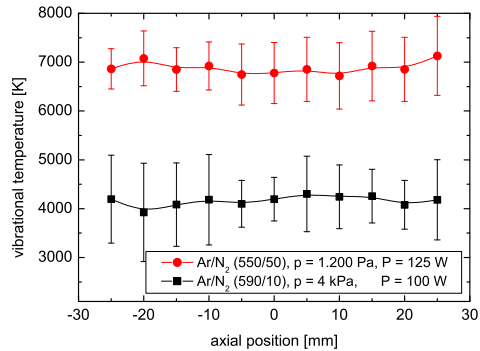
Fig. 5.18: Vibrational temperature T_v vs. axial position.

The vibrational temperature T_v was calculated from the bands of the second positive system of nitrogen with a corresponding change of vibrational quantum number $\Delta v = $ -2. The vibrational temperature dependences vs. axial position for mixtures of Ar/N_2 (550/50 in sccm, $p = 0.12\,\text{kPa}$, $P = 125\,\text{W}$) and Ar/N_2 (590/10 in sccm, $p = 4\,\text{kPa}$, $P = 100\,\text{W}$) are plotted in Fig. 5.18. We see that T_v is approximately constant along the nozzle as well as downstream

of it. Besides, T_v is higher for higher reduced power (the power-to-pressure ratio). Under both mentioned experimental conditions the discharge is produced in fog-like form, see Fig. 5.2 b and compare with respective region in "p-P" map, Fig. 5.6.

a)   b)
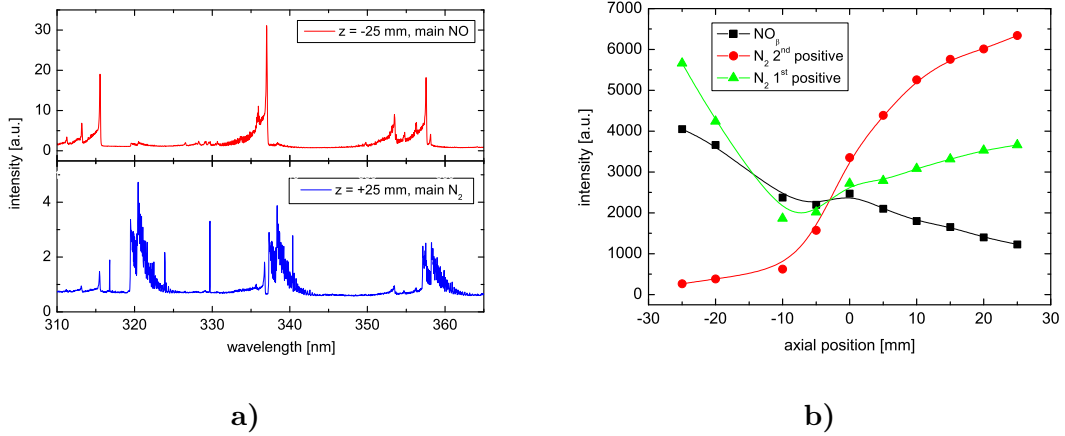
Fig. 5.19: Development of emission spectra and molecular systems on the axial position: **a)** detail of spectra measured at different axial position $z = -25$ mm and $z = +25$ mm, **b)** intensities of N_2 1st and 2nd positive and NO systems vs. axial position. Discharge parameters Ar/N_2 (590/10), $p = 4$ kPa, $P = 100$ W.

The emission spectra changed along the nozzle, see detail of spectra in Fig. 5.19 a. There are depicted intensity ratios of different molecular systems how they changed with the axial position. The axial dependences of N_2 1st and 2nd positive system and NO system intensity were studied for the same experimental conditions; mixture Ar/N_2 (590/10 in sccm, $p = 4$ kPa, $P = 100$ W) and the results are plotted in Fig. 5.19 b. We note that whereas the intensity of the 2nd positive system in the flow direction decreases, the NO intensity increases. The development of the intensity of the 1st positive system with the z co-ordinate is more complicated. We anticipate that the most important reactions involving the concentrations and hence also the intensities of considered species are as follows [146]:

$$\text{N} + \text{O}\ (+\text{N}_2) \longrightarrow \text{NO}^*\ (+\text{N}_2) \quad k\ =\ 9.1 \cdot 10^{-31}\ \text{cm}^6\text{s}^{-1} \tag{1}$$

$$\text{NO}\,(\text{B}\,^2\Pi) \longrightarrow \text{NO}\,(\text{X}\,^2\Pi) + h\nu \quad \text{NO}_\beta\ \text{system} \tag{2}$$

$$\text{N} + \text{NO} \longrightarrow \text{N}_2 + \text{O} \quad k\ =\ 1.6 \cdot 10^{-10}\ \text{cm}^3\text{s}^{-1} \tag{3}$$

$$\text{N} + \text{N} \longrightarrow \text{N}_2 \quad \text{recombination (e.g. to B}\,^3\Pi_\text{g}) \tag{4}$$

$$\text{N}_2\,(\text{B}\,^3\Pi_\text{g}) \longrightarrow \text{N}_2\,(\text{A}\,^3\Sigma_\text{u}) \quad \text{N}_2\ 1^{\text{st}}\ \text{positive system} \tag{5}$$
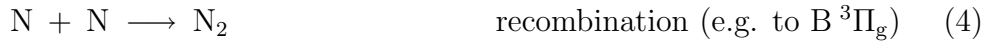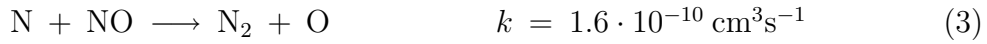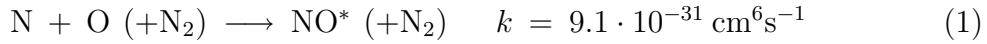
The excited NO^* species are created in reaction (1). However, the reaction (3), converting atoms N and molecule NO to N_2 and O, is very fast. Because the concentration of N is higher than that of NO (which depends on the amount of impurity oxygen in the carrier gas) the NO_β system can be observed in the spectra. Its increase with the z co-ordinate can be explained likely just by the increase of the leaking oxygen towards the nozzle exit.

5.2.6   OES of Ar/O_2 and -oxygen based discharges

A typical emission spectrum of Ar/O_2 discharge (Ar/O_2 with mixture ratio 590/10 in sccm, $p = 4\,\text{kPa}$, $P = 100\,\text{W}$, $z = \text{-8}\,\text{mm}$) is shown in Fig. 5.20. Under these experimental conditions the discharge is produced in fog-like form like in the mixture Ar/N_2. The spectrum consists mainly of NO_γ system (A $^2\Sigma^+ \longrightarrow$ X $^2\Pi$), OH system (A $^2\Sigma^+ \longrightarrow$ X $^2\Pi$), N_2 positive systems (B $^3\Pi_\text{g} \longrightarrow$ A $^3\Sigma_\text{u}^+$, C $^3\Pi_\text{u} \longrightarrow$ B $^3\Pi_\text{g}$) and Ar and O atomic lines. The presence of impurities was caused by use of technical argon and also by the leakages in the vacuum vessel. Moreover, the spectral system was optimized for measurement in UV region.

When present, OH and N_2 emissions were used in order to determine the plasma temperature. The vibrational temperature T_v was calculated from the band intensities of the nitrogen second positive system (C $^3\Pi_\text{u} \longrightarrow$ B $^3\Pi_\text{g}$) and the rotational temperature T_r was calculated from 0-0 band of OH system (A $^2\Sigma^+ \longrightarrow$ X $^2\Pi$). The development of rotational temperature along and below the tube in Ar/O_2 discharge is shown in Fig. 5.21. The temperature is, as expected, higher in the tube and lower below it, but under certain conditions a small temperature increase at the plasma column end is observed, too. Such an increase, visible also in case of vibrational temperatures (not shown here), can also influence the efficiency of technological processes.
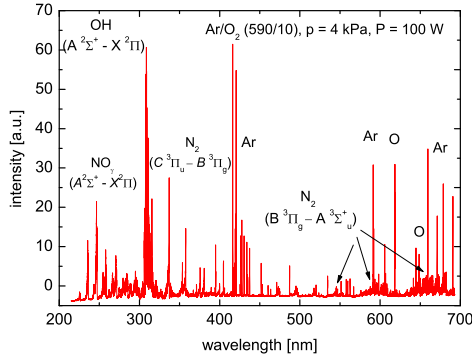
Fig. 5.20: The typical emission spectrum of Ar/O_2 discharge.
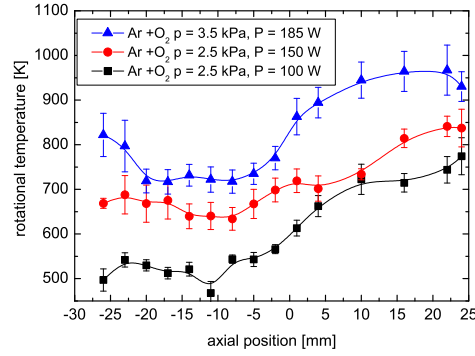
Fig. 5.21: Axial dependences of $T_r(z)$.

The emission spectra of N_2/O_2 discharges with different oxygen amount are displayed in Fig. 5.22 a for mixture 590/10 (sccm) and Fig. 5.22 b for air-like discharge 470/130 (sccm). In case of low oxygen amount, (Fig. 5.22 a), the spectrum consists particularly of NO_β system ($B\,^2\Pi \longrightarrow X\,^2\Pi$), NO_γ system and the N_2 positive systems. Excited NO molecules are probably created in the same reaction like in the Ar/N_2 discharge [146]

$$N \; + \; O \; (+N_2) \; \longrightarrow \; NO^* \; (+N_2) \,. \tag{1}$$
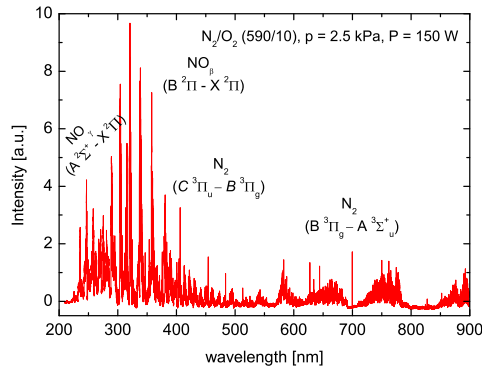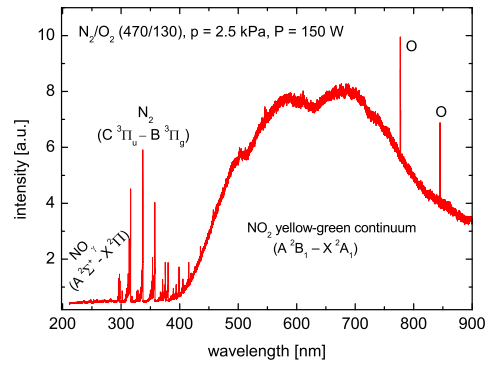
a) N_2/O_2 (590/10)

b) N_2/O_2 (470/130)

Fig. 5.22: Comparison of overview spectra N_2/O_2 discharges generated at the same experimental conditions $p = 2.5\,\mathrm{kPa}$, $P = 150\,\mathrm{W}$, $z = -3\,\mathrm{mm}$ with different mixture ratio: **a)** N_2/O_2 590/10 in sccm, **b)** air-like mixture N_2/O_2 470/130 in sccm.

When the oxygen amount is higher, following reaction also can take place

$$NO + O \longrightarrow NO_2^*. \tag{2}$$

Therefore in N_2/O_2 air-like mixtures highly intensive yellow-green continuum of NO_2 ($A^2B^1 \longrightarrow X^2A_1$) is observed, whereas NO systems, if present, are very weak. Besides, the N_2 second positive system and O atomic lines are registered, too.

a) N_2/O_2 (590/10)   **b)** N_2/O_2 (470/130)
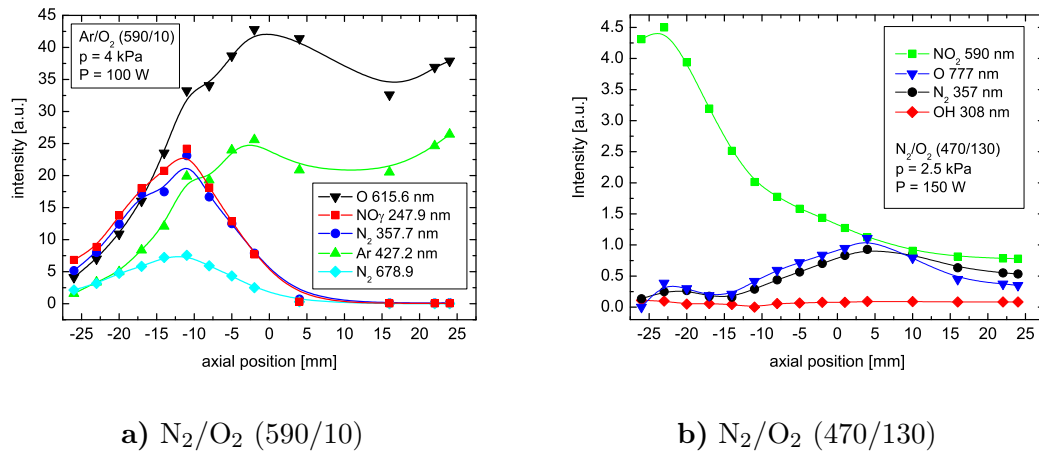
Fig. 5.23: Comparison of axial intensity development of spectral lines for N_2/O_2 discharges generated at the same experimental conditions $p = 2.5$ kPa, $P = 150$ W, $z = -3$ mm with different mixture ratio: **a)** N_2/O_2 590/10 (sccm), **b)** air-like mixture N_2/O_2 470/130 (sccm).

For effective sterilisation by UV radiation under this reduced-pressure conditions, discharge in nitrogen with a small amount of oxygen seems to be the most suitable as the energy is substantially put into NO_β emission. In air-like mixtures the energy is consumed in - for bacteria harmless NO_2 - radiation. In Fig. 5.23 a, b intensities of various lines and bands are plotted against the axial position in order to illustrate the spectrum development along and below the tube. Since argon and atomic oxygen have large excitation energies (14.5 and 12.8 eV respectively), they need to be excited electronically. However, the surface wave sustains the plasma only in the tube and therefore the intensity of depicted line decreases downstream of the tube end, see Fig. 5.23 a. As the molecules have lower excitation energy, they are excited in chemical processes, too. Therefore their emissions can even increase downstream of the tube (see again Fig. 5.23 a). Increase of NO_2 emission outside the tube was also observed, Fig. 5.23 b.

5.3   Bio-technological applications of surfatron discharge

The unique properties, which low-temperature plasma offers, are frequently used for industrial plasma processing. Surfatron plasma source was employed in three different kinds of bio-technological experiments. Surface activation of low density polyethylene for the purpose of increasing free surface energy is presented in this chapter at first. Bactericidal effects of Ar/O_2 and Ar/N_2 discharges under open atmosphere were tested on the bactericidal cultures *Neisseria sicca*, *Deinococcus radiodurans*, *Enterococcus feacium* and *Stenotrophomonas maltophilia*. These both discharges were also used for stimulation of germination of Lambs Quarter (*Chenopodium album* agg.) seeds.

5.3.1   Surface activation of low density polyethylene

Surfaces of low density polyethylene (LDPE) samples were activated using Ar/O_2 and Ar/N_2 (590/10 in sccm) discharges with the aim to increase the total surface energy and hydrophilicity of this material. The experiments were done at reduced pressure $p = 4\,kPa$ with input power $P = 100\,W$. Under these conditions the plasma exiting the tube was spread over the sample surface almost homogeneously in a fog-like form. Discharges are depicted in Fig. 5.2 b, c and their overview spectra in Fig. 5.20 (Ar/O_2) and Fig. 5.17 (Ar/N_2).
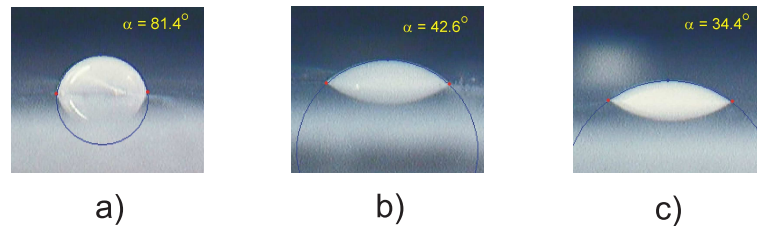

Fig. 5.24: Images of liquid drops (H_2O) on sample surface (LDPE) registered by SeeSystem. **a)** non-treated samples, **b)** plasma treatment, Ar/N_2, $t = 3\,s$, **c)** plasma treatment, Ar/O_2, $t = 22\,s$

The total surface energy was estimated by means of the sessile drop technique using the SeeSystem equipped by a CCD camera [147]. Images of liquid drops

on sample surface were registered by the camera and contact angles were subsequently measured from the solid-liquid meniscus, see Fig. 5.24. The total surface free energy γ^{TOT} of the samples was calculated using regression methods according to Lifshitz - van der Waals / acid-base theory from the contact angles of at least three different polar and apolar liquids; water (W), glycerol (G), diodomethane (D), ethylene glycol (E) and α-bromnapthalene (B) were used in our case [147]. The total surface energy γ^{TOT} is a sum of its apolar γ^{LW} and polar γ^{AB} components, $\gamma^{\mathrm{TOT}} = \gamma^{\mathrm{LW}} + \gamma^{\mathrm{AB}}$, where LW indicates the dispersive, i.e. apolar, Lifshitz - van der Waals interaction and AB refers to acid-base or electron - acceptor / electron - donor interactions.

The dependences of total surface energy γ^{TOT} calculated from different liquids combinations (W-D-F, W-D-G, W-E-B) on the treatment time are depicted in Fig. 5.25. The γ^{TOT} reaches energies about $51\,\mathrm{mJ.m^{-2}}$ for the W-D-G and W-E-B liquid combinations. The energy calculated from W-D-F is by about a few percent higher. This difference is probably caused by the choice of liquid combination; this problem is in detail discussed by *Navratil et al.* [148].
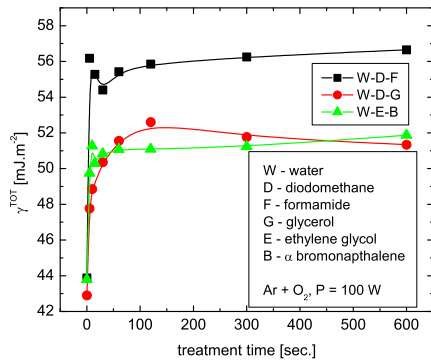
Fig. 5.25: Time dependence of γ^{TOT} estimated from different liquid combinations.
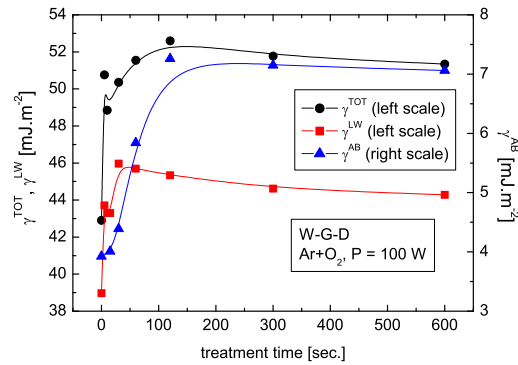
Fig. 5.26: Dependences of γ^{TOT} as well as both apolar γ^{LW} and polar γ^{AB} components on time.

The evolution of γ^{TOT} as well as its apolar γ^{LW} and polar components γ^{AB} with the $\mathrm{Ar/O_2}$ discharge treatment time is shown in Fig. 5.26. The depicted results were computed from the W-G-D liquid combination. The total surface energy γ^{TOT} was about $40\,\mathrm{mJ.m^{-2}}$ at the beginning of the process, i.e. before

plasma treatment. Surface treatment led to steep increase of total surface energy to a maximum located at about $52\,\mathrm{mJ.m^{-2}}$ during first $100\,\mathrm{s}$. After this time the γ^{TOT} was almost constant. The apolar component γ^{LW}, with maximum value about $45\,\mathrm{mJ.m^{-2}}$, is a major component of total surface energy γ^{TOT}. It can be seen in Fig. 5.26 that both γ^{TOT} and γ^{LW} have similar time evolution. Polar component reaches energy in order of units $\mathrm{mJ.m^{-2}}$. The bigger scatter of both energies γ^{TOT} and γ^{AB} during the interval $10\text{-}25\,\mathrm{s}$ is most probably caused by instability of the surfatron discharge just after ignition. The discharge cannot be sufficiently stabilized at the beginning of the experiment, and that limits the time resolution of measurements during the initial time period after discharge ignition. The points acquired in shorter treatment times are therefore overlapped by bigger experimental error than those acquired at longer times.
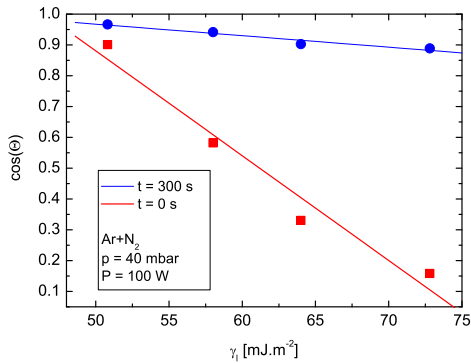
Fig. 5.27: The Zisman plot for four different liquids: W , G , F (formamide), M (methylene iodide). The critical surface energy $\gamma^{\mathrm{C}} = 48.75\,\mathrm{mJ.m^{-2}}$.
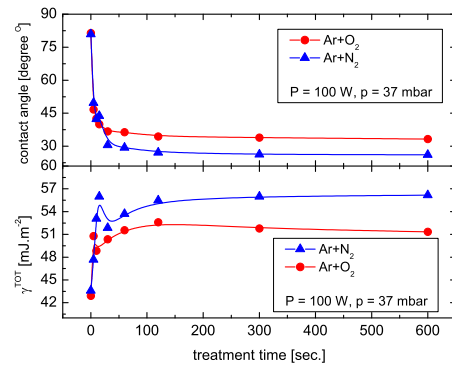
Fig. 5.28: Comparison of the dependences of the contact angle Θ (top panel) and of γ^{TOT} (bottom panel) on treatment time.

The critical surface free energy γ^{C} can be estimated from the so-called Zisman plot. The term "critical" is used because any liquid whose surface tension is greater than the "critical surface tension" makes a finite contact angle with the substrate. Critical surface tension values are useful empirical values that characterize relative degrees of surface energy of polymer substrates. Zisman noticed that a plot of cosine Θ (with Θ being the contact angle between the drop edge and the surface) versus the surface tension of different liquids γ_{l} is

often linear. Hence, the Zisman plot method is based on the determination of the dependence of the $\cos\Theta$ on γ_l. With linear extrapolation $\cos\Theta \to 1$ we obtain the critical surface energy γ^C. There were used four liquids, water (W), glycerol (G), formamide (F), methylene iodide (M), for building the Zisman plot in Fig. 5.27. The value of critical surface free energy for low density polyethylene obtained from linear extrapolation was estimated as $\gamma^C = 48.75\,\text{mJ.m}^{-2}$. From the previous considerations we conclude that after plasma treatment when $\gamma^{\text{TOT}} > \gamma^C$, the sample is well wettable.

Correspondence of surface hydrophilicity to total surface energy after plasma treatment by means of two different gas admixtures O_2 and N_2, is assessed in Fig. 5.28. The contact angle was measured for distilled water drop with volume $8\,\mu$l. Contact angle of non-treated LDPE sample was about $\alpha \approx 85°$ and quickly fell down to less than $\alpha \approx 30°$ during the first $50\,\text{s}$ of the treatment, see Fig. 5.24. The Ar/N$_2$ discharge mixture has been found to be more effective than Ar/O$_2$; it yielded higher total surface energy and, consequently, smaller contact angle within the same treatment time. Irregularities were not observed in decreasing contact angle curves, see Fig. 5.28. The small total energy descent followed by re-rise during first $50\,\text{s}$ in both types of discharges was probably due to the discharge instability in the initial time period after ignition, as described above.

5.3.2   Plasma sterilisation

Bactericidal effects of the plasma generated by the described surfatron-based experimental system were investigated, too. The suspension of sterile water and the defined bacteria culture was inoculated on the cultivating medium (agar) in appropriate concentration. The gram-negative *Neisseria sicca*, *Deinococcus radiodurans* and the gram-positive *Enterococcus feacium*, *Stenotrophomonas maltophilia* were used as model bacterial cultures. The concentration of bacteria on the cultivating medium was approximately $600\,\text{cm}^{-2}$ to get the continuous overlay of bacterial coat on the sample.

The samples were placed on the table distanced $z = 3\,\text{cm}$ from the nozzle outlet and exposed to plasma burning in open air. At such high pressure,

i.e. 1 atm., the highest power $P = 300\,\mathrm{W}$ had to be delivered. The mixtures of $\mathrm{Ar/O_2}$ and $\mathrm{Ar/N_2}$ (590/10 in sccm) were used. Under this experimental conditions plasma was burning only in the tube near by surfatron. Nevertheless, very weak plasma stream exiting the tube was visible in the darkness. Plasma stream temperature, measured simply by thermistor, was estimated roughly about $40\,^{\circ}\mathrm{C}$. Such low temperature together with open air conditions enabled presumption that bactericidal effect is not caused by high temperature and vacuum, respectively. The exposition time t varied from 30 seconds up to 8 minutes. After plasma exposition the samples were cultivated for the appropriate time and the bactericidal effect of particular experimental conditions was evaluated from the area of the zone of inhibition X_t in dependence on the treatment time t. Detailed description of the methodology is given in [149]. The sterilisation procedure is illustrated in Fig. 5.29.
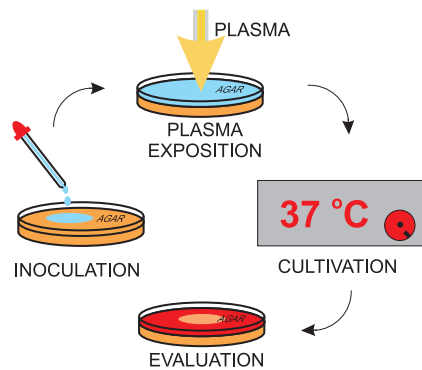
Fig. 5.29: Sterilisation procedure consists of four basic steps: inoculation, plasma exposition, cultivation, evaluation.
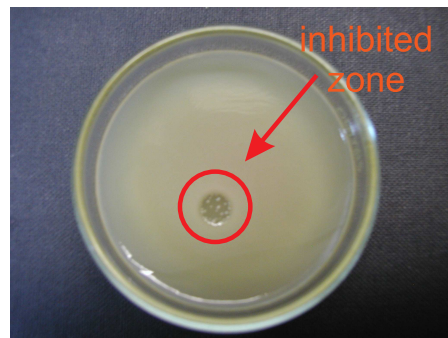
Fig. 5.30: The zone of inhibition is separated from the continuous coat by comparatively sharp boundaries.

The photography of one inhibition zone on continual bactericidal coat is in Fig. 5.30. Results for the evaluated X_t in dependence on time of exposition t are shown in the table Tab. 5.1. It is evident from the table that the efficiency of bactericidal effect is not the same for all used gas-mixtures and all the bacteria cultures. The bactericidal effect of $\mathrm{Ar/O_2}$ gas-mixture became visible already after $t = 1\,\mathrm{min}$ especially for gram-negative bacteria. For gram-positive bacteria *Deinococcus radiodurans* the bactericidal effect became visible after $t = 2\,\mathrm{min}$. The *Enterococcus feacium* was resistant and the

Bacteria	Gas mixture Ar/O_2 (590/10)				
	$X_{0.5}$ [mm^2]	X_1 [mm^2]	X_2 [mm^2]	X_4 [mm^2]	X_8 [mm^2]
Neisseria Sicca	0	34	67	110	165
Deinococcus radiodurans	0	0	69	109	123
Enterococcus faecium	0	0	0	0	0
Stenotrophomonas maltophilia	0	30	64	113	176
Bacteria	Gas mixture Ar/N_2 (590/10)				
	$X_{0.5}$ [mm^2]	X_1 [mm^2]	X_2 [mm^2]	X_4 [mm^2]	X_8 [mm^2]
Neisseria Sicca	0	0	0	30	77
Deinococcus radiodurans	0	0	0	50	98
Enterococcus faecium	0	0	0	0	0
Stenotrophomonas maltophilia	0	0	0	15	58

Tab. 5.1: The areas of the inhibition zones (X_t) of bacteria exposed to the discharge for $t = 0.5$, 1, 2, 4 and 8 minutes in Ar/O_2 and Ar/N_2 (590/10 in sccm); discharge generated at atmospheric pressure.

bactericidal effect was not detectable even after $t = 8$ min of exposure. For Ar/N_2 the bactericidal effect became visible after $t = 4$ min for both gram-negative and gram-positive bacteria *Deionococcus radiodurans*. The gram-positive bacteria *Enterococcus feacium* was resistant like in the previous case.

5.3.3   Plasma stimulation of seed germination

The Lamb's Quarters (*Chenopodium album* agg.) seed was stimulated by plasma discharge with the aim to increase germination. The experimental conditions were set in such a way that the fog-like form of discharge was created - $p = 4$ kPa, $P = 100$ W, Ar/O_2 or Ar/N_2 (590/10 in sccm). The seed, placed on petri dish distanced $z = 3$ cm from the nozzle outlet, was treated for relatively long time, up to $t = 50$ min. Afterwards the germination was tested by standard ways and statistical methods under laboratory conditions. The results are summarized in Fig. 5.31. Only the percentages of total amount of successfully germinated seeds after 8 days are depicted in the graph.

The seed was stimulated and the germination increased roughly three-times, from 15 % up to 50 %, after treatment in the Ar/O_2 surfatron discharge.
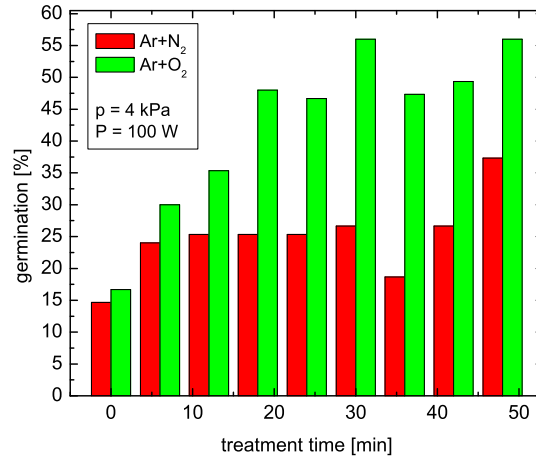
Fig. 5.31: Dependence of seed germination on plasma treatment time for the Lamb's Quarters seeds. The fluctuations of germination percentage for plasma treatment times longer than 20 min are probably due to statistical error.

In the interval 0 - 20 minutes the germination increased almost linearly. For longer treatment times the germination remained more or less constant; slight fluctuations are probably due to statistical error. In our opinion, the plasma stimulation of seeds might be caused by two major effects: **(i)** by erosion processes of seed protective coat and **(ii)** by germicidal effect of Ar/O_2 discharge. Indeed, the oxygen plasma can erode the protective seed-coat and growth of seeds is easier. This presumption is supported by the experimentally observed dynamics of germination: the plasma-treated seeds started to grow as early as after (approximately) 5 hours while non-treated seeds as far as after several (2 - 3) days. Bactericidal effects of oxygen mixture plasma were confirmed earlier (see previous chapter 5.3.2). In this way the surfatron - generated discharge could remove bacteria off the seed protective coat. This effect was also supported by the experimental observation: the treated seeds (unlike sometimes the untreated ones) did not become mouldy during germination under laboratory condition. Ar/O_2 discharge seems to be more efficient than Ar/N_2 discharge as it supports both the above mentioned stimulation mechanisms.

6. EXPERIMENTAL RESULTS AND DISCUSSION OF DC PLANAR MAGNETRON PLASMA DIAGNOSTICS

Dc planar magnetrons are quite often applied in surface technology at present time. Hence, plasma generated by dc planar magnetron system, described in first part of the chapter, which is used for deposition of thin films was investigated. Below there are mainly presented results of single probe measurements in magnetron discharge generated in continuous (cw) and pulsed regime. Moreover, measurements with an energy resolved mass spectrometer were also done to support interpretation of some physical effects. The investigated magnetron was operated in balanced (BLM) as well as in unbalanced (UNB) mode with the arrangement for deposition of TiO_x and TiN_x layers. Therefore, Ti target and Ar, Ar/O_2 and Ar/N_2 gas mixtures were used for experiments. This part of work has been done in the University of Geifswald (Germany), where the author of the thesis spent on leave 15 months.

6.1   Experimental setup for layer deposition

Dc planar magnetron sputtering system, investigated in the frame of doctoral study, consisted of a commercial planar magnetron of the type VTech 75 by Gencoa. Simple disk-geometry of the cathode was used. The target made from Ti (Ti 99.9 % purity grade, diameter 77 mm, thickness 8 mm) was directly connected with the cathode. Water cooling protected the cathode from overheating and consequent destruction. The magnetron could be operated either in BLM or UNB mode by mechanically changing permanent magnet configuration [150], see Fig. 3.5. This could be done while the discharge was on. The cathode structure was shown in Fig. 3.3. The magnetron was fed by
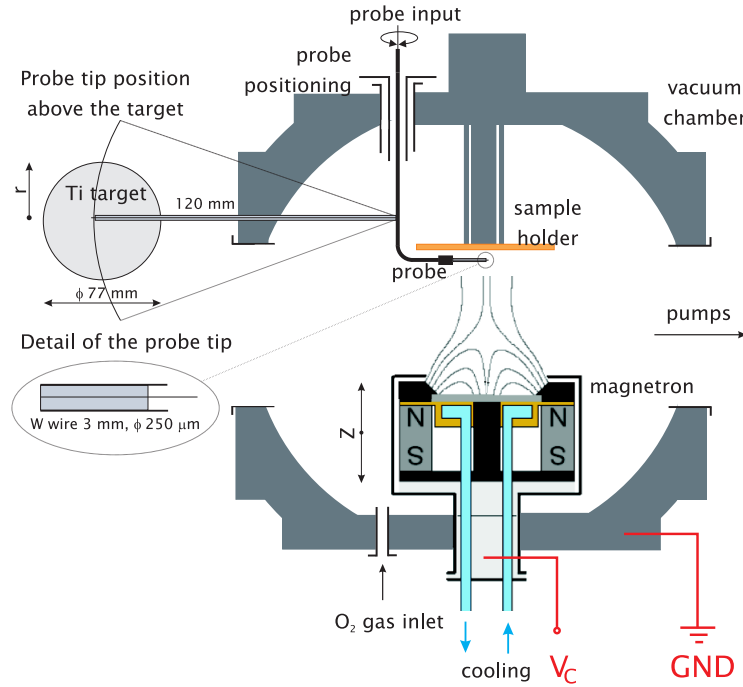
Fig. 6.1: Experimental DC planar magnetron setup.

commercial dc power supply AE MDX 500 with the voltage range down to -620 V designated for continuous regime.

The magnetron was inserted into lower part of the ultra-high vacuum (UHV) chamber, electrically isolated from the walls; see Fig. 6.1. This UHV vacuum chamber, spherically-shaped with diameter about 70 cm, was made from stainless-steel. The whole magnetron cathode was movable in vertical direction, which allowed changing the distance between the target and the substrate. The vacuum chamber was pumped out by turbomolecular pump Pfeiffer TMH 1600, backed by rotary vacuum pump, down to ultimate pressure 10^{-8} Pa. Pressure was adjusted by a throttle gate valve VAT 64 installed between the chamber and the turbomolecular pump. The valve was controlled by VAT control unit PM-3. The flow rates of working gas or mixture of carrier and reactive gases were controlled by MKS mass flow controllers in the ranges up to 2, 20 and 100 sccm. Ar was used as carrier gas, O_2 and N_2 as reactive gases; each with high purity grade 5.9. Argon gas injection line was fitted to the magnetron cathode. This allowed directing of argon gas over the target surface. Reactive gas pipe was inserted into the chamber with its nozzle end situated not far from the target. The mass

flow controllers, the throttle valve and the magnetron were PC-controlled via their own control units.

The pulsed regime of magnetron was realized by a combination of the dc supply and handmade electronic power switch. In series with the discharge path there was inserted a ballast resistor ($R = 15\,\Omega$). As a source of dc discharge power during the active impulse served series of big capacitors, which were charged from the dc source during the idle part of the period. In such manner the discharge current during the pulse could reach much higher values compared to the current limit of the used dc source. The switch was activated by a signal from pulse generator Agilent 33120A. The leading edge of the pulse served as a trigger signal for time-resolved probe acquisition system which was described in chapter 5.1.1. The same diagnostics device was used for measurements in cw regime.

The probe, made of tungsten wire $250\,\mu$m in diameter and with active length $3\,$mm, was inserted into the chamber using radially movable feed-trough, electrically isolated from the vacuum chamber. The probe was situated near the plane of the substrate (distance roughly 65-$85\,$mm from the target) as well as near the target (minimum distance $15\,$mm from the target); see Fig. 6.1. Different radial distances were achieved by inclining the probe holder. The probe tip was perpendicularly oriented to the magnetic field lines. Such arrangement minimized the effect of magnetic field on the probe [125]. Further, the magnetic field B in the plane $z = 65\,$mm measured from the target was less than $1\,$mT. As a calculated mean Larmor radius r_{Le} for electrons was much larger than the radius of probe wire r_{p}, $r_{\text{Le}} \gg r_{\text{p}}$ [120], the influence of magnetic field upon measured data could be neglected. This criterion was also valid in the plane $z = 15\,$mm.

6.2   Probe investigation of Ar and Ar/N$_2$ discharge

The experiments were carried out in experimental configuration described in previous section 6.1 and the scheme is depicted in Fig. 6.1. Argon and a mixture Ar/N$_2$ were used as working gases. The flow rate of working gas

was constant - Ar (19 sccm) and reactive admixture N_2 (1 sccm). Discharge power P, determined as a product of instant cathode voltage and discharge current, was varied in the range $P = 10 \text{-} 120\,\text{W}$; the pressure p in the chamber was optional $p = 0.3 \text{-} 1.2\,\text{Pa}$. The power supply of the magnetron was stabilized to the discharge current.

The so-called double Maxwellian EEDF, with two hardly distinguishable groups of electrons, typical for Ar discharges at low pressures [91], was frequently met during I-V probe characteristic processing. At first the plasma potential V_{pl} was determined as the probe voltage corresponding to zero-cross of the second derivative of the I-V characteristic. Then the measured data of the second derivative of the probe characteristic were integrated in order to find the mean electron energy E_{m} using equation (4.14). The interval of integration was limited by a suitable value chosen by the user on the higher energy side and by V_{pl} on the lower energy one. The electron density n_{e} was estimated from i_{e}^2 vs. V_{p} plot in the electron accelerating regime (4.10). No noise reducing filters were used.

The ion current i_{i} versus energy measured by a plasma monitor represents an ion distribution function (IDF). This IDF is not the velocity distribution function nor the energy distribution function defined in kinetic theory [151], as the free space distribution function is modified by the interaction in presheath and sheath and by the acceleration to the extraction hood of the monitor. Therefore, the free space velocity distribution function can be calculated only in very special cases from plasma monitor measurements. The IDF in direction to the orifice of the plasma monitor was measured. With this distribution function the ions are hitting the substrate. The integral over the measured i_{i} is a measure for the ion flow density to the substrate. The total ion current to the substrate and the average ion energy can also be calculated [152]. For plasma monitoring the plasma process monitor PPM 421 (Balzers) was used. The orifice of diameter 0.1 mm was located at the substrate position. The extraction hood was biased with -20 V. The distribution functions of Ar^+, Ar^{++}, Ti^+, Ti^{++}, N^+, N^{++} and N_2^+ ions were measured.

Ar   Ar/N$_2$

Fig. 6.2: Dependences of n_e on power delivered to the discharge. The probe was situated near by the plane of substrate position, $z = 88$ mm from the target, at the target axis.

In following graphs the dependences of plasma parameters on the power are shown. All presented measurements are done at the axis of the discharge. Fig. 6.2 shows the n_e dependence on the power in Ar and Ar/N$_2$ discharge for different pressures and working modes. The left graph is for pure Ar and the right one for Ar/N$_2$ discharge. Generally, the n_e increases with power and is higher in UNB than in BLM mode. The n_e depends on the pressure - at lower pressures the n_e is lower, too. The differences between BLM and UNB mode are caused by ionisation processes created by different types of magnetic field. The electron density is higher in Ar/N$_2$ discharge ($n_e \approx 10^{16} \, \text{m}^{-3}$) than in Ar discharge ($n_e \approx 10^{15} \, \text{m}^{-3}$), which could be caused by enhanced ionization of nitrogen particles via Ar metastables. We observe weak decrease of n_e with the radial distance from the target axis, less than 10 % (not shown).

The mean electron energy E_m is higher in UNB than in BLM mode in both types of discharges, see Fig. 6.3. The difference between averaged energies for the same pressure is relatively small. The E_m are higher in Ar ($E_m \approx 1.8$ - 3.6 eV) than in Ar/N$_2$ discharge ($E_m \approx 1.6$ - 2.5 eV). The interesting shape of dependences with maxima around 70 W, especially obvious in Ar/N$_2$ discharge, is due to ionisation of Ti. The amount of Ti atoms increases exponentially with the discharge power, see Fig. 6.4. The lower ionization potential of Ti reduces the energy of electrons. The E_m is reciprocally proportional to
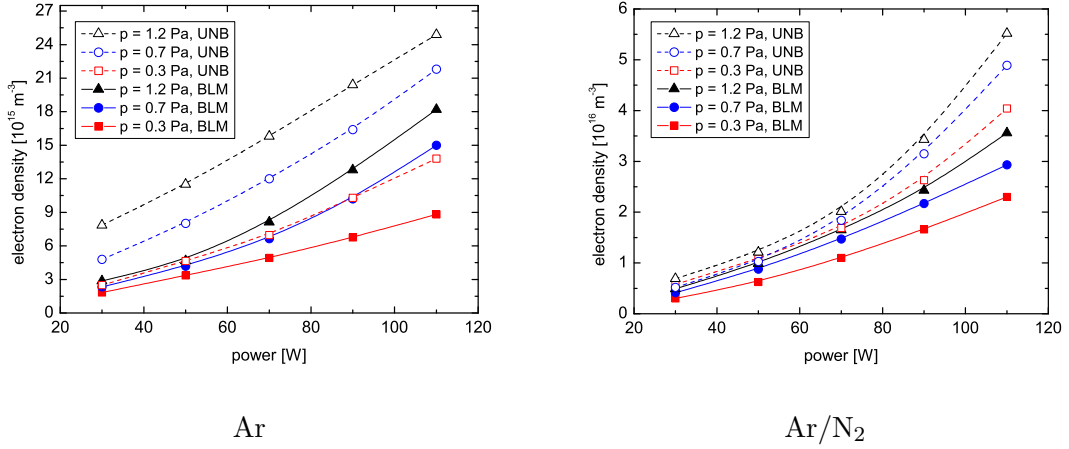
Ar   Ar/N$_2$
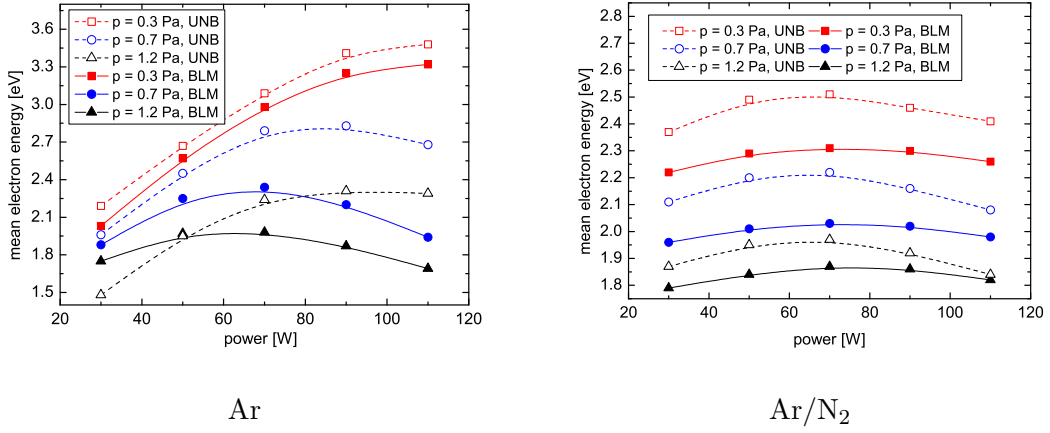
Fig. 6.3: Dependences of E_m on power delivered to the discharge. The probe was situated near by plane of substrate, $z = 88$ mm from the target, at the target axis.

the pressure. This is an indication of the influence of the mean free path, which shows similar behavior. Decrease of E_m with the radial distance is somewhat more pronounced in BLM than in UNB mode (about 15 %). The plasma potentials V_{pl} showed qualitatively a similar behavior as the E_m with slightly positive values $V_{pl} \approx 0.5 \text{-} 2.5$ V.

integrated area for Ar$^+$ integrated area for Ti$^+$
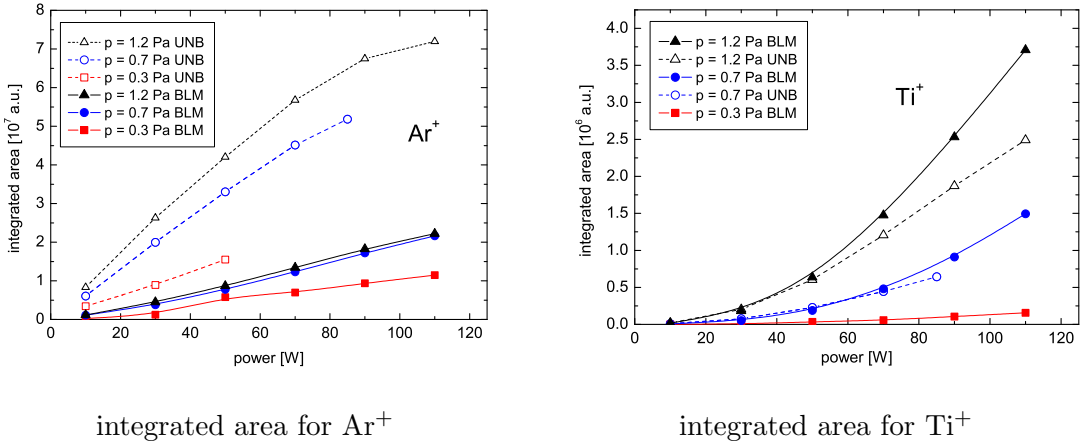
Fig. 6.4: Dependences of integrated areas for Ar$^+$ and Ti$^+$ on power delivered to the pure Ar discharge.

In case of pure Ar discharge the ion flow density to the substrate is estimated by Ar$^+$ ions followed by Ar^{++} ions, the contribution of which is by about one order of magnitude lower. At low powers the contribution of Ti$^+$ ions

is about 1%. At higher power and pressure this contribution reaches the level of Ar^{++} ions (about 10 %). Ions Ti^{++} contribute less than by 0.1%. Fig. 6.4 shows the areas for Ar^+ and Ti^+ ions vs. discharge power for pure Ar discharge.

As expected from the probe measurements, the Ar^+ ions flow density increases roughly proportional to the discharge power P. The flow increases with pressure p and is higher in UNB mode. The flow of Ti^+ ions increases approximately exponentially with P. The amount of sputtered Ti atoms is proportional to the discharge power, too. But, because of the lower ionization potential, atoms Ti will be preferentially ionized compared to Ar. This effect leads to the strong increase of Ti^+ ions. The ionization degree of Ti is much higher than the ionization degree of Ar. Moreover, this effect reduces the E_m, Fig. 6.3, and increases the n_e somewhat more than linearly. The maximum energy of the distribution function of Ar^+ depends on the plasma potential. It is remarkably lower in case of BLM mode compared to UNB one. This energy increases with the power and has got a lower slope for high powers. If N_2 is added to the buffer gas, the total flow densities of ions increase in agreement with the higher plasma density (Fig. 6.2). The amount of nitrogen ions depends on pressure, nitrogen flow rate and power. Generally, N_2^+ is the dominating nitrogen ion followed by N^+ and N^{++}. At low N_2 flows ($< 0.5\,\mathrm{sccm}$) there is a maximum of the N_2^+ ion flow for smaller powers. At 2 sccm of N_2 the N_2^+ ion flow increases almost proportionally to the discharge power. At high pressure it reaches the level of Ar^+ ions. It seems to be strongly influenced by the amount of Ti ions, see discussion above.

6.3   Diagnostic of Ar/O_2 discharge

Oxygen based plasmas are frequently used in technological processes, e.g. in deposition of oxide layers, plasma etching, plasma sterilisation etc. Efficiencies of these processes are usually caused by presence of negative oxygen ions, radicals etc. Thus, investigation of negative ions properties belongs to

the most interesting subjects in electronegative plasmas. However, the probe diagnostic of the electronegative plasma is more complicated compared to the electropositive one. Presence of negative ions in plasma changes the I-V characteristics and complicates the interpretation of Langmuir probe data.

Methods determining negative ion density in electronegative plasma from Langmuir probe measurements were proposed, e.g., in [153, 154, 155]. The approach in papers [154, 155] is based on comparison of two probe characteristics, the first taken in pure electropositive (Ar) plasma, the second measured in electronegative (Ar/O$_2$) plasma. Determination of negative ion density and explanation of their creation together with another plasma characteristics by means of Langmuir probe measurements are mainly discussed in this chapter. In spite of the fact that absolute values are burdened by larger computational error, the method gives us idea about negative ion properties.

6.3.1 Evaluation of probe data with respect to the presence of negative ions

We determined plasma parameters from Langmuir probe measurements by a method generalizing a procedure applied in [155]. In the following text the subscripts 'e', 'p' and 'n' denote quantities related to electrons, positive ions and negative ions, respectively. Quantities concerning electronegative plasma are labeled by dash. Let us start our considerations with remembering some relations for electropositive plasma. For the sake of simplicity we suppose the Maxwell electron energy distribution function.

Thus, the electron current component of the characteristics in the transition region is

$$i_e \;=\; eA_p n_e \cdot \sqrt{\frac{eT_e}{2\pi m_e}} \cdot \exp\left(\frac{V}{T_e}\right), \qquad V \;<\; 0. \tag{6.1}$$

where A_p is the probe area, V is voltage bias between the probe and plasma, n_e is electron number density and T_e is electron temperature measured in volts ($= kT_e/e$ with T_e measured in Kelvins).

Not a few theories have been proposed for description of the positive-ion

current and ion current theories do not provide sufficiently reliable and undoubted results. We assume here a general form

$$i_{\mathrm{p}} = e A_{\mathrm{p}} n_{\mathrm{p}} \cdot \sqrt{\frac{e T_{\mathrm{e}}}{m_{\mathrm{p}}}} \cdot F\left(V, T_{\mathrm{e}}, \lambda\right), \qquad V < 0. \tag{6.2}$$

with function F specified by a particular ion-current model. Parameters λ are optional and can be determined empirically by fitting the formula (6.2) to the measured data in the region $V \ll 0$. For instance, in collisional theories of ion current the λ parameters should be the Debye number $D_\lambda = r_{\mathrm{p}}/\lambda_{\mathrm{D}}$ and the Knudsen number $K_{\mathrm{i,e}} = \lambda_{\mathrm{i,e}}/r_{\mathrm{p}}$. Multiplicative factor $\sqrt{e T_{\mathrm{e}}/m_{\mathrm{p}}}$ denotes Bohm velocity v_{B} of positive ions at the sheath-presheath edge for the collisionless plasma sheath [5].

Let us now consider electronegative plasma. The presence of negative ions does not significantly influence the part of characteristics where electron current is dominant as the inequality $T_{\mathrm{e}}'/m_{\mathrm{e}} \gg T_{\mathrm{n}}'/m_{\mathrm{n}}'$ yields $I_{\mathrm{e}}' \gg I_{\mathrm{n}}'$. For instance, usual ratios $T_{\mathrm{e}}'/T_{\mathrm{n}}' \sim 10^2$, $m_{\mathrm{e}}/m_{\mathrm{n}}' \sim 10^{-3}$ and $n_{\mathrm{e}}'/n_{\mathrm{n}}' \sim 1$ give $I_{\mathrm{e}}'/I_{\mathrm{n}}' \sim 10^2$. Hence, the characteristics of electronegative plasma near the plasma potential can be treated as pure electronic and the plasma potential V_{pl}', electron number density n_{e}' and electron temperature T_{e}' can be determined by standard procedures.

On the contrary, more controversial is the assumption that the model (6.2) of positive-ion current holds for electronegative plasma with the same parameters λ. There is also some discussion concerning validity of the Bohm criterion. *Braithwaite* and *Allen* [156] obtained for low pressures the modified Bohm criterion

$$v_{\mathrm{B}}^2 = \frac{e T_{\mathrm{e}}'}{m_{\mathrm{p}}'} \cdot \frac{n_{\mathrm{ps}}' T_{\mathrm{n}}'}{n_{\mathrm{es}}' T_{\mathrm{n}}' + n_{\mathrm{ns}}' T_{\mathrm{e}}'}, \tag{6.3}$$

where the subscript 's' denotes local values at the sheath edge. At low collisionality the negative ions are confined in the plasma bulk, thus $n_{\mathrm{ns}}' \approx 0$ and the normal Bohm criterion applies. We suppose here - with some uncertainty - that the model (6.2) remains valid for electronegative plasma, too.

A general method determining parameters of electronegative plasma from Langmuir probe measurements can be shortly described as follows. First, a comparative characteristic of electropositive plasma existing in similar conditions is measured and from its electron part the electron number density n_e and the electron temperature T_e are determined. Then from its ion part and with the equality $n_p = n_e$ taken into account the optional parameters λ of the ion current model (6.2) are specified. Knowing these parameters, the characteristics of electronegative plasma can be processed. The electron part of the characteristics measured in electronegative plasma gives the electron number density n'_e and electron temperature T'_e. The model (6.2) applied to the positive-ion saturation current gives the positive-ion density n'_p. Finally, the negative-ion density n'_n is determined from the quasineutrality condition, $n'_n = n'_p - n'_e$.

In our measurements the common procedure outlined above was specified as follows. For the electrons we supposed Maxwellian (6.1) or double-Maxwellian distribution. In both measurements in electropositive and electronegative plasmas the plasma potential was determined from the first or second derivative of the characteristics and the electron density and temperature were determined by fitting the single-Maxwell (6.1) or double-Maxwell formula to the measured data.

For the positive-ions we applied empirical ion current model (6.1) with

$$F(V) = C \left(1 - \frac{V}{T_e} \right)^{\kappa} \tag{6.4}$$

or

$$i_p = D \left(1 - \frac{V}{T_e} \right)^{\kappa}, \qquad D \equiv e A_p n_p \sqrt{\frac{e T_e}{m_p}} C \tag{6.5}$$

Parameters $\lambda = (C, \kappa)$ can be determined from the region $V \ll 0$ of characteristics measured in electropositive plasma. For dc discharge in Ar plasma under experimental conditions which were investigated we obtained $\kappa \approx 1.4$, $C \approx 0.2$.

To express the ion densities n'_{p}, n'_{n} and the degree of electronegativity $\alpha \equiv n'_{\mathrm{n}}/n'_{\mathrm{p}}$ in electronegative plasma without unnecessary multiplicative factors, we employ symbols

$$\varepsilon \;\equiv\; \frac{n'_{\mathrm{e}}}{n_{\mathrm{e}}} \qquad \gamma \;\equiv\; \frac{n'_{\mathrm{p}}}{n_{\mathrm{p}}} \tag{6.6}$$

Then

$$n'_{\mathrm{p}} \;=\; \gamma n_{\mathrm{e}}, \quad n'_{\mathrm{n}} \;=\; (\gamma - \varepsilon)\, n_{\mathrm{e}}, \quad \alpha \;=\; 1 - \frac{\varepsilon}{\gamma} \tag{6.7}$$

In our method ε is evaluated directly as the electron densities n'_{e} and n_{e} are explicitly determined. The parameter γ is

$$\gamma \;=\; \sqrt{\frac{T_{\mathrm{e}}}{T'_{\mathrm{e}}} \cdot \frac{m'_{\mathrm{p}}}{m_{\mathrm{p}}} \cdot \frac{D'}{D}} \tag{6.8}$$

with parameters D' and D determined by fit of the model current (6.5) to the ion parts of the characteristics measured in electronegative and electropositive plasma, respectively.

For comparison, the less general method described in [155] is also included in the scheme (6.6 and 6.7), now with parameters

$$\varepsilon \;=\; \sqrt{\frac{T_{\mathrm{e}}}{T'_{\mathrm{e}}} \cdot \frac{i'_{\mathrm{e}}(0)}{i_{\mathrm{e}}(0)}} \qquad \gamma \;=\; \sqrt{\frac{T_{\mathrm{e}}}{T'_{\mathrm{e}}} \cdot \frac{m'_{\mathrm{p}}}{m_{\mathrm{p}}} \cdot \frac{i'_{\mathrm{p}}}{i_{\mathrm{p}}}} \tag{6.9}$$

The first expression follows from the Maxwellian electron characteristic (6.1), the second one is a consequence of the simplest but not quite adequate model of constant positive-ion saturation current ($i_{\mathrm{p}} = D$).

There are two error sources in determining the ion densities. The first one is connected with the assumption that parameters λ in (6.2) (or C, κ in (6.4)) are identical in both electropositive and electronegative plasmas. To minimize this error, the state of the reference electropositive plasma should be as close to the state of electronegative plasma as possible.

The second error arises due to the positive-ion mass uncertainty. The effective mass m_p of a mixture of positive ions is defined by the formula

$$\frac{1}{\sqrt{m_\mathrm{p}}} = \sum_X p(X) \frac{\nu(X)}{\sqrt{m(X)}} \tag{6.10}$$

where $p(X)$ is fraction of a positive-ion species X ($\sum p(X) = 1$), $\nu(X)$ is its ionization degree ($\nu = 1,\ 2,\ ...$) and $m(X)$ is its mass. The kind of positive ions and their density in Ar/O_2 plasmas were roughly estimated by plasma monitor measurements. The obtained orders of magnitudes of relative ion concentrations are shown in the table. Similar values for Ar^+ and Ar^{++} were detected in pure Ar plasma.

$\mathbf{X}$	$n(\mathbf{X})$ [a.u]
Ar^+	$10^0 - 10^1$
Ar^{++}	10^0
O_2^+	10^{-1}
O^+	10^{-2}
O^{++}	$10^{-5} - 10^{-4}$

Neglecting fractions of positive oxygen ions, one obtains from Eq. (6.10)

$$m_\mathrm{p} = \frac{m(Ar)}{[1 + p(Ar^{++})]^2}. \tag{6.11}$$

On account of plasma monitor analysis we estimated $p(Ar^{++})$ in the range (0.1, 0.3) for all measurements regardless of whether the investigated plasma was electropositive or electronegative one. Hence, $m_\mathrm{p} = (0.7 \pm 0.1)\, m(Ar)$, $\sqrt{m'_\mathrm{p}/m_\mathrm{p}} = 1 \pm 0.2$. The error of the parameter γ in (6.8) is due to the positive-ion mass uncertainty estimated up to 30 %.

6.3.2 Experimental results and discussion

The slightly electronegative Ar/O_2 magnetron discharge was investigated with the main goal to diagnose the density of negative ions n_n together with

other plasma parameters as electron density n_e, electron temperature T_e and plasma potential V_pl. The n_n was calculated by the procedure described in the previous section. In the following graphs we introduce experimentally determined plasma parameters depending on incoming power $P = 30\text{-}110\,\mathrm{W}$, on axial distances from the cathode ($z = 45, 65, 85\,\mathrm{mm}$) and on radial distance r from the axis of the target (cathode). The given radial span corresponds roughly to the target diameter, $r = 0\text{-}50\,\mathrm{mm}$. The pressure $p = 0.7\,\mathrm{Pa}$ in the vacuum chamber was kept constant. The discharge was created from Ar as a carrier gas with flow rate 19.5 sccm. For Ar/O_2 mixtures O_2 was added as a reactive gas with two typical flow rates 0.75 and 1.5 sccm. Measurements were carried out in both BLM and UNB modes.

The sputtering process is influenced by mutually dependent cathode voltage and discharge current. To simplify the analysis we used their product as an optional parameter specifying the plasma discharge. Further argument for choosing power as an experimental parameter lies in the fact that it characterize a lot of former measurements; therefore it is possible to compare these former results with processed data. However, power does not always adequately characterizes the process; some of the investigated plasma parameters like V_pl are better characterize by discharge voltage. The target oxidation is necessarily accompanied by increase of cathode voltage and that has to be taken into account as an another error source. This target oxidation is important mainly in mixtures highly subsidized by oxygen.

Power dependences of n_e for two different Ar/O_2 ratios are presented in Fig. 6.5 a. The figure Fig. 6.5 b depicts power dependences of n_n. As plasma monitor data showed, relative concentration of atomic oxygen ions O^- is by two orders of magnitude higher than concentration of molecular oxygen ions O_2^-. Hence, negative ion density concerns atomic oxygen ions O^-.

The n_n is lower than the n_e roughly by one order of magnitude, $n_\mathrm{e} \approx 10^{15}\,\mathrm{m^{-3}}$, $n_\mathrm{n} \approx 10^{14}\,\mathrm{m^{-3}}$. The n_n is higher in UNB than in BLM mode by several hundreds percent. Fig. 6.5 b shows that dependences of n_n on O_2 concentration or magnetron mode have opposite behavior compared to analogous dependences of n_e: if n_e is lower, then n_n is higher and vice versa. Electrons

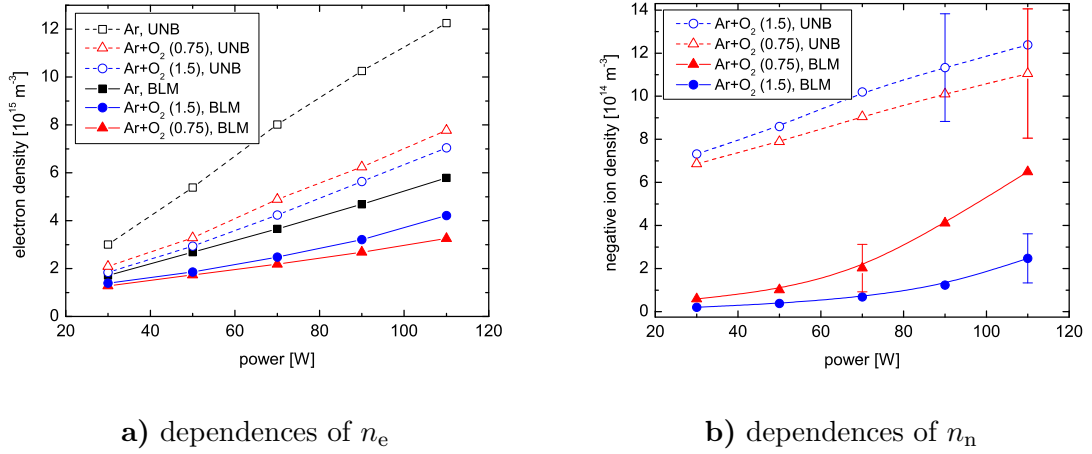**a)** dependences of n_e **b)** dependences of n_n

Fig. 6.5: Dependences of n_e **(a)** and n_n **(b)** on power, $p = 0.7$ Pa, $z = 65$ mm, $r = 0$ mm, Ar (19.6 sccm), O_2 (0.75 and 1.5 sccm).

escaping from the magnetic trap are caught by oxygen particles, n_e decreases and new negative ions originate, n_n increases. More detailed analysis of this phenomenon has to be done.

a) power dependences of T_e **b)** radial dependences of T_e
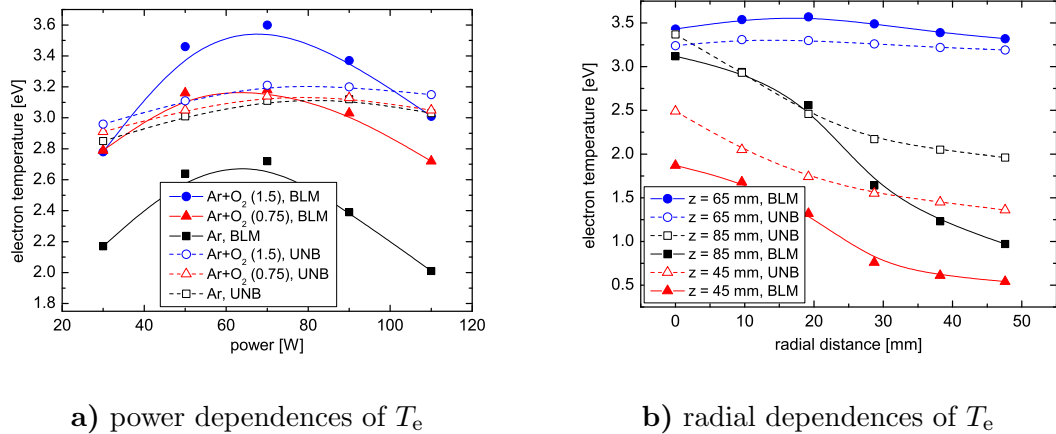
Fig. 6.6: **(a)** Power ($r = 0$ mm, $z = 65$ mm) and **(b)** radial ($z = 45, 65, 85$ mm, $P = 70$ W) dependences of T_e, $p = 0.7$ Pa, Ar (19.6 sccm), O_2 (0.75 and 1.5 sccm).

The difference between electron temperatures T_e at particular dc power in two different Ar/O_2 mixtures is much larger in the BLM mode compared to the UNB one, see Fig. 6.6 a. Presence of oxygen in the discharge increases T_e. The energy equal to electron affinity of particular specie (for atomic oxygen 1.48 eV) is released at the time of negative ion creation process. Electron

affinity of O_2 is comparatively small - 0.45 eV. Such energy is not sufficient to dissociate the O_2 molecule when an electron is attached since its dissociation energy amounts to 5.1 eV. It is therefore supposed that O_2 is first dissociated by electron impact and then the negative atomic oxygen ion is created by electron attachment. O_2 dissociation process has resonance electron energy around 6.5 eV [157]. Most of the electrons with such energy spend therefore their energy on the dissociative electron attachment of O_2. At the same time the low energy electrons can efficiently transfer their energy to O_2 vibrations, i.e. they heat the oxygen gas. Both mentioned processes deplete the electron energy.

Comparison of radial dependence of T_e in BLM and UNB is shown in Fig. 6.6 b. In BLM mode we can see steep decrease of the temperature at the edge of the discharge, while in UNB mode these dependences are more moderate. This is probably caused by the different shape of magnetic field. In the BLM mode the lower energy electrons cannot escape from the "magnetic trap" at the magnetron cathode. The high energy electrons escape but lose their energy stepwise in collisional processes. Possible reason for the local increase of the T_e at $z = 65$ mm can be as follows.

Magnetic field prevents electrons from escaping from the cathode vicinity, therefore the n_e is the highest near the cathode, see Fig. 6.7 a. In spite of this, some amount of electrons around the axis of the target have enough energy (Fig. 6.6 b) for escaping from the cathode space while being accelerated by electric field. That electron flux can dissociatively attach to electronegative O_2 molecules when the electron energy reaches the resonant value for this process, i.e. the energy around 6.5 eV. This process takes apparently place at the height around $z = 65$ mm, where negative ion density is the highest, see Fig. 6.7 b. The electrons that do not participate in the dissociative attachment flow further from the cathode and induce other ionisation processes. This explains further increase of n_e and decrease of T_e in the $z = 85$ mm compared to $z = 65$ mm.
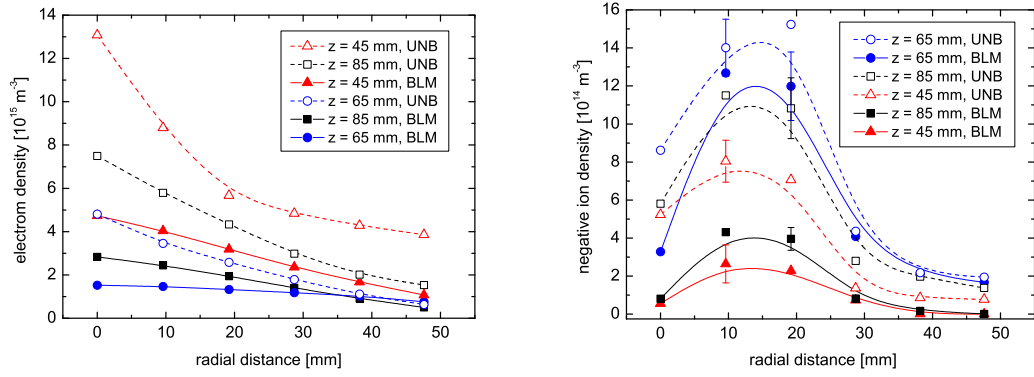
a) radial dependences of n_e **b)** radial dependences of n_n

Fig. 6.7: Radial dependences of: **a)** electron density n_e and **b)** negative ion density n_n; $p = 0.7$ Pa, $z = 45, 65, 85$ mm, $r = 0$ mm, Ar (19.6 sccm), O_2 (0.75 and 1.5 sccm).

The radial profile of n_e is higher in UNB roughly by factor two compared to BLM. Stronger radial fall was observed only at the distance $z = 45$ mm, especially in UNB mode, see Fig. 6.7 a. The local n_e minimum is located at the distance $z = 65$ mm. This local density minimum is accompanied by the maximum of the electron temperature T_e (Fig. 6.6 b) as well as by the maximum of negative ion density in Fig. 6.7 b. As it is shown in Fig. 6.7 b, the n_n strongly depends on the radial position and - contrary to the n_e distribution - its maximum is shifted to the distance $r \approx 15$ mm. The pronounced inhomogeneous distribution of oxygen ions can be maintained due to their smaller diffusion coefficient. At the position of the peak the racetrack is located, which is easy visible as an erosion rill. At larger radial positions the negative ion densities are very low, $n_n \approx 10^{11-13}$ m^{-3}. Such small values are burden with large computational error but in spite of this the fact that radial distribution of negative ion density exhibits local maximum shifted apart from the symmetry axis is evident. This behaviour was observed in both BLM and UNB modes.

The ion density ratio n_n/n_p represents fraction of negative charge carried by negative ions. This quantity is depicted in Fig. 6.8 in dependence on the applied dc power. The BLM and UNB modes show opposite trends.
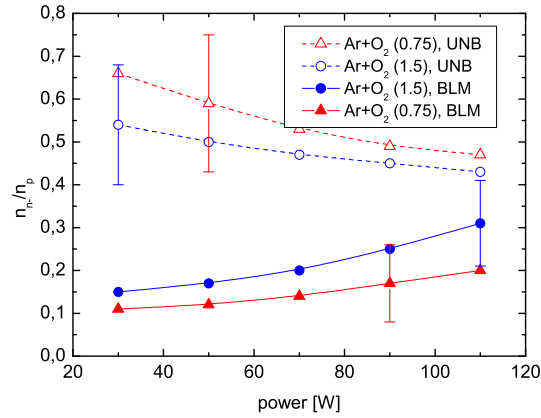
Fig. 6.8: Dependence of n_n/n_p on power.

The dependences of plasma potential V_{pl} vs. power are similar to dependences T_e vs. power, see Fig. 6.6. Addition of oxygen somewhat increases V_{pl} at lower dc power ($P = 50\,\mathrm{W}$). However, it is difficult to state generally that these differences are due to the presence of O_2 in the plasma as they are smaller than $10\,\%$ and the error of measured values is estimated around $20\,\%$. Plasma potential cannot be fully characterized by the power as it strongly depends on the cathode voltage.

6.4 Time-resolved diagnostics of pulsed discharge during deposition of TiO_x layers

The dc unbalanced magnetron with Ti target, described in chapter 6.1, is being mainly used for deposition of nanocrystalline TiO_x thin films. Plasma density is the most important parameter which influences deposition efficiency. Hence, magnetron configuration was operated in pulsed regime, see chapter 3.2.1. For this reason, we selected the conditions more similar to high power magnetrons with high peak power densities but small repetition frequencies. Experimental conditions as the instant value of discharge current I_p, gas pressure in the reactor p, gas mixture ratio Ar/O_2 etc., were varied in a broad range. The time evolutions of plasma parameters as electron density n_e, electron temperature T_e, plasma potential V_{pl} and EEPF

were determined during the modulation cycle of pulse discharge excitation. The presented results of temporal and spatial plasma parameters distribution supplement current knowledge about low-frequency pulsed magnetron discharge with Ti target applied for the TiO_x thin films deposition.

6.4.1   Experimental conditions and probe data evaluation

The UNB magnetron was operated in pulsed regime with the lower repetition frequency of modulation cycle. The maximum peak current I_p was limited by technical equipment up to 20 A while much lower average current I_{av} was used. Due to its low value we had to use low repetition frequency $\nu_p = 250\,Hz$ in order to achieve maximum peak current 20 A. The length of the active part of the modulation cycle was set up on $T_a = 150\,\mu s$ in order to reach maximum electron concentration as it will be described later. Pure Ar and mixtures Ar/O_2 were used for pulsed magnetron discharge ignition. Flow rate of Ar was kept constant at 19.5 sccm in all experiments. Mixture of Ar and O_2 gasses was created by adding of 0.5, 1.5, 4.5, 8.0 sccm of O_2 respectively. The pressure in the chamber was typically kept at 5 Pa. The maximum peak discharge current was 15 A (in Ar/O_2) and 20 A in pure Ar discharge. In all figures and graphs, only details of single time period 0-500 μs is depicted. Assuming radial symmetry, plots of radial profile include only a half of the total curve. Presented data are interlaid by B-spline curves.

The plasma was excited by combination of dc voltage supply working up to dc voltage -620 V and maximum dc current 1 A and by pulse modulator with high parallel input capacity. This system was capable to excite dc pulse magnetron discharge with maximum average current 1 A but with maximum instant current roughly about 20 A in a pulse. In series with the discharge path a ballast resistor ($R = 15\,\Omega$) was inserted in order to avoid arcing and to stabilize the discharge current.

Apparatus for time resolved Langmuir probe measurement, described in chapter 5.1.1 was used for the experiment. Time resolution of the acquisition unit with input amplifiers was better than 5 μs. The time response of all the Langmuir probe system was tested with rectangular current pulses

added to the probe tip. This measurement confirmed that time response of the system is shorter than $5\,\mu$s.

Probe voltage V_{p} was measured relative to the grounded body of the vacuum vessel. The probe voltage relative to the plasma potential is then described $V \equiv V_{\mathrm{p}} - V_{\mathrm{pl}}$, where V_{pl} denotes the plasma potential. The voltage at which the probe current is zero is floating potential V_{fl}. The second derivative of the electron current characteristics in the retarding region determines the electron energy probability function, defined by (4.4), with energy $E/e \equiv -V$ measured in volts.

Assuming Maxwellian electron energy distribution, the dependence of the electron current on the voltage V can be described using equations (4.8) and (4.9) as

$$i_{\mathrm{e}} \;=\; eA_{\mathrm{p}}n_{\mathrm{e}} \cdot \sqrt{\frac{eT_{\mathrm{e}}}{2\pi m_{\mathrm{e}}}} \cdot \exp\left(\frac{V}{T_{\mathrm{e}}}\right), \qquad V \;<\; 0, \tag{6.12}$$

$$i_{\mathrm{e}} \;=\; eA_{\mathrm{p}}n_{\mathrm{e}} \cdot \sqrt{\frac{eT_{\mathrm{e}}}{2\pi m_{\mathrm{e}}}} \cdot \left(1 + \frac{V}{T_{\mathrm{e}}}\right)^{1/2}, \; V \;>\; 0, \tag{6.13}$$

where e is elementary charge, A_{p} is the probe surface, T_{e} is the electron temperature measured in volts and m_{e} and n_{e} are the electron mass and the electron number density, respectively. A computer code enabling comprehensive processing of the probe characteristics has been developed. The n_{e} and T_{e} are determined by fitting the electron current characteristics according to formulas (6.12, 6.13) since in all cases we were able to approximate the electron distribution by Maxwellian function; see next chapter and Fig. 6.12 a. T_{e} determined in this way corresponds within an error of a few percent with the electron temperature T_{eff} determined by integration of electron distribution function according to (4.14).

6.4.2   Results and discussion of time-resolved measurements

The time evolution of the instant discharge current during the whole modulation cycle was measured. First this measurement was done only with ballasting resistor, which worked as a dummy load without magnetron discharge. Current and voltage waveforms were practically rectangular with negligible

error in this case. The instant current and voltage at the resistor dropped to zero when the active part of the modulation cycle ended. These tests were performed for different currents in the resistor up to maximum 25 A in the peak and maximum voltage -375 V. The same repetition frequency and duty cycle were used both at these tests and for the experiments with magnetron discharge. The switching time delay was of order of nanoseconds.
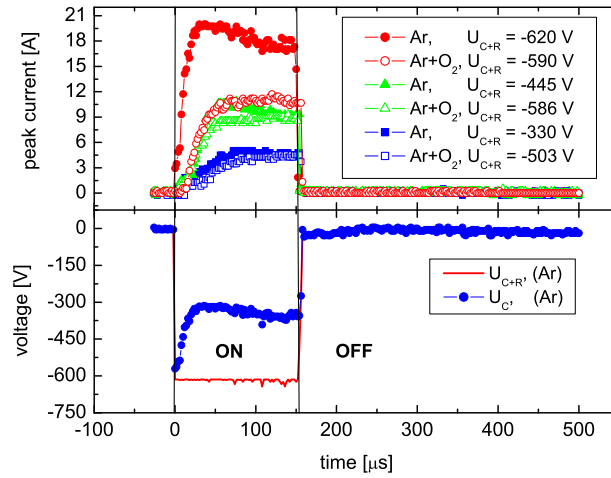

Fig. 6.9: **upper)** Time evolution of peak current in active pulse, $p = 5$ Pa, Ar 19.5 sccm, O_2 1.5 sccm, **lower)** time evolution of voltage U_{C+R} and U_C in pure Ar (-620 V).

Evolution of the magnetron discharge current is in Fig. 6.9 for different composition of gas mixture Ar/O_2 and different maximum voltage on the serial connection of ballasting resistor and magnetron cathode U_{C+R}. Time evolution of the cathode voltage U_C measured directly on the cathode is also shown in Fig. 6.9. The measured U_{C+R} was constant during the active part of modulation cycle for all the investigated conditions. Instant discharge current was linearly increasing in the first 30 - $70\,\mu s$ of the modulation cycle before it reached the maximum value (Fig. 6.9). Duration of this increase was dependent on the maximum current in the peak. This duration was shorter for higher current peak. The behaviour is an effect of the plasma impedance evolution because U_{C+R} has a constant magnitude during all the active part of modulation cycle from its beginning. Similar effect of slow current increase was observed, for example, in [94].

Determination of electron density in pulsed magnetron

Figs. 6.10 and 6.11 show the time evolution of electron density n_e within the modulation cycle. It is obvious, see Fig. 6.10 a, that n_e is strongly influenced by the distance from the target. Near the target ($z = 15$ mm) n_e reached $n_e \simeq 1.3 \times 10^{18}\,\mathrm{m}^{-3}$ in pure Ar and $n_e \simeq 3 \times 10^{17}\,\mathrm{m}^{-3}$ in the mixture of Ar/O$_2$. During the active part of modulation cycle, n_e always reached maximum value in the interval between 50 - $100\,\mu$s, with correlation with the time evolution of the discharge current (Fig. 6.9).
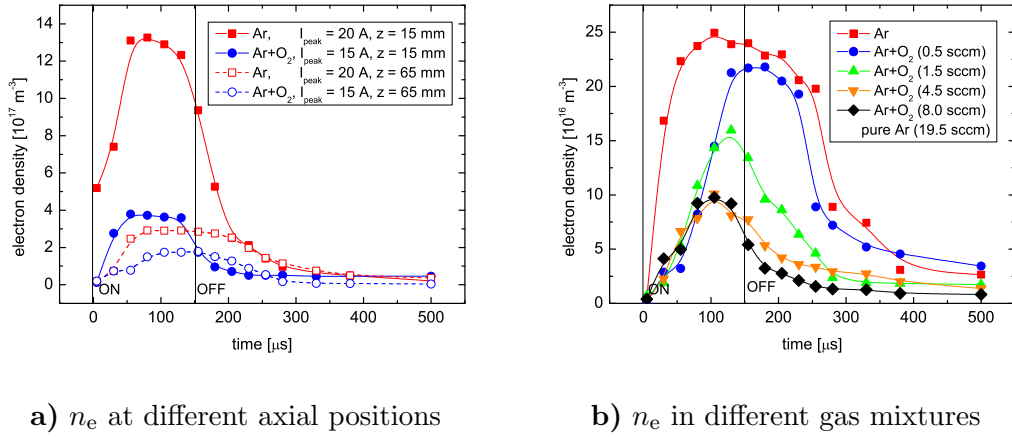

a) n_e at different axial positions   **b)** n_e in different gas mixtures

Fig. 6.10: Temporal evolutions of n_e: **a)** at different axial positions Ar 19.5 sccm, O$_2$ 1.5 sccm, $p = 5$ Pa, $r = 0$ mm, $T_{\mathrm{period}} = 4$ ms, **b)** in different Ar/O$_2$ ratio mixtures, Ar 19.5 sccm, O$_2$ 0.5, 1.5, 4.5, 8.0 sccm, $p = 5$ Pa, $r = 0$ mm, $z = 65$ mm, $T_{\mathrm{period}} = 4$ ms, $I_p = 10$ A.

It was shown that with increasing oxygen percentage in the gas mixture n_e decreases, although the instant discharge current is the same. This phenomenon is clearly illustrated in Fig. 6.10 b where the maximum discharge current in the active part of modulation cycle was held constant at $I_p \approx 10$ A for all gas mixture compositions. It is clear that n_e was more than twice lower in Ar/O$_2$ mixture (for O$_2$ mass flow 4.5 and 8 sccm) than in pure Ar. We suppose that this decrease is due to the presence of negative oxygen ions in the discharge. Negative atomic and molecular oxygen ions were detected in magnetron discharges in oxygen gas many times [158, 159]. Explanation that n_e decreases in oxygen due to inelastic collisions of electrons with oxygen molecules and excitation of their vibrational levels is less probable. As

it was shown in Figs. 6.12 b and 6.13 a, the presence of O_2 in the plasma increases the electron temperature T_e. Furthermore, results of n_e in Ar/N_2 gas mixture were investigated by *Petrov et al.* [160]. In this mixture the negative ions cannot be created from N_2 and N atoms. In the mentioned paper, experiments were done with Ti target and constant dc discharge current. Different amount of N_2 in Ar/N_2 gas mixture from 0 % up to 100 % was used. Only very weak decrease of n_e was observed for increasing nitrogen amount in the plasma. Electron density was $n_e \approx 6 \times 10^{17}\,\mathrm{m^{-3}}$ in pure argon and $n_e \approx 5.5 \times 10^{17}\,\mathrm{m^{-3}}$ in the mixture of N_2/Ar and even in pure N_2. Similar behavior was observed in our system in cw regime, see chap. 6.2 - if N_2 was added into the discharge, n_e even increased. Although more processes can be involved, this experiment supports our statement that the decrease of electron concentration for higher amount of O_2 was caused by negative oxygen ions. It is very probable that negative oxygen ions were generated by dissociative electron attachment as it was described in previous section 6.3, and because of this process the density of free electrons is reduced.
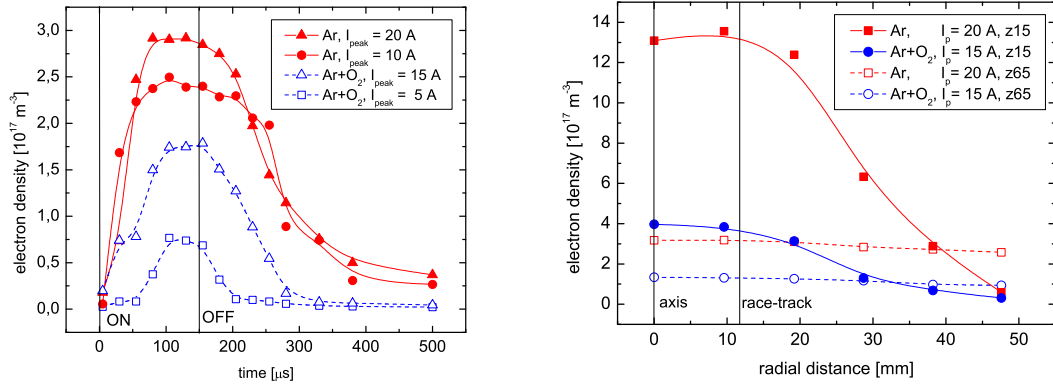
a) n_e at $z = 65\,\mathrm{mm}$ positions   **b)** radial dependences of n_e

Fig. 6.11: **a)** Temporal evolutions of n_e, Ar 19.5 sccm, O_2 1.5 sccm, $p = 5\,\mathrm{Pa}$, $r = 0\,\mathrm{mm}$, $z = 65\,\mathrm{mm}$, $T_{\mathrm{period}} = 4\,\mathrm{ms}$. **b)** Radial dependences of n_e, Ar 19.5 sccm, O_2 1.5 sccm, $p = 5\,\mathrm{Pa}$, $t = 100\,\mu\mathrm{s}$, $T_{\mathrm{period}} = 4\,\mathrm{ms}$, z15 - axial distance 15 mm from the target, z65 - axial distance 65 mm from the target.

Radial profiles of n_e are shown in Fig. 6.11 b. The shapes of the profiles were strongly influenced by the distance from the target. In the position $z = 15\,\mathrm{mm}$, the plasma is bound to the cathode and in the radial distance

$r = 30\,\mathrm{mm}$ from the target axis, the probe is practically out of the active discharge. On the contrary, near the substrate plane at $z = 65\,\mathrm{mm}$ the plasma is spread more homogeneously and n_e is almost independent on the radial distance. This fact can be utilized during the deposition process. Homogeneous layers over large substrate could be deposited at this distance.

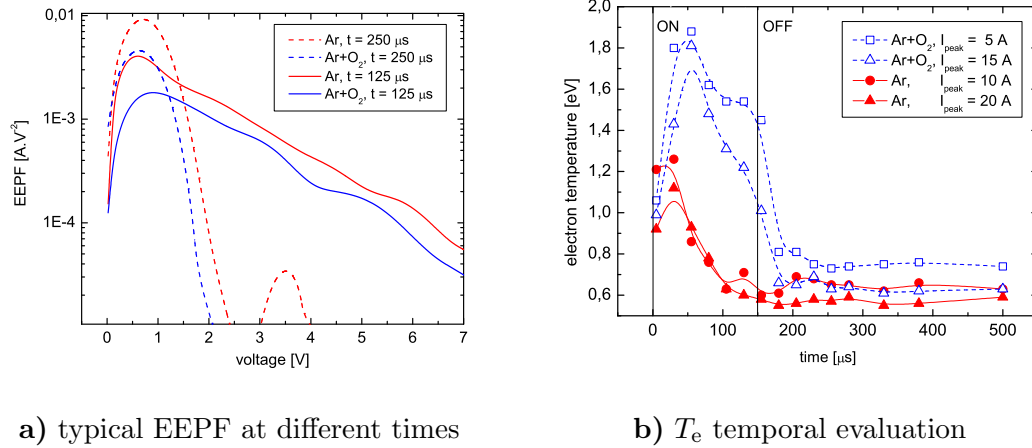**Determination of electron temperature in pulsed magnetron**

a) typical EEPF at different times   **b)** T_e temporal evaluation

Fig. 6.12: **a)** Typical EEPF at different delays after power pulse leading edge, Ar 19.5 sccm, O_2 1.5 sccm, $p = 5\,\mathrm{Pa}$, $r = 0\,\mathrm{mm}$, $T_\mathrm{period} = 4\,\mathrm{ms}$, $T_\mathrm{active} = 150\,\mu\mathrm{s}$. **b)** Temporal evolution of T_e, Ar 19.5 sccm, O_2 1.5 sccm, $p = 5\,\mathrm{Pa}$, $r = 0\,\mathrm{mm}$, $z = 65\,\mathrm{mm}$, $T_\mathrm{period} = 4\,\mathrm{ms}$.

In many works mentioned above a bi-Maxwellian electron distribution [91] with high energetic electron group was found in the magnetrons operated in pulsed regime [99, 112]. The quality of our probe data enabled us to perform investigation of EEPF. Typical results are shown in Fig. 6.12 a. We see approximately Maxwellian distribution in pure Ar discharge as well as in the mixture Ar/O_2. To verify it, we calculated the effective electron temperature T_eff from equation (4.14) and the T_e from equation (4.12), respectively. Both methods gave similar results with differences about 15 %. The effective electron temperature T_eff calculated from (4.14) was typically lower than T_e from (4.12). Since the deviations of EEPF from Maxwellian did not appear to be significant, all values of electron temperature shown below were computed from formula (4.12) under assumption of the Maxwellian EEPF.

The reason why we - contrary to other authors - did not observe bi-Maxwellian distribution function in pulse magnetron lie in the fact that we have used relatively higher pressure 5 Pa. The bi-Maxwellian function was usually found in magnetron system working at lower pressure below 1 Pa. Theoretical modelling of electron distribution function in dc cylindrical magnetron was done in [161]. In this work the dependence of EEPF on the pressure in magnetic field was studied experimentally and theoretically. Bi-Maxwellian EEPF with high-energy group was found at a pressure of 1 Pa, but above 3 Pa EEPF it was nearly Maxwellian or slightly deviated from Maxwellian with deficit of electrons at higher energies. The results of this work confirm our explanation why we did not observe bi-Maxwellian EEPF in our pulsed magnetron.
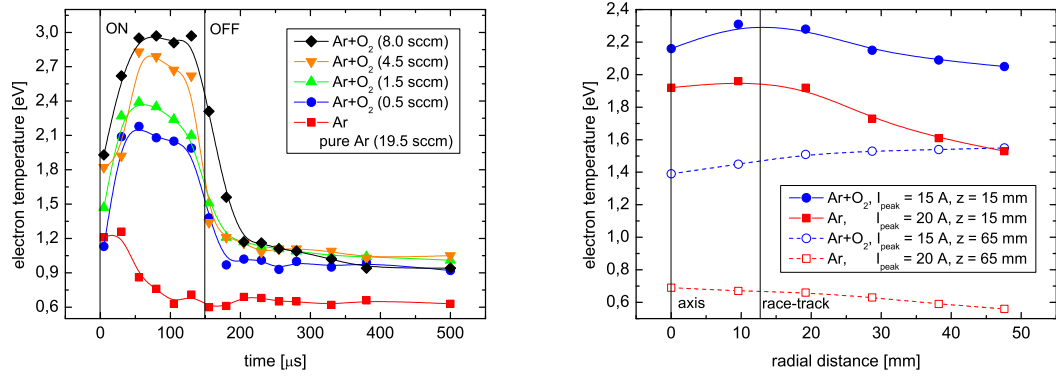
a) T_e in different gas mixtures   **b)** radial dependences of T_e

Fig. 6.13: **a)** Temporal evolutions of T_e in different Ar/O_2 ratio mixtures, Ar 19.5 sccm, O_2 0.5, 1.5, 4.5, 8.0 sccm, $p = 5$ Pa, $r = 0$ mm, $z = 65$ mm, $T_{period} = 4$ ms. **b)** Radial dependences of T_e, Ar 19.5 sccm, O_2 1.5 sccm, $p = 5$ Pa, $t = 100 \mu s$, $T_{period} = 4$ ms, $z = 15$ mm and $z = 65$ mm from the target.

Time evolution of electron temperature T_e during the first $500 \mu s$ of modulation cycle is depicted in Figs. 6.12 b and 6.13 a. T_e reaches its maximum faster (20 - 50 μs after onset of the active part of modulation cycle) than n_e. After reaching local maximum T_e steeply decays. This decrease is probably caused by high density of Ti particles sputtered from the target. Ti particles can be easier ionised and excited (ionisation energy of Ti is 6.82 eV in comparison with Ar 15.8 eV). When Ti density in the plasma is high, inelastic collisions of electrons with Ti atoms decrease average electron energy. It is

expected that the density of sputtered Ti atoms in the plasma gradually increases from the beginning to the end of the active part of modulation cycle. The described dependence is evident in pure Ar - Figs. 6.12 b, and 6.13 a. If O_2 is added into the discharge, T_e reached higher magnitude than in the case of pure Ar. Fig. 6.13 a shows that for higher amount of O_2 in the plasma T_e reaches higher magnitude and decrease of T_e after local maximum is less apparent than in the case of pure Ar. T_e is approximately constant after this local maximum up to the end of the active part of the modulation cycle for the maximum O_2 flow rate 8 sccm.

Two phenomena affect time evolution and magnitude of T_e in our cases: **(i)** The first one is connected with concentration of Ti atom in the plasma. It is well known that after adding of O_2 in the plasma the sputtering rate of Ti sharply decreases. This is caused by oxidation of the target surface. Instead of fast sputtering of Ti atoms only slow sputtering of TiO_x layer from the target surface predominates. This implies that the loss of electron energy by inelastic collisions with Ti atoms is less intensive in the presence of O_2 in the plasma and T_e is effectively higher. **(ii)** The second phenomenon, which has influence on T_e time evolution, is connected with creation of negative oxygen ions. T_e can be increased due to released energy of the magnitude of electron affinity energy.

Radial profiles of T_e above the target are depicted in Fig. 6.13 b. T_e is apparently higher at the target ($z = 15$ mm) than at the plane $z = 65$ mm. High energetic electrons created near by cathode are trapped by strong magnetic field at the target. They can escape from the magnetic trap only due to elastic and inelastic collisions with atoms and molecules. Due to these collisions they lose their energy during diffusion process into higher distances from the target.

Determination of plasma potential in pulsed magnetron

Time evolution of the plasma potential V_{pl} during modulation cycle is shown in Fig. 6.14 a. At the beginning of the active pulse, the plasma potential was negative. During the active part of the modulation cycle the absolute value of $|V_{pl}|$ decreased. This phenomenon of negative V_{pl} and $|V_{pl}|$ decrease was also

observed in [99, 102]. Negative V_{pl} was also observed in [101]. The authors explain it by a thin oxide layer covering walls of the reaction chamber.
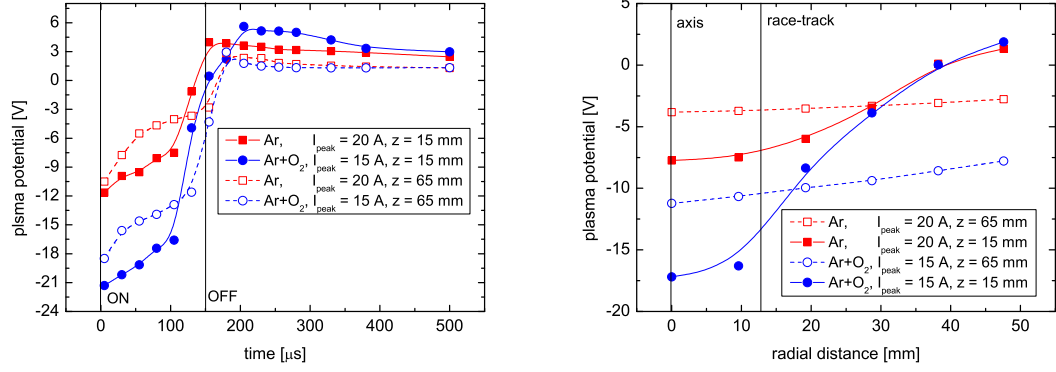
a) temporal evolution of V_{pl} **b)** radial profiles of V_{pl}

Fig. 6.14: **a)** Temporal evolutions of V_{pl}, Ar 19.5 sccm, O_2 1.5 sccm, $p = 5$ Pa, $r = 0$ mm, $z = 15$, 65 mm, $T_{period} = 4$ ms. **b)** Radial dependences of V_{pl}, Ar 19.5 sccm, O_2 1.5 sccm, $p = 5$ Pa, $t = 100$ μs, $T_{period} = 4$ ms, $z = 15$ mm and $z = 65$ mm from the target.

On the other hand, we have observed negative V_{pl} also in pure Ar before use of O_2 in the magnetron discharge. This means that explanation due to the oxide layer on the surface of the chamber is not adequate in our case. *Vetushka et al.* [102] measured also negative V_{pl} in the pulse magnetron with graphite target and pure Ar gas. They observed negative V_{pl} also in the active part of the pulse cycle. We attribute negative value of V_{pl} and $|V_{pl}|$ decrease during the active part of the pulse to the strong electric field that appears between cathode and grounded reactor in the first instant of the active part of the modulation cycle. This field gradually relaxes, because it becomes partially shielded due to the formation of the cathode fall with positive space charge of ions and $|V_{pl}|$ decreases. This electric field logically causes that V_{pl} is more negative for $z = 15$ mm than for $z = 65$ mm. Fig. 6.14 b shows radial profiles of V_{pl} in one particular time, $t = 100$ μs. V_{pl} is almost homogenous at $z = 65$ mm but for $z = 15$ mm $|V_{pl}|$ has a maximum at the centre of the magnetron and gradually decreases for higher radial distance.

7. CONCLUSION

The work done in the frame of doctoral thesis was focused on development of new technological plasma sources or their modifications, commissioning of the sources and subsequent diagnostics of generated plasma. Ground survey of intended plasma applications was brought at the beginning, see *Introduction* in chap. 1. Two plasma sources, surfatron and dc planar magnetron, were in the main interest of investigation; basic phenomena of both are described in *Sources of technological plasmas* in chap. 3. Produced plasmas were treated by comprehensive diagnostics with the view of future technological applications. All main tasks of the thesis were successfully realized and are summarized below.

1) Plasma source working at 2.45 GHz frequency for technological applications

a) Plasma source working at microwave range of frequencies based on surfatron was constructed (chap. 5.1). The plasma source works in wide spectra of experimental conditions. Shape of exiting plasma column is mainly influenced by gas mixture composition, incoming power and pressure in chamber. So-called plasma "plume shape" was observed at lower pressures and the fog-like form was observed at higher pressures, as depicted in Fig. 5.2. The stable working conditions were mainly determined by pressure in the vessel and supplied microwave power. The range of stable working conditions is displayed as an area between two limit lines in so-called "p-P map" in Fig. 5.6. The thermal sensitive samples can be prevented from overheating using pulse mode of operation or fog-like form of discharge; described in [7B].

b) Surfatron plasmas generated under stable experimental conditions (in the proper area in "p-P maps") were investigated by double probe technique

in wide range of pressures and power. Electron temperature T_e determined from double probe data was more or less constant inside the area of "p-P map": pure Ar - $\langle T_e \rangle \approx 2.45$ eV, Ar/N$_2$ - $\langle T_e \rangle \approx 2.25$ eV and Ar/O$_2$ - $\langle T_e \rangle \approx 3.05$ eV. The radial profile of electron temperature near the outlet of the tube proved strong maxima at the plasma "plume" edges. This profile probably corresponds to azimuthally symmetric $m = 0$ mode of TM surface wave generated in the surfatron. For more detail see [1A].

Single probe measurements done in plasma "plume" created under low pressure gave main survey about plasma parameters. Electron density reached values of the order $n_e \approx 10^{15}$ m^{-3}, mean electron energy $E_m \approx 2.5$ eV and plasma potential reached positive values roughly $V_{pl} \approx 5$ V. The radial profiles are influenced by shape of plasma plume, too. The values were somewhat increased using pulsed mode at the end of active part of modulation cycle. Observed increase (decrease) during the active part (pause) was more or less linear. More details can be found in [6B].

All types of investigated discharges Ar, Ar/N$_2$, Ar/O$_2$ and air-like mixtures were diagnosed by means of optical emission spectroscopy. Rotational T_r and vibrational T_v temperatures were determined as well as axial development of molecular systems. Comparison of temperatures T_e and T_v, which usually correspond to each other, revealed that surfatron produced plasma is not in thermodynamic equilibrium. The axial dependences of both T_r and T_v were almost linear in plasma column burning inside and also outside of the tube. Results about elementary processes involving the intensity of considered species were found in Ar/N$_2$, Ar/O$_2$ discharges. Rather high T_r, which approximates temperature of neutral particles, in Ar/O$_2$ discharge predetermined unsuitability of "plasma plume" for applications on thermal sensitive samples. Hence, oxygen-based plasma in fog-like form is better for these purposes. More details and other results can be found in previous published papers [8A, 11B - 14B].

c) Surfatron-generated plasma was used for material surface treatment, sterilisation and processing of seeds before sowing. The microwave discharge generated in Ar/O$_2$ and Ar/N$_2$ mixtures was used for this purposes. The

surface of LDPE was treated by plasma with the idea to increase its free surface energy (increase hydrophilicity). The critical surface energy of the low density polyethylene was experimentally estimated using the co-called Zisman plot: $\gamma^{\mathrm{C}} = 48.75\,\mathrm{mJ.m^{-2}}$. The total surface energy calculated according to the Lifshitz-van der Waals/acid-base theory was determined experimentally (W-G-D liquid combination), $\gamma^{\mathrm{TOT}} = 52\,\mathrm{mJ.m^{-2}}$. We concluded that the surface of LDPE material became hydrophilic after plasma treatment. This characteristic was also confirmed by measurements of contact angles between plastic material and sessile water drop. The Ar/N_2 discharge seems to be more efficient for this type of LDPE surface modification. The results were also published in [3B, 4B].

The bactericidal effect of plasma generated by surfatron in the Ar/O_2 and Ar/N_2 mixtures was assessed. The defined bacteria cultures were exposed to the generated plasma and the areas of inhibition zones were measured. Preliminarily, it can be concluded that the bactericidal agent generated by the surfatron-plasma is more effective for the gram-negative bacteria. For the gram-positive bacteria the sterilisation efficiency is lower or the process is ineffective at all; see [3A].

The bactericidal effect of Ar/O_2 discharge probably plays significant role also in stimulation process of seed germination. The germination increased after plasma treatment by more than three times from $15\,\%$ up to $50\,\%$. The percentage of successfully germinated seeds was calculated by standard statistical methods from large amount of seeds. The effect influencing seed germination after plasma treatment might be the erosion of the seed protective coat by the plasma treatment. More details in [3B, 4B].

2) Planar magnetron plasma source for deposition of thin films

a) Conventional dc planar magnetron was investigated in continuous regime at first. The substrate region during sputtering of Ti was investigated in Ar, Ar/N_2, Ar/O_2 discharges. Langmuir probe measurements and plasma process measurements were carried out. Influence of balanced and unbalanced mode, discharge power, pressure, N_2 or O_2 flow and the sputtered Ti were studied. The electron density in pure Ar discharge reached $n_{\mathrm{e}} \approx 10^{15}\,\mathrm{m^{-3}}$

and increases linearly with power. Presence of N_2 in discharge increases n_e roughly about one order of magnitude. Mean electron energy E_m has a maximum around $P \approx 70\,W$. Decrease of energy at higher power is probably caused by ionisation of sputtered Ti particles. Plasma monitoring showed strong increase of the amount of Ti^+ ions at powers higher than $70\,W$. Plasma potential V_{pl} expressed similar qualitative behavior like E_m with positive values about $5\,V$. More detail in [6A, 7A, 15B].

The Ar/O_2 mixture was also investigated by Langmuir probe method. Presence of O_2 agents decreased n_e and increased T_e. Plasma monitoring confirmed presence of negative atomic oxygen ions O^-. Density of negative ions was calculated by developed method based on comparison of Langmuir probe data taken in pure Ar discharge and in Ar/O_2 discharge. Electron temperature T_e and plasma potential V_{pl} have local maxima around $70\,W$. Electron density n_e and negative ion density n_n are related to each other. The measured negative ion density ($n_n \approx 10^{14}\,m^{-3}$) is roughly about one order of magnitude smaller than electron density ($n_e \approx 10^{15}\,m^{-3}$). Negative ion density strongly depends on radial distance from the target (cathode) axis. Presented results suggest that negative ions originate at the distance around $z = 65\,mm$ from the target by dissociative electron attachment where T_e reaches its maximum and n_e minimum. Other results related to this point were presented in [8B-10B].

b, c) The current cw magnetron was converted to the pulse operating system. The plasma was excited by pulse-modulated dc voltage. This system was capable to excite dc pulse magnetron discharge with average current $1\,A$ but with instant current up to $25\,A$ in a pulse. The main aim of this part was to study spatial and temporal distribution of the plasma parameters under pulsed regime with modulation frequency $250\,Hz$ and active pulse length $150\,\mu s$. Time-resolved Langmuir probe technique was used for the determination of basic plasma parameters. The main results are summarized below.

Electron density reached maximum $n_e \approx 10^{18}\,m^{-3}$ in the distance $z = 15\,mm$ from the target and $n_e \approx 3 \times 10^{17}\,m^{-3}$ at a distance $z = 65\,mm$ (suitable plane

for deposition with homogeneous profile of electron density). Hence, operation of magnetron in pulse regime increased electron density by at least two orders of magnitude. Presence of O_2 decreased n_e probably due to the creation of negative oxygen ions. Electron density reached its maximum value after $50\text{-}100\,\mu$s from the beginning of the active part of modulation cycle. This justifies lower repetition frequency of pulses. The length of the active part of the modulation cycle should be at least $100\,\mu$s if the highest electron concentration in the discharge is required.

Electron temperature steeply decreased during the active part of the pulse. This effect is probably caused by ionisation and excitation of sputtered Ti atoms and energy losses during ionisation processes. EEPF was calculated from the measured data and the distribution similar to the Maxwellian one was found. Presence of O_2 increased electron temperature. Absolute value of the plasma potential $|V_{pl}|$ decreased during the active part of modulation cycle from negative values at the beginning up to positive values in off time of the modulation cycle. For more detail see $[2A, 4A, 1B]$.

BIBLIOGRAPHY

[1] L. Tonks, I. Langmuir, *Phys. Rev.*, **33**, (1929), 876.

[2] F. F. Chen, *Introduction to Plasma Physics*, **Plenum Press**, (1974).

[3] A. Rutscher, H. Deutsch, *Wissensspeicher Plasmatechnik*, **VEB Fachbuchverlag Leipzig**, (1983).

[4] R. Hippler et al *Low Temperature Plasma Physics*, **Wiley-VCH**, (2001).

[5] M. A. Lieberman, A. J. Lichtenberg, *Principles of Plasma Discharges and Materials Processing*, **Willey and Sons**, (1994).

[6] G. A. Abraham, P. M. Fontini, T. R. Cuadrado, J. Appl. Polymer Sci. **65(6)**, (1997).

[7] M. Moisan, J. Barbeau, J. Pelletier, Sci. Tech. Appl. **299**, (2001), 102.

[8] M. Moisan, J. Barbeau, S. Moreau, J. Pelletier, M. Tabrizian, L'H. Yahia, Int. J. Pharm. **299**, (2000), 1.

[9] J. Pelletier, Agressologie **33**, (2001), 105.

[10] S. Lerouge, M. R. Werthimer, L'H. Yahia, Plasma and Polymers **6**, (2001), 175.

[11] S. Lerouge, M. R. Werthimer, R. Marchand, M. Tabrizian, L'H. Yahia, J. Biomed. Mater. Res. **52**, (2000), 128.

[12] S. Moreau, M. Moisan, M. Tabrizian, et al., J. Appl. Phys. **88**, (2000), 1166.

[13] M. Moisan, J. Barbeau, M. C. Crevier et al., Pure Appl. Chem. **74**, (2002), 349.

[14] C. L. Nelson, T. J. Berger, Curr. Microbiol. **18**, (1989), 275.

[15] K. Kelly-Wintenberg, A. Hodge, T. C. Montie et al., J. Vac. Sci. Technol. **A17(4)**, (1999), 1539.

[16] S. Hury, D. R. Vidal, F. Desor, J. Pelletier, T. Lagarde, Letters in Appl. Microbiol. **26**, (1998), 417.

[17] K. Kelly-Wintenberg, T. C. Montie, C. Brickman et al., J. Indust. Microbiol. Biotechnol. **20**, (1998), 69.

[18] A. Ricard, V. Monna, Plasma Sources Sci. Technol. **11**, (2002), A150.

[19] S. Willeger, S. Cousty, A. Ricard, M. Sixou, J. Phys. D: Appl. Phys. **36**, (2003), L60.

[20] E. Stoffels, A. J. Flikweert, W. W. Stoffels, G. M. W. Kroesen, Plasma Sources Sci. Technol. **11**, (2002), 383.

[21] R. E. J. Sladek, E. Stoffels, J. Phys. D: Appl. Phys. **38**, (2005), 1716.

[22] A. E. Dubinov, E. M. Lazarenko, V. D. Selemir, IEEE Transac. on Plasma Sci. **28(1)**, (2000), 180.

[23] S. Zivkovic, N. Puac, Z. Giba, D. Grubisic, Z. L. Petrovic, Seed Sci. and Technol. **32**, (2004), 693.

[24] J. C. Volin, F. S. Denes, R. A. Young, S. M. T. Park, Corp Sci. **40**, (2000), 1706.

[25] F. Denes, S. Mnolache, R. A. Young, J. Photopolymer Sci. Technol. **12(1)**, (1999), 27.

[26] J. R. Roth, *Industrial Plasma Engineering, volume 2*, **IoP**, (2001).

[27] R. dAgostino, P. Favia, C. Oehr, M. R. Werheimer, Plasma Process. Polym. **2**, (2005), 7.

[28] W.J. van Ooij, S. Luo, S. Datta, Plasma and Polymers, **4**, (1999), 33.

[29] R. Barni, C. Riccardi, E. Selli et al., Plasma Process. Polym. **2**, (2005), 64.

[30] J. H. Choi, E. S. Lee, H. K. Baik et al., Plasma Sources Sci. Technol. **14**, (2005), 363.

[31] J. Janca, P. Stahel, J. Buchta, D. Subedi, F. Krcma, J. Pryckova, Plasmas and Polymers **6**, (2001), 15.

[32] Masuda et al., IEEE Trans. Ind. Appl. **24**, (1988), 223.

[33] M. Simor, J Rahel, P. Vojtek, A. Brablec, M. Cernak, App. Phys. Letters **81**, (2002), 2716.

[34] P. Stahel, J. Janca, D. Subedi, Czech. J. of Phys (Suppl. D) **52**, (2002), 750.

[35] R. K. Waits, J. Vac. Sci. Technol. **15(2)**, (1978), 179.

[36] J. A. Thornton, J. Vac. Sci. Technol. **15(2)**, (1978), 171.

[37] J. Musil, J. Vlcek, Surf. Coat. Technol. **112**, (1999), 162.

[38] J. Musil, A. J. Bell, A. Rajsky, M. Cepera, J. Zeman, Fyzika **A4**, (1995), 351.

[39] J. Musil, M. Misina, D. Hovorka, J. Vac. Sci. Technol. **A15(4)**, (1997), 1999.

[40] P. Spatenka, I. Leipner, J. Vlcek, J. Musil, Plasma Sources Sci. Technol. **6**, (1997), 46.

[41] J. Musil, K. Rusnak, V. Jeek, J. Vlcek, Vacuum **46**, (1995), 46.

[42] J. Musil, P. Baroch, IEEE Transaction on Plasma Science **33(2)**, (2005), 338.

[43] Z. Zakrzewski, M. Moisan, V. M. M. Glaude, C. Beaudry, P. Leprince, Plasma Phys. **17**, (1977), 77.

[44] Z. Zakrzewski, M. Moisan, *Surface-waves in Plasmas and Solids*, World Scientific, Singapore (1986), 440.

[45] H. Nowakowska, Z. Zakrzewski, M. Moisan, J. Phys. D: Appl. Phys. **34**, (2001), 1474.

[46] V. M. M. Glaude, M. Moisan, R. Pantel, P. Leprince, J. Marec, J. Appl. Phys. **51**, (1980), 5693.

[47] M. Moisan, C. M. Ferreira, Y. Hajlaoui, Revue Phys. Appl. **17**, (1982), 707.

[48] Z. Zakrzewski, J. Phys. D: Appl. Phys. **16**, (1983), 171.

[49] A. Shivarova, I. Zhelyazkov , J. Plasma Phys. **20**, (1978), 1049.

[50] M. Moisan, J. Pelletier, *Microwave Excited Plasmas*, **Elsevier**, (1992).

[51] M. Moisan, C. Beaudry, P. Leprince, IEEE Trans. Plasma Sci. **3**, (1975), 55.

[52] M. Moisan, Z. Zakrzewski, R. Pantel, J. Phys. D: Appl. Phys. **12**, (1979), 219.

[53] M. Moisan, R. Grenier, Z. Zakrzewski, Spectrochim. Acta **8**, (1995), 781.

[54] J. Hubert, M. Moisan, Z. Zakrzewski, Spectrochim. Acta **41B**, (1986), 205.

[55] C. M. Ferreira, J. Phys. D: Appl. Phys. **14**, (1981), 1811.

[56] H. Nowakowska, Z. Zakrzewski, M. Moisan, M. Lubanski, J. Phys. D: Appl. Phys. **31**, (1998), 1422.

[57] J. Vyskocil, J. Musil, J. Phys. D: Appl. Phys. **13**, (1980), L25.

[58] J. Musil, J. Vyskocil, Z. Zakrzewski, Acta Phys. Slov. **2**, (1986), 111.

[59] M. Moisan, Z. Zakrzewski, J. Phys. D: Appl. Phys. **24**, 1991, 1025.

[60] M. Chaker, M. Moisan, Z. Zakrzewski, Plasma Chem. Precess **6**, (1986), 79.

[61] C. M. Ferreira, J. Phys. D: Appl. Phys. **22**, (1989), 705.

[62] U. Kortshagen, H. Schluter, A. Shivarova, J. Phys. D: Appl. Phys. **24**, (1991), 1571.

[63] U. Kortshagen, A. Shivarova, E. Tatatova, D. Zamfirov, J. Phys. D: Appl. Phys. **27**, (1994), 301.

[64] S. Grosse, H. Schluter, E. Tatatova, Plasma Sources Sci. Technol. **3**, (1994), 545.

[65] E. Tatarova, F. M. Dias, C. M. Ferreira et al., J. Phys. D: Appl. Phys. **30**, (1997), 2663.

[66] K. Ivanova, I. Koleva, A. Shivarova, Plasma Sources Sci. Technol. **4**, (1995), 444.

[67] L. Dountchev, I. Koleva, A. Shivarova, Plasma Sources Sci. Technol. **5**, (1996), 531.

[68] J. Berndt, K. Makasheva, H. Schluter, A. Shivarova, Plasma Sources Sci. Technol. **11**, (2002), 208.

[69] V. Guerra, J. Loureiro, Plasma Sources Sci. Technol. **8**, (1999), 110.

[70] E. Tatarova, F. M. Dias, H. van Kuijk, C. M. Ferreira et al., Vacuum **69**, (2003), 189.

[71] P. Merel, M. Tabbal, M. Chaker, M. Moisan, A. Ricard, Plasma Sources Sci. Technol. **7**, (1998), 550.

[72] V. Guerra, E. Tatarova, F. M. Dias, C. M. Ferreira et al., J. Phys. D: Appl. Phys. **91(5)**, (2002), 2648.

[73] M. Moisan, J. Hubert, J. Margot, Z. Zakrzewski, *Advanced Technologies Based on Wave and Beam Generated Plasmas*, Kluwer Acad. Publish., Netherlands (1999), 23.

[74] J. Musil, Vacuum **36(1-3)**, (1986), 169.

[75] J. Musil, Vacuum **2**, (1996), 145.

[76] S. Kvasnica, P. Adamek, P. Spatenka, IEEE Transaction on Plasma Science. **33(2)**, (2005), 364.

[77] A. E. Wendt, M. A. Lieberman, H. Meuth, J. Vac. Sci. Technol **A6 (3)**, (1988), 1827.

[78] J. W. Bradley, Plasma Sources. Sci. Technol. **5**, (1996), 622.

[79] B. Window, N. Savvides, J. Vac. Sci. Technol. **A4(3)**, (1986), 196.

[80] T. E. Sheridan, M. J. Goeckner, J. Goree, J. Vac. Sci. Technol. **A8(1)**, (1990), 30.

[81] T. E. Sheridan, M. J. Goeckner, J. Goree, J. Vac. Sci. Technol. **A(9)**, (1991), 301.

[82] J. E. Miranda, M. J. Goeckner, J. Goree, T. E. Sheridan, J. Vac. Sci. Technol. **A(8)**, (1990), 1627.

[83] T. E. Sheridan, M. J. Goeckner, J. Goree, J. Vac. Sci. Technol. **A8(3)**, (1990), 437.

[84] T. E. Sheridan, J. Goree, J. Vac. Sci. Technol. **A7(3)**, (1989), 1014.

[85] M. J. Goeckner, J. Goree, T. E. Sheridan, IEEE Transaction on Plasma Science **19(2)**, (1991), 301.

[86] J. W. Bradley, S. Thompson, Y. A. Gonzalvo, Plasma Sources. Sci. Technol. **10**, (2001), 490.

[87] J. W. Bradley, G. Lister, Plasma Sources. Sci. Technol. **6**, (1997), 524.

[88] W. Trennpohl, J. Bretagne, G. Gouset, D. Pagmon, M. Touzeau, Plasma Sourses Sci. Technol. **(5)**, (1996), 607.

[89] F. Debal, J. Bretagne, M. Jumet, et al, Plasma Sources Sci. Technol. **(7)**, (1998), 219.

[90] F. Debal, J. Bretagne, J. P. Dauchot, M. Hecq, M. Wautelet, Plasma Sources Sci. Technol. **(10)**, (2001), 30.

[91] V. A. Godyak, R. B. Piejak, B. M. Alexandrovich, Plasma Sources. Sci. Technol. **1**, (1992), 179.

[92] T. E. Sheridan, M. J. Goeckner, J. Goree, J. Vac. Sci. Technol. **A9(3)**, (1991), 688.

[93] V. Stranak, H. Steffen, S. Wrehde, R. Hippler, M. Tichy, J. Phys. Vol. **54**, Suppl. C, (2004), 826.

[94] J. Vlcek, A. Pajdarova, J. Musil, Contribution to Plasma Phys. **44**, (2004), 426.

[95] P. Baroch, J. Musil, J Vlcek, K.H. Nam, J.G. Han, Surf. Coat. Technol. **193**, (2005), 107.

[96] D. Gloss, P. Frach, O. Zywitzki, et al., Surf. Coat. Technol. **200**, (2005), 967.

[97] H. Klostermann, B. Bocher, F. Fietzke, T. Modes, O. Zywitzki, Surf. Coat. Tech. **200**, (2005), 760.

[98] J.W. Bradley, H. Backer, Surf. Coat. Sci. Technol. **200**, (2005), 616.

[99] H. Backer, J.W. Bradley, Plasma Sources Sci. Technol. **14**, (2005), 419.

[100] S-H. Seo, J-H. Hwan, H-Y. Chang, J-G. Han, J. Appl. Phys. **98**, (2005), 43301.

[101] A. Belkin, A. Freilich, J. Lopez et al., New Journal of Physics **7**, (2005), 1367.

[102] A. Vetushka, S. K. Karkari, J. W. Bradley, J. Vac. Sci. Technol. **A22(6)**, (2004), 2459.

[103] T. Dunger, T. Wenzel, S. Wenzel, F. Richter, Surf. Coat. Technol. **200**, (2005), 1676.

[104] T. Wenzel, T. Dunger, S. Welzel, H. Kupfer, F. Richter, Surf. Coat. Technol. **200**, (2005), 630.

[105] H. Backer, P. S. Henderson, J. W. Bradley, P. J. Kelly, Surf. Coat. Technol. **174-175**, (2003), 909.

[106] P. J. Kelly, C. F. Beevers, P. S. Henderson et al., Surf. Coat. Sci. Technol. **174-175**, (2003), 795.

[107] S. Ohno, D. Sato, M. Kon, et al., Japanese Journal of Appl. Phys. **43**, (2004), 8234.

[108] A.A. Onifade, P.J. Kelly, Thin Solid Films **494**, (2006), 8.

[109] V. Kouznetsov, K. Macak, J.M. Schneider, U. Helmersson, I. Petrov, Surf. Coat. Technol. **122**, (1999), 290.

[110] K. Macak, V. Kouznetsov, J.M. Schneider, U. Helmersson, J. Vac. Sci. Technol. **A(18)**, (2000), 1533.

[111] J.T. Gudmundsson, J. Alami, U. Helmersson, Surf. Coat. Technol. **161**, (2002), 3427.

[112] J.T. Gudmundsson, J. Alami, U. Helmersson, Appl. Phys. Lett. **78**, (2001), 249.

[113] A. P. Ehiasarian, W. D. Munz, L. Hultman, U. Helmersson, I. Petrov, Surf. Coat. Technol. **(163-164)**, (2003), 267.

[114] A. P. Ehiasarian, P. E. Hovsepian, L. Hultman, U. Helmersson, Thin Solid Films **(457)**, (2004), 270.

[115] J. Musil, J. Lestina, J. Vlcek, T. Togl, J. Vac. Sci. Technol. **19**, (2001), 420.

[116] J. W. Bradley, H. Backer, Y Aranda-Gonzalvo, P. J. Kelly, R. D. Arnell, Plasma Sources Sci. Technol. **11**, (2002), 165.

[117] J. W. Bradley, S. K. Karkari, A. Vetusha, Plasma Sources Sci. Technol. **13**, (2004), 189.

[118] R. H. Huddlestone, S. L. Leonard, *Plasma Diagnostic Technigues*, **Academic Press, London**, (1965).

[119] I. Langmuir, H. M. Mott-Smith, Phys. Rev. **28**, (1926), 727.

[120] S. Pfau, M. Tichy, *Langmuir probe diagnostic of low-temperature plasmas*, in R. Hippler et al. *Low Temperature Plasma Physics*, **Wiley-VCH**, (2001).

[121] J. G. Laframboise, UITAS Report **100**, University of Toronto, (1966).

[122] M. Tichy, M. Sicha, P. David, T. David, Contrb. Plasma Phys. **34**, (1994), 59.

[123] J. E. Allen, R. L. F. Boyd, P. Raynolds, Proc. Phys. Soc. London **70B**, (1957), 297.

[124] I. B. Bernstein, I. N. Rabinowitz, Phys. Fluids **2/2**, (1959), 112.

[125] J.G. Laframboise, J. Rubinstein, Phys. Fluids **19**, (1976), 1900.

[126] F. F. Chen, Plasma Phys. **7**, (1965), 47.

[127] Y. S. Chou, L. Talbot, D. R. Willis, Phys. Fluids **9/11**, (1966), 2150.

[128] A. K. Jakubowski, AIAA Journal **10/8**, (1972), 988.

[129] Z. Zakrzewski, T. Kopiczynski, Plasma Physics **16**, (1974), 1195.

[130] S. Klagge, M. Tichy, Czech. J. Phys. **B35**, (1985), 354.

[131] M. J. Druyvesteyn, Zeitscher. f. Physik **64**, (1930), 781.

[132] S. C. M. Luijendijk, J. van Eck, Physica **36**, (1967), 49.

[133] B. Nuhn, G. Peter, Proc. XIII. ICPIG, Berlin, (1977).

[134] E. O. Johnson, L. Malter, Phys. Rev. **80**, (1950), 58.

[135] G. V. Marr, *Plasma Spectroscopy*, **Elsevier**, (2001).

[136] J. Janca, Czech. J. Phys. **B15**, (1965), 662.

[137] Z. Hubicka, PhD. thesis (in Czech), **Charles University in Prague, Fac. Math. Phys.**, (1998).

[138] http://www.nist.gov, *Atomic Spectral Database*.

[139] G. Hertzberg, *Molecular Spactra and Molecular Structure*, **Van Nostrand**, (1966).

[140] C. Tesar, J. Janca, V. Kapicka, P. Slavicek, A. Hrdlicka, XV Symposium on Physics of Switching Arc, Vol I, Contributed Papers. Brno, (2003), 178, ISBN 80-214-2307-2.

[141] P. Slavicek, Diploma thesis (in Czech), **Masaryk University in Brno, Fac. Nat. Sci.**, (1996).

[142] P. Adamek, PhD. thesis (in Czech), **Charles University in Prague, Fac. Math. Phys.**, (1999).

[143] P. Kudrna, PhD. thesis (in Czech), **Charles University in Prague, Fac. Math. Phys.**, (1997).

[144] Programme documentation, *Using MATLAB*, **The MathWorks Inc. USA**, (2000).

[145] J. Margot, M. Moisan, A. Ricard, Appl. Spectroscop. **45**, (1991), 260.

[146] V. Kudrle, P. Vasina, A. Talsky, J. Janca, Czech. J. Phys. **52(D)**, (2002), 589.

[147] V. Bursikova, P. Stahel, Z. Navratil, J. Janca, Surface Energy Evaluation by Contact Angle Measurements, *Masaryk University*, Brno, (2004), ISBN 80-210-3563-3.

[148] Z. Navratil, V. Bursikova, P. Stahel, M. Sira, P. Zverina, Czech. J. Phys., Suppl. C, **54**, (2004), C877.

[149] J. Julák, V. Kříha and V. Scholtz, Czech. J. Phys., Suppl. B, **56**, (2006), B1333.

[150] Instruction Manual VTech75 UHV Gencoa, Gencoa Ltd, Liverpool, United Kingdom, (1997).

[151] H. Vogel, Gehrtsen Physik, Springer, Heidelberg, Berlin, (1995), 225. (in German).

[152] K. Ellmer, R. Wendt, K. Wiesemann, Int. J. Mass. Spectrom., **223-224**, (2002), 679.

[153] H. Amemiya, J. Phys., **23**, (1990), 999.

[154] M. Shindo, Y. Kawai, Surf. and Coat. Technol. **142-144**, (2001), 355.

[155] M. Shindo, S. Hiejema, Y. Ueda, S. Kawakami, N. Ishii, Y. Kawai, Surf. and Coat. Technol. **116-119**, (1999), 1065.

[156] N. J. Braithwaite, J. E. Allen, J.Phys. **D21**, (1988), 1733.

[157] E. Stoffels, W. W. Stoffels and K. Tachibana, Rev. Sci. Instrum., Vol. **69**, No. 1, (1998), 11.

[158] N. Martin, A. M. E. Santo, R. Sanjines, F. Levy, Surf. Coat. Technol. **138 (1)**, (2001), 77.

[159] M. Misina, J. W. Bradley, H. Backer et al, Vacuum **68(2)**, (2002), 171.

[160] I. Petrov, A. Myers, J.E. Greene, J.R. Abelson, J. Vac. Sci. Technol. **A12**, (1994), 2846.

[161] E. Passoth, J.F. Behnke, C. Csambal, et al, J.Phys. D: Appl. Phys. **32**, (1999), 2655.

LIST OF PUBLICATIONS RELATED TO THIS THESIS

Papers in international journals

[1A] <u>V. Stranak</u>, P. Adamek, J. Blazek, M. Tichy, P. Spatenka, *Probe diagnostic of microwave plasma at frequency* 2.45 GHz *in cw and pulse regime.* Contrib. Plasma Phys. **46**, No. 5–6, (2006), 439–444.

[2A] <u>V. Stranak</u>, Z. Hubicka, P. Adamek, J. Blazek, M. Tichy, P. Spatenka, R. Hippler, S. Wrehde, *Investigation of the time evolution of plasma parameters in a pulsed magnetron discharge.* Czech. J. Phys. **56**, (2006), B1364–B1370.

[3A] <u>V. Stranak</u>, V. Kriha, V. Scholtz, J. Koller, M. Tichy, P. Spatenka, *Surfatron plasma–based sterilisation*, Czech. J. Phys. **56**, (2006), B843–B847.

[4A] <u>V. Stranak</u>, Z. Hubicka, P. Adamek, J. Blazek, M. Tichy, P. Spatenka, R. Hippler, S. Wrehde, *Time–resolved probe diagnostics of pulsed dc magnetron discharge during deposition of* TiO_x *layers.* Surf. Coat. Technol. **201**, (2006), 2512–2519.

[5A] J. Blazek, P. Kriz, <u>V. Stranak</u>, P. Spatenka, *Diagnostics of low–temperature plasma by refractional methods.* Czech. J. Phys. **56**, (2006), B664–B650.

[6A] R. Hippler, S. Wrehde, <u>V. Stranak</u>, O. Zhigalov, H. Steffen, M. Tichy, M. Quaas, H. Wulff, *Characterisation of a magnetron plasma for deposition of titanium oxide and titanium nitride films.* Contrib. Plasma Phys. **45**, (2005), 348–357.

[7A] <u>V. Stranak</u>, H. Steffen, S. Wrehde, R. Hippler, M. Tichy, *Investigation of plasma parameters in the dc planar magnetron in balanced and unbalanced mode*, Czech. J. Phys. **54**, (2004), 826–827.

[8A] <u>V. Stranak</u>, P. Slavicek, Z. Navratil, P. Adamek, M. Tichy, P. Spatenka, D. Trunec, *Diagnostics of surfatron–generated plasma by probe measurements and emission spectroscopy.* Czech. J. Phys. **54**, (2004), 970–975.

[9A] P. Kriz, <u>V. Stranak</u>, J. Blazek, *Study of the parameters of barrier torch discharge.* Czech. J. Phys. **52/D**, (2002), 509–514.

Contributions in proceedings of conferences

[1B] <u>V. Stranak</u>, Z. Hubicka, P. Adamek, P. Virostko, J. Blazek, S. Wrehde, M. Tichy, R. Hippler, *Investigation of pulsed magnetron discharge at different frequencies during deposition of* TiO_x *thin films.* In: Proceedings of **SAPP XVI, 2007**, Podbanske, January 20–25, (2007), (ed. J. Matuska, S. Matejcik, J. D. Skalny), 263-264. ISBN 978-80-89186-13-6.

[2B] M. Chichina, <u>V. Stranak</u>, O. Churpita, S. Kment, Z. Hubicka, M. Tichy, P. Spatenka, *Deposition of thin* TiO_x *layers using plasma sources of jet types.* In: Proceedings of **SAPP XVI, 2007**, Podbanske, January 20–25, (2007), (ed. J. Matuska, S. Matejcik, J. D. Skalny), 139-140. ISBN 978-80-89186-13-6.

[3B] <u>V. Stranak</u>, M. Tichy, V. Kriha, V. Scholtz, Z. Navratil, P. Slavicek, P. Spatenka, *Bio-medical applications and diagnostics of microwave plasma.* In: Proceedings of **ESCAMPIG 2006** Vol. 30G, Lecce, July 12–16, (2006), (ed. M. Cacciatore, S. De. Benedictis, P. F. Ambrico, M. Rutigliano), 441–442. ISBN 2-914771-38-X.

[4B] <u>V. Stranak</u>, M. Tichy, V. Kriha, V. Scholtz, F. Houser, P. Spatenka, B. Sera, *Biotechnological applications of surfatron plasma discharge.* In: Proceedings of **WDS 06**, part II, Prague, June 6–9, (2006), (ed. J. Safrankova, J. Pavlu), 139–144, ISBN 80-86732-85-1.

[5B] J. Blazek, J. Olejnicek, <u>V. Stranak</u>, P. Spatenka, *Modification of Abel transformation to refractional methods.* In: Proceedings of 14th Annual Conference **Technical Computing Prague 2006**, Prague, October 26, (2006), CD-ROM, ISBN 80-7080-616-8, 7 pages.

[6B] <u>V. Stranak</u>, M. Tichy, J. Blazek, Z. Navratil, P. Slavicek, P. Adamek, P. Spatenka, *Surfatron plasma source working at frequency* 2.45 GHz *for technological applications.* In: Proceedings of **PLASMA–2005**, AIP Vol. 812, Opole-Turawa, September 6–9, (2005), (ed. M. J. Sadowski, M. Dudeck, H.–J. Hartfuss, E. Pawelec), 181–190, ISBN 0-7354-0304-X.

[7B] <u>V. Stranak</u>, M. Tichy, Z. Navratil, P. Slavicek, P. Adamek, J. Blazek, M. Prokysek, P. Spatenka, *Surfatron plasma source of jet type - construction and diagnostics.* In: Proceedings of **WDS 05**, part II, Prague, June 7–10, (2005), (ed. J. Safrankova), 319–325, ISBN 80-86732-59-2.

[8B] J. Blazek, <u>V. Stranak</u>, P. Spatenka, *Langmuir probe diagnostics of negative-ion plasma.* In: Proceedings of 13th Annual Conference **Technical Computing Prague 2005**, Prague, November 11, (2005), CD-ROM, ISBN 80-7080-577-3, 9 pages.

[9B] <u>V. Stranak</u>, J. Blazek, S. Wrehde, H. Steffen, M. Tichy, P. Spatenka, R. Hippler *Langmuir probe disagnostics of* Ar *planar magnetron discharge with reactive admixtures* N_2 *and* O_2. In: e-Proceeding of 17th Conference **ISPC**, Toronto, August 7–12, (2005), (ed. J. Mostaghimi, T. W. Coyle, V. A. Pershin, H. R. Salimi Jazi).

[10B] <u>V. Stranak</u>, J. Blazek, M. Tichy, P. Spatenka, H. Steffen, S. Wrehde, R. Hippler, *Determination of negative ion density in slightly electronegative plasma.* In: Proceedings of **ICPIG XXVII** Confererence, Eidhoven, July 17–22, (2005), (ed. E. M. van-Veldhuizen), ISBN 90-386-2231-7.

[11B] Z. Navratil, P. Slavicek, <u>V. Stranak</u>, M. Sery, M. Tichy, D. Trunec, P. Spatenka, P. Stahel, *Optical emission spectroscopy of surfatron generated plasma in* Ar/O_2 *and* N_2/O_2 *mixtures.* In: Proceedings of **ICPIG XXVII** Confererence, Eidhoven, July 17–22, (2005), (ed. E. M. van Veldhuizen), ISBN 90-386-2231-7.

[12B] <u>V. Stranak</u>, Z. Navratil, P. Slavicek, M. Sery, M. Tichy, P. Spatenka, D. Trunec, *Comparative diagnostics of* Ar *and* He *surfatron generated plasma by means of optical emission spectroscopy and probe measurements.* In: Proceedings of 12th Conference **ICPP**, Nice, October 25–29, (2004).

[13B] <u>V. Stranak</u>, Z. Navratil, P. Slavicek, M. Tichy, P. Spatenka, D. Trunec, *Optical emission spectroscopy of argon plasma generated by surfatron at frequency* 2.45 GHz. In: Proceedings of the 17th Conference **Escampig 2004**, Constanta, September 1 - 5, (2004), (ed. V. Ciupina, G. Musa, R. Vladoiu), 181–183.

[14B] <u>V. Stranak</u>, Z. Navratil, P. Slavicek, M. Sery, J. Blazek, P. Spatenka, M. Tichy, *Optical emission spectroscopy and probe measurement in* Ar/N_2 *surfatron discharge.* In: Proceedings of **WDS 04**, Part II, Prague, June 15–18, (2004), (ed. J. Safrankova), 339–343. ISBN 80-86732-32-0.

[15B] <u>V. Stranak</u>, S. Wrehde, H. Steffen, R. Hippler, M. Tichy, *Langmuir probe measurements in a dc-magnetron discharge.* In: Proceedings of **Fruhjahrstagung 4/2004**, Kiel, March 8–11, (2004), ISSN 0420-0195. (in German)

[16B] <u>V. Stranak</u>, M. Tichy, P. Adamek, J. Blazek, P. Spatenka, *Probe measurement of the characteristics of surfatron generated argon plasma.* In: Proceedings of **WDS 03**, Part II, Prague, June 10–13, (2003), (ed. J. Safrankova), 407-411, ISBN 80-86732-18-5.

[17B] P. Kriz, <u>V. Stranak</u>, J. Blazek, *Optical diagnostics of barrier-torch discharge burning at atmospheric pressure.* In: Proceedings of **WDS 03**, Part II, Prague, June 10–13, (2003), (ed. J. Safrankova), 403-407, ISBN 80-86732-18-5.

[18B] <u>V. Stranak</u>, M. Tichy, P. Adamek, J. Blazek, P. Kriz, P. Spatenka, *Electron temperature in surfatron–generated plasma–jet in argon measured by double Langmuir probe.* In: Proceedings of **ICPIG XXVI** Confererence, Vol. 3., Greifswald, July 15–20, (2003), (ed. J. Meichsner, D. Loffhagen and H.-E. Wagner), 249–250, ISBN 3-00-011689-3.

[19B] <u>V. Stranak</u>, M. Tichy, P. Adamek, J. Blazek, P. Kriz, *A surfatron plasma source for material processing and biomedical application.* In: Proceedings of **APP Spring Meeting**, Bad Honnef, February 23–26, (2003), 129–132.

[20B] P. Kriz, <u>V. Stranak</u>, J. Blazek, V. Stach, *Holographic interferometry of barrier torch discharge.*In: Proceedings of **WDS 02**, Part II, Prague, June 11–14, (2002), (ed. J. Safrankova), 418–422, ISBN 80-85863-88-X.

[21B] P. Kriz, J. Blazek, <u>V. Stranak</u>, M. Sicha, *Determination of mass density distribution in low - temperature discharges by means of holographic interferometry.* In: Proceedings of 16th **ESCAMPIG** and 5th **ICRP** Conferences, Vol. 2, Grenoble, July 14–18, (2002), (ed. J. Sadeghi, H. Sugai), 139–140.